


3-29-2016

# Closing a Synthetic Carbon Cycle: Carbon Dioxide Conversion to Carbon Monoxide for Liquid Fuels Synthesis

Yolanda Andreina Daza

Follow this and additional works at: <http://scholarcommons.usf.edu/etd>

 Part of the [Chemical Engineering Commons](#), and the [Materials Science and Engineering Commons](#)

## Scholar Commons Citation

Daza, Yolanda Andreina, "Closing a Synthetic Carbon Cycle: Carbon Dioxide Conversion to Carbon Monoxide for Liquid Fuels Synthesis" (2016). *Graduate Theses and Dissertations*.  
<http://scholarcommons.usf.edu/etd/6079>

This Dissertation is brought to you for free and open access by the Graduate School at Scholar Commons. It has been accepted for inclusion in Graduate Theses and Dissertations by an authorized administrator of Scholar Commons. For more information, please contact [scholarcommons@usf.edu](mailto:scholarcommons@usf.edu).

Closing a Synthetic Carbon Cycle:  
Carbon Dioxide Conversion to Carbon Monoxide for Liquid Fuels Synthesis

by

Yolanda A. Daza

A dissertation submitted in partial fulfillment  
of the requirements for the degree of  
Doctor of Philosophy  
Department of Chemical and Biomedical Engineering  
College of Engineering  
University of South Florida

Major Professor: John N. Kuhn, Ph.D.  
Venkat R. Bhethanabotla, Ph.D.  
Babu Joseph, Ph.D.  
Rudiger Schlaf, Ph.D.  
Matthew M. Yung, Ph.D.

Date of Approval:  
March 21, 2016

Keywords: Reverse Water Gas Shift, Chemical Looping, RWGS-CL, Perovskite Oxides,  
Isothermal CO<sub>2</sub> Conversion, Carbon Capture and Utilization, CCU

Copyright © 2016, Yolanda A. Daza

## DEDICATION

To God, my parents, my family and my friends, especially Mariela and Romina.

## ACKNOWLEDGMENTS

I would like to acknowledge my committee members for the guidance. I thank the previous and current members of the Heterogeneous Catalysis & Materials Chemistry Group: Adela Ramos, Bryan Hare, Debtanu Maiti, Ryan Kent, Dr. Sandy Pettit, Nada Elsayed, Ummuhan Cimenler, Dr. Selasi Blavo, Dr. Selma Hokenek, Devin Walker and Tim Roberge for all the help and support. Thank you to Wenyang Gao for all the help in the lab. I would also like to thank Mr. Bernard Batson for all his help and direction, and Mr. Rod Hale for providing me with much needed guidance and advice at the beginning of my Ph.D.

I would particularly like to thank Dr. Kuhn for his patience, guidance and advice throughout my stay at USF.

The research presented in this document was funded by the Graduate Students Success Scholarship that is administered by the USF School of Graduate Studies, the McKnight Dissertation Fellowship administered by the Florida Education Fund, the Dissertation Improvement Fellowship administered by NASA Florida Space Grant Consortium and NSF award 1335817.

## TABLE OF CONTENTS

LIST OF TABLES.....	v
LIST OF FIGURES .....	vi
ABSTRACT.....	viii
CHAPTER 1: INTRODUCTION.....	1
1.1 CO <sub>2</sub> Availability and Current Utilization .....	1
1.2 CO <sub>2</sub> as a Resource for Liquid Hydrocarbon Fuel Production.....	2
1.3 Green Technologies for CO <sub>2</sub> Conversion to Fuels with Large Demand .....	3
1.4 Rationale for RWGS Catalysis over Competing Technologies.....	4
1.5 Intensified RWGS.....	5
1.5.1 Reverse Water Gas Shift Chemical Looping.....	6
CHAPTER 2: MATERIALS AND METHODS .....	9
2.1 Perovskite Oxides .....	9
2.1.1 Effect of Different Metals on the Properties of the Perovskite Oxides .....	10
2.1.2 Redox Reactions on Perovskite Oxides .....	11
2.1.3 Synthesis of Perovskite Oxides by Sol-Gel Methods .....	13
2.1.3.1 Introduction to the Pechini Synthesis Method.....	13
2.1.3.2 Experimental Procedure for the Pechini Synthesis Method .....	14
2.2 Characterization Techniques.....	15
2.2.1 Gas Sorption.....	15
2.2.2 X-Ray Diffraction .....	15
2.2.3 Mass Spectrometry.....	16
CHAPTER 3: CARBON DIOXIDE CONVERSION BY REVERSE WATER GAS SHIFT CHEMICAL LOOPING ON PEROVSKITE-TYPE OXIDES.....	20
3.1 Introduction.....	20
3.2 Experimental Procedure.....	23
3.2.1 Synthesis of Oxide Powders La <sub>1-x</sub> Sr <sub>x</sub> CoO <sub>3-δ</sub> .....	23
3.2.2 XRD .....	24
3.2.3 BET Surface Area .....	24
3.2.4 Temperature-Programmed Reduction (TPR) .....	24
3.2.5 Temperature-Programmed Oxidation with CO <sub>2</sub> (TPO-CO <sub>2</sub> ) .....	25
3.2.6 Isothermal CO <sub>2</sub> Conversion .....	25
3.2.7 In-situ XRD .....	25

3.2.8 Recyclability Studies.....	26
3.3 Results.....	26
3.3.1 Synthesis, Surface Analysis, and Bulk Structure Characterization of the $(La_{1-x}Sr_x)CoO_{3-\delta}$ Powders.....	26
3.3.2 Effect of A-Site Composition on the Reducibility by $H_2$ and the Re-Oxidation by $CO_2$ .....	28
3.3.3 Assessment of $La_{0.75}Sr_{0.25}CoO_3$ for $CO_2$ Conversion to $CO$ .....	30
3.3.3.1 Phase Evolution Under Hydrogen as a Function of Temperature.....	31
3.3.3.2 Isothermal $CO_2$ Conversion.....	31
3.3.3.3 Recyclability.....	32
3.4 Discussion.....	34
3.4.1 Role of Metallic Cobalt in the Reduction of Carbon Dioxide to Carbon Monoxide.....	34
3.4.2 Comparison of RWGS-CL to Other Techniques.....	35
3.4.2.1 Thermochemical Cycles.....	35
3.4.2.2 RWGS.....	37
3.4.2.3 Photochemical.....	38
3.5 Summary.....	38
CHAPTER 4: ISOTHERMAL REVERSE WATER GAS SHIFT CHEMICAL LOOPING ON $La_{0.75}Sr_{0.25}Co_{(1-y)}Fe_yO_3$ PEROVSKITE TYPE OXIDES.....	47
4.1 Introduction.....	47
4.2 Experimental Procedure.....	51
4.2.1 Synthesis of Oxide Powders.....	51
4.2.2 Characterization.....	52
4.2.2.1 XRD.....	52
4.2.2.2 BET Surface Area.....	52
4.2.3 Reaction Experiments.....	52
4.2.3.1 Temperature-Programmed Reduction (TPR).....	53
4.2.3.2 Temperature-Programmed Oxidation with $CO_2$ (TPO- $CO_2$ ).....	53
4.2.3.3 Isothermal RWGS-CL.....	53
4.2.3.4 Carbon Deposit on $La_{0.75}Sr_{0.25}FeO_3$ .....	53
4.3 Results and Discussion.....	54
4.3.1 Surface Area, Bulk Structure, Reducibility, and Re- Oxidation Capabilities.....	54
4.3.2 Isothermal RWGS-CL Using $La_{0.75}Sr_{0.25}FeO_3$ .....	58
4.3.2.1 Reaction Rates and Changes in Oxygen Stoichiometry.....	58
4.3.2.2 Role of Oxygen Vacancies on $CO_2$ Adsorption.....	59
4.3.2.3 Crystalline Structure Stability.....	61
4.3.2.4 Selectivity Towards $CO$ .....	61
4.4 Summary.....	62

CHAPTER 5: MORE CU, MORE PROBLEMS: DECREASED CO <sub>2</sub> CONVERSION ABILITY BY CU-DOPED LA <sub>0.75</sub> SR <sub>0.25</sub> FeO <sub>3</sub> PEROVSKITE OXIDES.....	69
5.1 Introduction.....	69
5.2 Materials and Methods.....	72
5.2.1 Synthesis of Oxide Powders .....	72
5.2.2 XRD .....	73
5.2.3 Reaction Experiments .....	73
5.2.3.1 Temperature-Programmed Oxygen Vacancy Formation.....	73
5.2.3.2 Temperature-Programmed Reduction (TPR).....	73
5.2.3.3 Temperature-Programmed Oxidation with CO <sub>2</sub> (TPO-CO <sub>2</sub> ) .....	73
5.3 Results.....	74
5.3.1 Effect of Cu Addition in the Crystalline Structure, Oxygen Vacancies Formation and Reducibility of the Samples .....	74
5.3.2 Effect of Cu Doping in the CO Formation Profiles of La <sub>0.75</sub> Sr <sub>0.25</sub> Fe <sub>1-y</sub> Cu <sub>y</sub> O <sub>3</sub> Perovskites .....	79
5.4 Discussion.....	81
5.4.1 Effect of Cu Containing Secondary Phases .....	81
5.4.2 Effects of B-site Doping of Cu into the La <sub>0.75</sub> Sr <sub>0.25</sub> FeO <sub>3</sub> Perovskite .....	83
5.5 Conclusion.....	83
CHAPTER 6: ENERGY REQUIREMENTS OF THE PROCESS.....	90
6.1 Overview.....	90
6.2 Design Parameters .....	90
6.2.1 CO <sub>2</sub> Source.....	90
6.2.2 H <sub>2</sub> Source .....	91
6.2.3 RWGS-CL Reactor .....	92
6.2.4 CO Hydrogenation Products .....	92
6.3 Results .....	93
CHAPTER 7: CONCLUSIONS AND FUTURE WORK.....	97
7.1 Conclusions .....	97
7.2 Future Work.....	99
7.2.1 Role of Supports .....	99
7.2.2 Low Temperature Thermochemical Cycles.....	99
7.2.3 Earth-Abundant Metals.....	100
7.2.4 Process Energy Requirements and Potential Economic Outlook .....	100
REFERENCES .....	101
APPENDICES .....	114
Appendix A Copyright Permissions .....	115

A.1 Permission for Use of Material in Chapter 3 .....	115
A.2 Permission for Use of Material in Chapter 4 .....	116
A.3 Permission for Use of Material in Chapter 5 .....	117
Appendix B Calculations .....	118
B.1 X-Ray Diffraction Qualitative Analysis for Different Geometries .....	118
B.2 Sample Ionization Factor Calculations .....	119
B.3 Procedure for Mass Spectrometry Qualitative Analysis.....	121
B.4 Data Used in Calculations on Chapter 6 .....	122



## LIST OF TABLES

Table 3.1	CO generation rate during the first ten min of the reaction .....	44
Table 3.2	CO produced during the cycles of H <sub>2</sub> reduction and CO <sub>2</sub> re-oxidation of La <sub>0.75</sub> Sr <sub>0.25</sub> CoO <sub>3-δ</sub> .....	44
Table 3.3	Rates and evolution of CO produced on different materials at STP conditions.....	45
Table 4.1	Surface area and crystallographic parameters of La <sub>0.75</sub> Sr <sub>0.25</sub> Co <sub>(1-Y)</sub> Fe <sub>Y</sub> O <sub>3</sub> .....	68
Table 4.3	Lattice parameters changes of the La <sub>0.75</sub> Sr <sub>0.25</sub> FeO <sub>3</sub> sample throughout the RWGS-CL cycles.....	68
Table 5.1	Abbreviations.....	88
Table 5.2	Unit cell parameters of the perovskite phases for the fresh La <sub>0.75</sub> Sr <sub>0.25</sub> Fe <sub>1-Y</sub> Cu <sub>Y</sub> O <sub>3</sub> samples as calculated from X-ray diffraction data.....	88
Table 5.3	H <sub>2</sub> O and CO formation on the La <sub>0.75</sub> Sr <sub>0.25</sub> Fe <sub>1-Y</sub> Cu <sub>Y</sub> O <sub>3</sub> (Y=0, 0.10 and 0.25) samples during the temperature-programmed oxidation with CO <sub>2</sub> (CO formation) experiments.....	88
Table 5.4	Rate of CO formation at T = 550°C on the RWGS-CL process on La <sub>0.75</sub> Sr <sub>0.25</sub> FeO <sub>3</sub> and Cu-supported La <sub>0.75</sub> Sr <sub>0.25</sub> FeO <sub>3</sub> perovskite oxides.....	89
Table 6.1	Results from preliminary economic and energy assessment .....	95
Table B-1	Summary of equations .....	118
Table B-4	Constants used in the calculations .....	122

## LIST OF FIGURES

Figure 1.1	Pictorial representation of the intensified reverse water gas shift (RWGS-CL) process .....	8
Figure 2.1	Materials .....	18
Figure 2.2	Different steps in the powders synthesis.....	18
Figure 2.3	TPO profile of uncharred SrCoO <sub>3</sub> to determine the optimal charring temperature .....	19
Figure 2.4	Mass spectrometer reaction set up .....	19
Figure 2.5	U-tube reactor packed with perovskite immobilized between glass wool.....	19
Figure 3.1	Schematic representation of the overall proposed process .....	40
Figure 3.2	Schematic representation of CO <sub>2</sub> conversion to CO on the oxygen deficient oxide system.....	40
Figure 3.3	TPO profile of uncharred LaCoO <sub>3</sub> to determine the optimal charring temperature .....	41
Figure 3.4	X-ray diffraction patterns of fresh (La <sub>1-x</sub> Sr <sub>x</sub> )CoO <sub>3-δ</sub> powders .....	41
Figure 3.5	Temperature-programmed reduction with 5%H <sub>2</sub> /N <sub>2</sub> of (La <sub>1-x</sub> Sr <sub>x</sub> )CoO <sub>3-δ</sub> samples .....	42
Figure 3.6	Carbon monoxide generation with 10%CO <sub>2</sub> /He using H <sub>2</sub> -pretreated (La <sub>1-x</sub> Sr <sub>x</sub> )CoO <sub>3-δ</sub> .....	42
Figure 3.7	X-ray diffraction patterns of (La <sub>1-x</sub> Sr <sub>x</sub> )CoO <sub>3-δ</sub> samples after a 10% H <sub>2</sub> /He pretreatment at 600 °C and after isothermal CO <sub>2</sub> conversion with 10% CO <sub>2</sub> /He at 850 °C.....	43
Figure 3.8	Changes in La <sub>0.75</sub> Sr <sub>0.25</sub> CoO <sub>3-δ</sub> crystalline structure while it is heated in 10% H <sub>2</sub> /He .....	43

Figure 3.9	Changes in $\text{La}_{0.75}\text{Sr}_{0.25}\text{CoO}_{3-\delta}$ crystalline structure throughout the cycles.....	44
Figure 4.1	X-ray diffraction patterns of the $\text{La}_{0.75}\text{Sr}_{0.25}\text{Co}_{(1-Y)}\text{Fe}_{(Y)}\text{O}_3$ powders.....	64
Figure 4.2	Temperature-programmed reduction of $\text{La}_{0.75}\text{Sr}_{0.25}\text{Co}_{(1-Y)}\text{Fe}_{(Y)}\text{O}_3$ by 10% $\text{H}_2/\text{He}$ .....	64
Figure 4.3	Temperature-programmed oxidation of $\text{La}_{0.75}\text{Sr}_{0.25}\text{Co}_{(1-Y)}\text{Fe}_{(Y)}\text{O}_3$ under 6.7% $\text{CO}_2/\text{He}$ after an isothermal reduction at 550 °C for 30 min by 10% $\text{H}_2/\text{He}$ .....	65
Figure 4.4	Five cycles of RWGS-CL on 76.1mg of $\text{La}_{0.75}\text{Sr}_{0.25}\text{FeO}_3$ at 550 °C .....	65
Figure 4.5	RWGS-CL on $\text{La}_{0.75}\text{Sr}_{0.25}\text{FeO}_3$ at 550 °C .....	66
Figure 4.6	Oxygen stoichiometry variations on the $\text{La}_{0.75}\text{Sr}_{0.25}\text{FeO}_3$ during the RWGS-CL at 550 °C .....	67
Figure 4.7	X-ray diffraction patterns of the $\text{La}_{0.75}\text{Sr}_{0.25}\text{FeO}_3$ powder throughout the RWGS-CL cycles.....	67
Figure 5.1	X-ray results.....	85
Figure 5.2	TP-Ovac formation results.....	86
Figure 5.3	TPR results.....	86
Figure 5.4	XRD patterns after isothermal reduction at 450 °C in 10% $\text{H}_2/\text{He}$ for 30 min .....	87
Figure 5.5	Temperature-programmed CO formation on Cu0, Cu10 and Cu25 (raw signals of $m/z=28$ ) after isothermal reduction at 450 °C in 10% $\text{H}_2/\text{He}$ for 30 min .....	87
Figure 6.1	Schematic representation of the reactor configuration on the applied RWGS-CL process .....	95
Figure 6.2	Mass balance scheme of the RWGS-CL combined processes.....	96

## ABSTRACT

CO<sub>2</sub> global emissions exceed 30 Giga tonnes (Gt) per year, and the high atmospheric concentrations are detrimental to the environment. In spite of efforts to decrease emissions by sequestration (carbon capture and storage) and repurposing (use in fine chemicals synthesis and oil extraction), more than 98% of CO<sub>2</sub> generated is released to the atmosphere. With emissions expected to increase, transforming CO<sub>2</sub> to chemicals of high demand could be an alternative to decrease its atmospheric concentration. Transportation fuels represent 26% of the global energy consumption, making it an ideal end product that could match the scale of CO<sub>2</sub> generation. The long-term goal of the study is to transform CO<sub>2</sub> to liquid fuels closing a synthetic carbon cycle.

Synthetic fuels, such as diesel and gasoline, can be produced from syngas (a combination of CO and H<sub>2</sub>) by Fischer Tropsch synthesis or methanol synthesis, respectively. Methanol can be turned into gasoline by MTO technologies. Technologies to make renewable hydrogen are already in existence, but CO is almost exclusively generated from methane. Due to the high stability of the CO<sub>2</sub> molecule, its transformation is very energy intensive. Therefore, the current challenge is developing technologies for the conversion of CO<sub>2</sub> to CO with a low energy requirement.

The work in this dissertation describes the development of a recyclable, isothermal, low-temperature process for the conversion of CO<sub>2</sub> to CO with high selectivity, called Reverse Water Gas Shift Chemical Looping (RWGS-CL). In this process, H<sub>2</sub> is used to generate oxygen vacancies in a metal oxide bed. These vacancies then can be re-filled by one O atom from CO<sub>2</sub>, producing CO. Perovskites (ABO<sub>3</sub>) were used as the oxide material due to their high oxygen

mobility and stability. They were synthesized by the Pechini sol-gel synthesis, and characterized with X-ray diffraction and surface area measurements. Mass spectrometry was used to evaluate the reducibility and re-oxidation abilities of the materials with temperature-programmed reduction and oxidation experiments. Cycles of RWGS-CL were performed in a packed bed reactor to study CO production rates.

Different metal compositions on the A and B site of the oxide were tested. In all the studies, La and Sr were used on the A site because their combination is known to enhance oxygen vacancies formation and CO<sub>2</sub> adsorption on the perovskites. The RWGS-CL was first demonstrated in a non-isothermal process at 500 °C for the H<sub>2</sub>-reduction and 850 °C for the CO<sub>2</sub> conversion on a Co-based perovskite. This perovskite was too unstable for the H<sub>2</sub> treatment. Addition of Fe to the perovskite enhanced its stability, and allowed for an isothermal and recyclable process at 550 °C with high selectivity towards CO. In an effort to decrease the operating temperature, Cu was incorporated to the structure. It was found that Cu addition inhibited CO formation and formed very unstable oxide materials.

Preliminary studies show that application of this technology has the potential to significantly reduce CO<sub>2</sub> emissions from captured flue gases (i.e. from power plants) or from concentrated CO<sub>2</sub> (adsorbed from the atmosphere), while generating a high value chemical. This technology also has possible applications in space explorations, especially in environments like Mars atmosphere, which has high concentrations of atmospheric carbon dioxide.

## CHAPTER 1: INTRODUCTION<sup>1</sup>

### 1.1 CO<sub>2</sub> Availability and Current Utilization

Global carbon dioxide atmospheric concentration recently reached the 400 ppm threshold, putting the world at 1.5 °C above the average temperature prior to the industrial revolution. In 2012, 31.7 giga tonnes (Gt) of CO<sub>2</sub> were emitted to the atmosphere [1], and emissions are expected to increase to 45 Gt/year by 2040, if this happens, it is foreseen that global temperature will increase 2 °C above pre-industrial times at which point the environmental changes would be almost irreversible.

The rapidly increasing atmospheric CO<sub>2</sub> concentration and the threat it poses upon the environment has led to increased efforts to reduce emissions. Amongst the most widely used approaches is Carbon Capture and Storage (CCS), more commonly called sequestration. According to the Global CCS Institute, sequestration is at a current estimated large projects capacity of 80 Mt CO<sub>2</sub>/year [2]. Furthermore, current CO<sub>2</sub> utilizations for industrial processes such as ammonia synthesis, use in carbonated beverages, etc. does not exceed 130 Mt/year [3].

Production of CO<sub>2</sub> is more than 150 times higher than its current and potential use or sequestration capability. Due to its large scale, a combination of methods and technologies at all levels of society, from industry to individual households, should be used if we are to significantly reduce CO<sub>2</sub> emissions [2, 3].

Recently, a variety of technologies for repurposing the vastly available carbon dioxide into high value chemicals have emerged. To fulfill the ultimate resolution of environmental

---

<sup>1</sup> This chapter will be submitted as part of a manuscript invited to RSC Advances

remediation, these technologies should be renewable, and the overall process needs to be carbon negative. If we consider the costs of CO<sub>2</sub> transportation and storage (~\$ 16.5/tonne CO<sub>2</sub> [4]), developing technologies for Carbon Capture and Utilization (CCU) seem to make more sense than simply sequestering CO<sub>2</sub>. But the stability of the molecule is another challenge to overcome. CO<sub>2</sub> is the most stable form of carbon, making its transformation very energy intensive.

Technologies currently under research to transform CO<sub>2</sub> to chemicals of wide use include synthesis of polymers [3], oxalates [5], formates [6], dimethyl ether [7], ethylene and propylene [8] and an interesting recently developed technology by Job et al. [9], that can recycle CO<sub>2</sub> onto plastics similar to polyurethane (up to 50% CO<sub>2</sub> by weight). But even at the high global demand for plastics (311 Mt), if all the plastic produced in the world was synthesized with this technology, we estimate that CO<sub>2</sub> emissions wouldn't decrease more than 0.05%. Similarly, if all the methanol [10] and chemicals (made from oil) [11] consumed globally were synthesized from CO<sub>2</sub>, emissions would not decrease by more than 0.26% and 4% respectively. Still, the key factors of utilization remain an issue: (i) the need for concentrated CO<sub>2</sub> [12, 13] and (ii) proven technologies for conversion that can match the scale of CO<sub>2</sub> production, and produce chemicals of significantly high demand [12-15].

## **1.2 CO<sub>2</sub> as a Resource for Liquid Hydrocarbon Fuel Production**

In a worldwide effort to increase environmental friendliness, the use of alternative renewable technologies (solar, wind, geothermal, nuclear, hydro...) have been steadily increasing, and have evolved from representing 2.8% of the world energy production in 1973 to 8.3% in 2012 [1]. The limitation is that these renewable energy sources are mostly used to make electricity, and in 2012, electricity only represented 18.1% of the global energy consumption. From this percentage, 67.9% of electricity was produced by fossil fuels [1]. This is likely the

biggest window for growth that renewable energy has on the world energy consumption. The challenge for alternate renewable energy sources is that energy can't be efficiently stored. Solar, wind, tide... do not constantly produce energy and go through peaks where the energy produced is likely wasted.

The last statement describes clearly why fossil fuels are still necessary. Oil represents 40.7% of world energy consumption, and 63.7% of total oil products were used to make transportation fuels [1]. The demand for fuels is at least 100 times larger than chemicals [16]. Furthermore, only liquid fuel demand matches the scale of CO<sub>2</sub> production [13, 17, 18].

So far, no other type of fuel has been able to outrank the practicality of liquid fuels, therefore energy dense fuels are still necessary [19, 20], and unless renewables are used to make energy dense fuels, the world will continue to depend on liquid fossil fuels.

As an alternative, synthetic liquid hydrocarbon fuels with high energy density have been synthesized and studied [21]. So this excess energy could be stored in the form of liquid fuels to be used when needed. But converting CO<sub>2</sub> to fuels poses another crucial problem, the need for renewable hydrogen [22-27], which is still a technology in development [28].

### **1.3 Green Technologies for CO<sub>2</sub> Conversion to Fuels with Large Demand**

The technologies that are focused on converting CO<sub>2</sub> to fuels are limited to (1) syngas synthesis from methane dry reforming (DR), (2) direct hydrogenation of CO<sub>2</sub> to methanol and (3) RWGS reaction. Electrochemical reduction of CO<sub>2</sub> is currently not a viable way to reduce emissions because the scale of conversion would be much lower than RWGS [29].

Methane is a relatively abundant chemical, in 2013 its global production was 3479 billion m<sup>3</sup> [1], which is equivalent, in moles, to ~20% of CO<sub>2</sub> yearly emissions. Due to its scale of production, methane is the chemical with the highest potential for CO<sub>2</sub> conversion. DR is an



endothermic reaction [10], favored at high temperatures, at which catalysts sinter and coke [19] and deactivate due to high sulfur levels [10]. Low temperature DR has been reported (430–470 °C) with no coking, but using an assembly of noble and transition metal catalysts combined with metal oxides (Pt–Ni–Mg/ceria–zirconia catalysts [30]) which have yet not been studied for poisoning.

Direct CO<sub>2</sub> hydrogenation is more thermodynamically favored than RWGS. Therefore, it was considered promising for industrialized methanol synthesis [31] and has been demonstrated industrially in Iceland by George Olah and Surya Prakash. However, the CAMERE process revealed 20% higher methanol yields when CO<sub>2</sub> is converted to CO (through RWGS), and CO to methanol, rather than directly hydrogenating CO<sub>2</sub> [23].

The RWGS is an endothermic reaction, favored at high temperatures [26]. The most commonly studied catalyst are copper based [32-35], or supported ceria [36-38], potentially less expensive than those used in DR. Its biggest advantage is the formation of CO, which can be used as a building block for a variety of important chemicals, such as hydrocarbons in Fischer-Tropsch synthesis, fine chemicals synthesis or the purification of nickel.

RWGS is also suspected to be a key step in selective methanation of CO<sub>2</sub> [39] and it is also suspected to occur in FT reactors with high CO<sub>2</sub> feeds [18, 40]. It becomes evident that RWGS is a key step that should be considered and fully understood.

#### **1.4 Rationale for RWGS Catalysis Over Competing Technologies**

The reverse water gas shift reaction was first patented by Carl Bosch and Wilhelm Wild in 1914 H<sub>2</sub> [41]. It was used as a way of avoiding the separation of CO from H<sub>2</sub> + CO mixtures, while having the added advantage of making extra H<sub>2</sub> [41]. Currently, it is important in the

synthesis of methanol [13], ammonia, and in fixing syngas' H<sub>2</sub>/CO ratio for Fischer-Tropsch feeds.

Taking CO<sub>2</sub> as the starting point, Mallapragada et al. [42] studied different routes to transform CO<sub>2</sub> into liquid fuels using solar assisted processes. The method is called “Sun-to-Fuels”. The importance of using Solar-aided processes is due to the need for green renewable energy, with an overall carbon negative process. Mallapragada et al. [42] determined that solar-assisted conversion of CO<sub>2</sub> to CO by reverse water gas shift reaction followed by CO conversion to fuels with FTS has the highest current and estimated potential efficiency. Furthermore, converting CO<sub>2</sub> to CO gives an added versatility in the products that can be obtained from CO transformation [11]. RWGS is also of great interest to be used in Mars due to its high (~95%) CO<sub>2</sub> atmospheric concentration [43, 44]. Therefore, RWGS is a promising reaction, whose products have a wide variety of potential end uses.

### **1.5 Intensified RWGS**

The first attempts to achieve an intensified RWGS process emerged from combining chemical looping with DR, but substituting CH<sub>4</sub> by H<sub>2</sub> due to its higher potential as a reducing agent. In a chemical looping process, the ability of the oxygen carrier to reduce and oxidize under the desired environments in a key factor that can determine the feasibility of the process. In the combined RWGS process with chemical looping, a metal oxide is used as an oxygen carrier. First, H<sub>2</sub> is used to reduce the metal oxide, followed by CO<sub>2</sub> flow which serves as an oxidant, returning the metal oxide to an oxidized state while CO is formed. The main advantages of an intensified RWGS – chemical looping process (RWGS-CL) are eliminating the possibility of methanation because the H<sub>2</sub> and CO<sub>2</sub> flow are always kept separate, and inherent product separation [45-47].

Thermodynamic modeling and experimental screening of transition metal oxides showed that Fe-based materials had one of the best CO<sub>2</sub> carrying capacities while having the ability to function in the widest variety of temperatures [48, 49]. Najera et al. [48] observed signs of stability on a 40% w/w Fe-BHA (Barium Hexaaluminate) porous sample on the intensified RWGS process over 6 reaction cycles. Adding ceria to iron oxide (CeO<sub>2</sub>-Fe<sub>2</sub>O<sub>3</sub>) linearly enhanced the stability of the solid solution, but decreased the CO formation capabilities [50].

### 1.5.1 Reverse Water Gas Shift Chemical Looping

A formal RWGS-CL process was demonstrated on La<sub>(1-x)</sub>Sr<sub>x</sub>CoO<sub>3</sub> perovskite oxides by Daza et al. [45], but amongst the studied temperatures, the H<sub>2</sub> reduction and CO<sub>2</sub> conversion happened with at least 50 °C difference, so the process was not isothermal.

Reduced Fe-based spinels had been used previously for CO<sub>2</sub> decomposition to C<sub>(s)</sub> and O<sub>2(g)</sub> at 300 °C [51, 52]. Based on these results, the RWGS-CL process was intensified on a La<sub>0.75</sub>Sr<sub>0.25</sub>FeO<sub>3</sub>, and was demonstrated under isothermal conditions at 550 °C [46]. By substituting cobalt with iron, the reducibility of the material was significantly decreased and it did not decomposed under H<sub>2</sub> flow.

However, the process was not fully stoichiometric, because even though oxygen vacancies were being created, not all of the vacancies were re-filled. DFT suggested that the driving force for the CO<sub>2</sub> bond cleavage was the increased CO<sub>2</sub> adsorption strength amongst the vacancies extent tested. RWGS was tested on La<sub>0.75</sub>Sr<sub>0.25</sub>Fe<sub>(1-y)</sub>Cu<sub>y</sub>O<sub>3</sub>, but doping Cu into the B site of the perovskite highly increased its reducibility and inhibited CO formation [47].

CO formation was achieved on both cobalt- and iron-based perovskites at similar reaction conditions, but the different solid state reactions the oxides underwent suggest very different reaction pathways. The high reducibility of the Co-based perovskite [45] lead to its reduction to

base  $\text{La}_2\text{O}_3$  and metallic Co. It is likely that  $\text{CO}_2$  then adsorbed in the basic lanthanum oxide or lanthanum-based Ruddlesden Popper phase and dissociated in the metallic cobalt, turning the metal into cobalt oxide (CoO) while yielding CO. On the iron based material, a surface redox mechanism between oxygen vacancies in the perovskite took place, where the  $\text{CO}_2$  was adsorbed likely on a lanthanum and Oxygen surface termination [53] close to an oxygen vacancy, then  $\text{CO}_2$  can dissociate into CO and a O adatom that re-fills the said oxygen vacancy [46]. Introducing Cu into the Fe-based perovskite increases the stability of the perovskite in its reduced state (after forming oxygen vacancies), therefore reducing its oxygen affinity and re-oxidation capabilities, therefore the observed outcome was a suppression of CO production because  $\text{CO}_2$  was not able to re-oxidized the reduced oxide [47].

Throughout the different studies with an intensified version of the conventional RWGS reaction, it is noteworthy that the best results were achieved with Fe-containing solid solutions. Even though it has been shown before that Fe-oxides can decompose  $\text{CO}_2$  to C(s) and  $\text{O}_2$  [51, 52], Fe-based oxides show the highest CO formation. Only one study has tested selectivity towards CO (vs. C(s)) and the process is 30 times more selective towards CO [46]. It is also curious that even though Cu is widely used to catalyzed forward and reverse water gas shift, Fe is best for the intensified process.

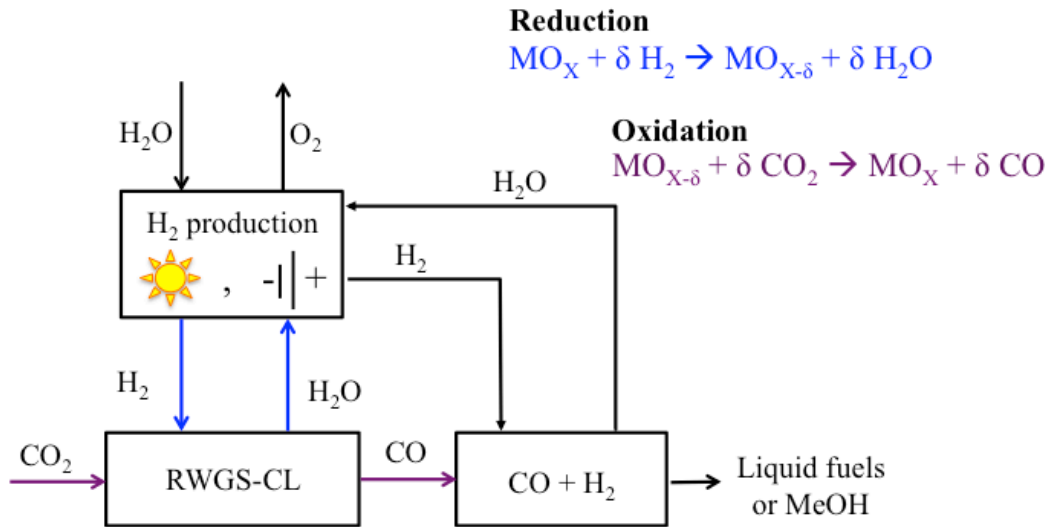


Figure 1.1 Pictorial representation of the intensified reverse water gas shift (RWGS-CL) process. Modified from [45].

## CHAPTER 2: MATERIALS AND METHODS

### 2.1 Perovskite Oxides

Perovskite oxides are mixed metal oxides of the general formula  $ABO_3$ . Where the A site metal is larger than the one occupying the B site [54-56]. Each site can be partially substituted to obtain a particular set of desired properties (magnetic, electrical, optical...) in each material [56-58]. Due to this ability to be tailored, a wide variety of uses can be given to these materials. They can be used as cathodes [59] and anodes [60] for solid oxide fuel cells and they have been studied in combustion reactions [61-64] due to their high oxygen exchange abilities. And they have been studied for  $NO_x$  reduction [57, 65-67] for applications mostly in catalytic converters.

The Ruddlesden Popper phase,  $A_{n-1}A'_2B_nX_{3n+1}$  where A and A' can be different lanthanides or rare earth metals, B is a smaller transition metal, X is an anion and n is the number of octahedral layers in the perovskite-like stack [68] are also of interest due to their higher oxygen surface exchange rates, when compared to typical  $ABO_3$ . They were first demonstrated by Ruddlesden and Popper in 1957 for n=1 materials [69]. For the n=1 ( $A_2BO_4$ ), the oxides exhibit a  $K_2NiF_4$  type structure [69] composed from a perovskite stacked with a rock salt (AO) and present a tetragonal crystalline structure [70]. Similarly to  $ABO_3$ , they can also be customized by partial substitution of the A and B site metals [71]. The difference in both phases can be observed in Figure 2.1.

When perovskites are heated in an inert or reducing environment, oxygen vacancies are formed in their structure [65, 72, 73]. The amount of oxygen vacancies formed depends on four

conditions: temperature, environment (low oxygen partial pressure or reducing agent used), size and valence of the cations on the A and B site [56, 74] and, under certain conditions, time spent under the reducing conditions [47, 75].

In an oxygen deficient environment, oxygen can be released from the structure upon heating, in an endothermic process [76]. Under a reducing environment (such as H<sub>2</sub>), the reduction profiles are dependent on the A and B site metals, and for a given B site metal, the extent of reduction has been found to increase with decreasing the ionic radius of the A site metal [77]. Typically, perovskites exhibit two reduction regions (as will be explained in temperature-programmed reduction experiments in later chapters). The first (low-temperature) region typically demonstrate the change in oxidation state of the B site metal, and the formation of oxygen vacancies [78], whereas the second (high temperature) region correlates to a phase change in the perovskite [63, 78], which can sometimes be reversible, upon O<sub>2</sub> flow.

### **2.1.1 Effect of Different Metals on the Properties of the Perovskite Oxides**

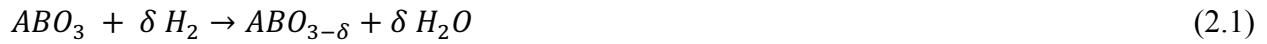
The use of Ln (lanthanides) and Me (transition metals) is of great interest because of the wide variety of properties that can be achieved in the perovskite. They can have magnetic, electrical and catalytic properties depending on the substitution of A and B site of the material [79]. Cu- based materials are well known to be superconductors [80, 81], Fe- based are magnetic [82] while Co-based exhibit different magnetic and conductive properties with high dependence on the temperature [83]

La-based perovskites have strong basic sites which enhances CO<sub>2</sub> adsorption [84]. The combination of La-Sr in the A site and Co in the B site has been studied for its anionic vacancy formation capabilities [85, 86]. Also, this combination its believed to enhance the oxygen vacancies formation because of the partial substitution of Sr<sup>2+</sup> in the A site, which creates a

charge unbalance that is stabilized by a coexistence of  $\text{Co}^{3+}$  and  $\text{Co}^{4+}$  [58, 74, 85, 87] in the oxide powders. Adding Fe to the Co-based perovskite enhances the stability of the crystalline structure [56, 88, 89]. Doping low amounts of Cu into the B site of La-based perovskites increases reducibility [90], which has been found favorable in redox reactions [91]. But high incorporation of Cu induces phase changes and appearance of several distinct phases and only Cu on the B site is unstable [90].

### 2.1.2 Redox Reactions on Perovskite Oxides

In general, the formation of oxygen vacancies on the oxides with a reducing agent, in this case hydrogen, can be represented by the reaction below:



whereas the re-oxidation of the reduced material with  $\text{CO}_2$  can be expressed by:



where the enthalpy of the oxygen vacancy formation (I) and re-oxidation with  $\text{CO}_2$  (II) reactions is given by:

$$\Delta H_{reduction}^{\circ} = \Delta H_{ABO_{3-\delta}}^{\circ} + \delta \Delta H_{H_2O}^{\circ} - \Delta H_{ABO_3}^{\circ} - \delta \Delta H_{H_2}^{\circ} \quad (2.3)$$

$$\Delta H_{oxidation}^{\circ} = \Delta H_{ABO_3}^{\circ} + \delta \Delta H_{CO}^{\circ} - \Delta H_{ABO_{3-\delta}}^{\circ} + \delta \Delta H_{CO_2}^{\circ} \quad (2.4)$$

respectively.

The formation energies of the oxygen vacant materials will depend on the metals' composition on the A and B site of the perovskite, the extent of oxygen vacancies ( $\delta$ ) formed during the  $\text{H}_2$ -reduction and the amount of oxygen vacancies that can be re-oxidized with  $\text{CO}_2$  [92, 93]. To perform accurate calculations, the aforementioned material properties should be considered. For the RWGS-CL, because reactions (2.1) and (2.2) can take place at the same



temperature for the  $La_{0.75}Sr_{0.25}FeO_3$ , we will neglect the temperature effects for this material. Also,  $\delta = 0.125$  will be assumed for the calculations in both reactions.

Then, using the  $\Delta H_{formation}^{o}La_{0.75}Sr_{0.25}FeO_3 = -146.44 \text{ KJ/mol}$  [94] and  $\Delta H_{formation}^{o}La_{0.75}Sr_{0.25}FeO_{3-0.125} = -426.77 \text{ KJ/mol}$  [94], we can calculate equations (2.3) and (2.4), respectively:

$$\begin{aligned}\Delta H_{reduction}^{o} &= \Delta H_{La_{0.75}Sr_{0.25}FeO_{3-0.125}}^{o} + 0.125 \Delta H_{H_2O}^{o} - \Delta H_{La_{0.75}Sr_{0.25}FeO_3}^{o} - 0.125 \Delta H_{H_2}^{o} \\ &= -310.56 \text{ KJ/mol}\end{aligned}$$

$$\begin{aligned}\Delta H_{oxidation}^{o} &= \Delta H_{La_{0.75}Sr_{0.25}FeO_3}^{o} + 0.125 \Delta H_{CO}^{o} - \Delta H_{La_{0.75}Sr_{0.25}FeO_{3-0.125}}^{o} + 0.125 \Delta H_{CO_2}^{o} \\ &= 315.70 \text{ KJ/mol}\end{aligned}$$

then, the formation of oxygen vacancies (2.3) is exothermic, while the re-oxidation of the material (2.4) is endothermic.

Simplistic scenarios such as adding the two reactions together (canceling the enthalpies of the oxides), leads to the conventional reverse water gas shift reaction, with a  $\Delta H_{reaction}^{o} = 41.18 \text{ KJ/mol}$ .

Other simplifications, such as neglecting the solid state enthalpies (i.e.  $\Delta H_{ABO_3} \approx \Delta H_{ABO_{3-\delta}}$ , would lead to:

$$\Delta H_{reduction}^{o} = \delta \Delta H_{H_2O}^{o} = -30.23 \text{ KJ/mol}$$

$$\Delta H_{oxidation}^{o} = -\delta \Delta H_{CO}^{o} + \delta \Delta H_{CO_2}^{o} = -13.81 \text{ KJ/mol} + 49.19 \text{ KJ/mol} = 35.38 \text{ KJ/mol}$$

Then,  $\Delta H_{reduction}^{o}$  (2.3) would still be exothermic, and  $\Delta H_{oxidation}^{o}$  (2.4) still endothermic, but the energies are at least one order of magnitude off. This confirms that for accurate calculations, the solid state enthalpies can't be neglected.

### 2.1.3 Synthesis of Perovskite Oxides by Sol-Gel Methods

Different methods have been developed for the synthesis of these types of materials. The most common are amorphous citrate [95], freeze drying [96] and sol-gel-based synthesis [97], but alternative methods like electrochemical synthesis [98], using activated cellulose [99] and combustion synthesis [100] have also been developed.

In Gelation or sol-gel synthesis, a solution with the dissolved metal precursors is turned into a hydrated solid (hydro-gel), which can be easily combusted to finally form the desired product. This process possesses the advantage of allowing a high control of texture, composition, homogeneity and structural properties of the end products. The homogeneity of the gel is highly dependent on the solubility of the metal precursors, therefore some studies have stabilized the pH of the samples to have an increased solubility of the metal precursors [101].

A point that usually remains common between all the synthesis methods is that previous to the synthesis, the desired molar ratios of the cations in the perovskite need to be determined and added accordingly.

**2.1.3.1 Introduction to the Pechini Synthesis Method.** The Pechini method, also called the polymeric precursor method [79], is the most commonly used form of solid-state synthesis [78]. It uses a carboxylic acid (citric acid) as a chelating agent in an aqueous medium to dissolve the salt precursors thus granting homogeneity to the dispersion of the cations in the solution [78, 79]. The dispersed cations are immobilized in a polymeric resin that is formed by the reaction between the acid and added ethylene glycol [78, 79]. The easiness of decomposition of the formed resin reduces the possibility of carbon contamination on the final product [101].

The Pechini method has the advantage of allowing a precise stoichiometry control of the product, homogeneity in the metal dispersion and high reproducibility over other methods used

for synthesizing perovskites [79]. Furthermore, this method usually yields single phase materials, which are desired because secondary phases can decrease the required properties [79].

**2.1.3.2 Experimental Procedure for the Pechini Synthesis Method.** In this work, the Pechini method as described by Popa and Kakihana [97], with a modification of the cations ratio as described by Ivanova et al. [78] was chosen to synthesize the perovskite powders (Figure 2.2).

First, the carbonates and/or nitrate precursors are carefully weighted and the molar ratios of metal precursors to citric acid are carefully controlled. Then, the precursors are added to an aqueous solution of citric acid, which is kept under magnetic stirring at 60°C for 2 h to enhance the solubility of the precursors (Figure 2.2 a). Typically, for a  $ABO_3$  perovskite, the molar ratios are 1:1:10 [78] for A site: B site: Citric acid, however, the ratio of metals to citric acid may vary depending on the solubility of the metal precursors in the citric acid aqueous solution.

Next ethylene glycol is added to react with citric acid forming a polymer (Figure 2.2 b) which immobilizes the cations in the solution [78]. The ratio of citric acid to ethylene glycol is often kept at 1:4 [78, 97]. The temperature of the solution is then increased to 90°C to evaporate the water and to make the polymer more viscous. After 7 h of heating, a highly viscous resin is obtained (Figure 2.2 b). The resin is then decanted to a crucible (Figure 2.2 c) for the heating treatments. The first heating is performed for 2 h at 450°C to remove most of the organic polymer, resulting in an amorphous powder (Figure 2.2 d). At this point, a small amount of the powder was separated from the main batch to perform a temperature-programmed oxidation with 20%  $O_2$  (He balance) to determine the crystallization temperature of the specific material (Figure 2.3). In this experiment, at a temperature usually above 700 °C, oxygen is consumed and carbon dioxide is formed due to a combustion reaction, which correlates to the formation of the crystalline powder. The existence of a range (instead of a set temperature) for the second heating,

is due to the dependence of the metal ions on the crystallization temperature, that is, the temperature at which the powders form a crystalline structure [97]. Evolution of the crystalline during the last step of the synthesis has been observed [88], therefore homogeneity of the conditions needs to be kept to ensure repeatability of the synthesis.

This powder is cooled and crushed before proceeding to the second heating, where charring (between 600°C and 900°C) in air is performed to form the crystalline powder (Figure 2.2 e). The obtained solid color is highly dependent on the metals added.

## **2.2 Characterization Techniques**

Characterization methods used to study the perovskite oxides will be briefly discussed; in-depth information can be found on each of the subsequent chapters,

### **2.2.1 Gas Sorption**

Surface area measurements were performed in a Quantachrome Autosorb IQ with N<sub>2</sub> as the adsorbant at 77 K. Prior to the measurements, the samples were outgassed usually at T > 100 °C to ensure water is removed from the porous and surface. Only partial pressures between 0.05 and 0.3 were considered for the calculations. The BET (Brunauer-Emmett-Teller) method [102] was used to calculate the surface area of the powders. This method considers both multilayer and monolayer adsorption.

### **2.2.2 X-Ray Diffraction**

X-ray diffraction (XRD) was used as the main method for determination of the crystalline structures. Three different devices were used to obtain the patterns showed in this dissertation. In chapter 3, a Phillips X-Ray and a Bruker D8 Diffractometers were used to collect the patterns at isothermal and temperature-programmed conditions respectively. Both devices had a CuK $\alpha$  ( $\lambda =$

0.154 nm) but different step sizes were used in each set up. In chapters 4 and 5, a Bruker X-Ray Diffractometer was used, also with a Cu K $\alpha$  ( $\lambda = 0.154$  nm) source and a step size of 0.0102 2 $\theta^\circ$ .

Almost the entirety of the X-ray diffraction patterns in this dissertation have been identified and their lattice parameters have been calculated using an iterative method with Bragg's Law.

$$n\lambda = 2d\sin\theta \quad (2.5)$$

where  $n$  is a positive integer (assumed 1),  $\lambda$  is the wavelength of the radiation source,  $d$  is the lattice distance and  $\theta$  is the incidence angle. And the lattice geometry equations for each symmetry system, obtained from reference [103] and are further explained in Appendix B-1, i.e. the cubic system relation:

$$d = \frac{a}{\sqrt{h^2+k^2+l^2}} \quad (2.6)$$

where  $a$  is the cubic lattice parameter and  $hkl$  the Miller indices of the Bragg plane. Bragg's law is used to obtain the experimental  $d$  values of the diffraction lines in the obtained pattern. Then,  $hkl$  values are assumed and introduced into the crystallographic relation, until a calculated  $d$  value matches the experimental  $d$  value with a minimum error.

### 2.2.3 Mass Spectrometry

In mass spectrometry (MS) technique, electrons bombard different gases, breaking the molecules into fragments. These fragments can be analyzed to determine the molecular weight of the original gas molecule, and different functional groups can be identified [104].

Figure 2.4 shows the experimental set up for all MS studies. Different gases are connected to the reactor inlet and their flow rates (in standard cubic centimeters) regulated by mass flow controllers. The simulation of the packed bed reactors is done by immobilizing ~75mg of powders between glass wool (Figure 2.5). This glass wool is unreactive and non-porous.

All quantifications of MS patterns were performed by a procedure found on Appendix B-3. In summary, CO<sub>2</sub>, CO, H<sub>2</sub>, H<sub>2</sub>O and O<sub>2</sub> were quantified using m/z=44, 28, 2, 18 and 32 respectively. In the first step, all baselines are removed, next, the contribution of CO<sub>2</sub> was subtracted from the m/z=28 signal (usually ~11% of m/z=44). Ideal gas law was used for calculating the molar flow rates, and the trapezoidal rule was used for calculating the areas under the curves for the different species.

Cubic perovskite ( $ABO_3$ )    Layered perovskite ( $A_2BO_4$ )

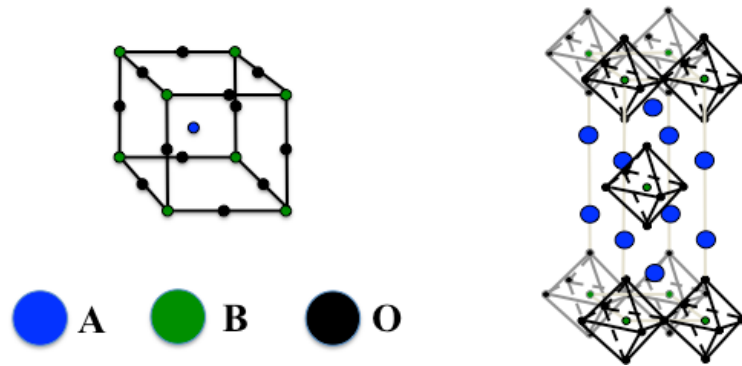


Figure 2.1 Materials. (left)  $ABO_3$  perovskite and (right) Ruddlesden-Popper with  $n=1$  layered perovskite.

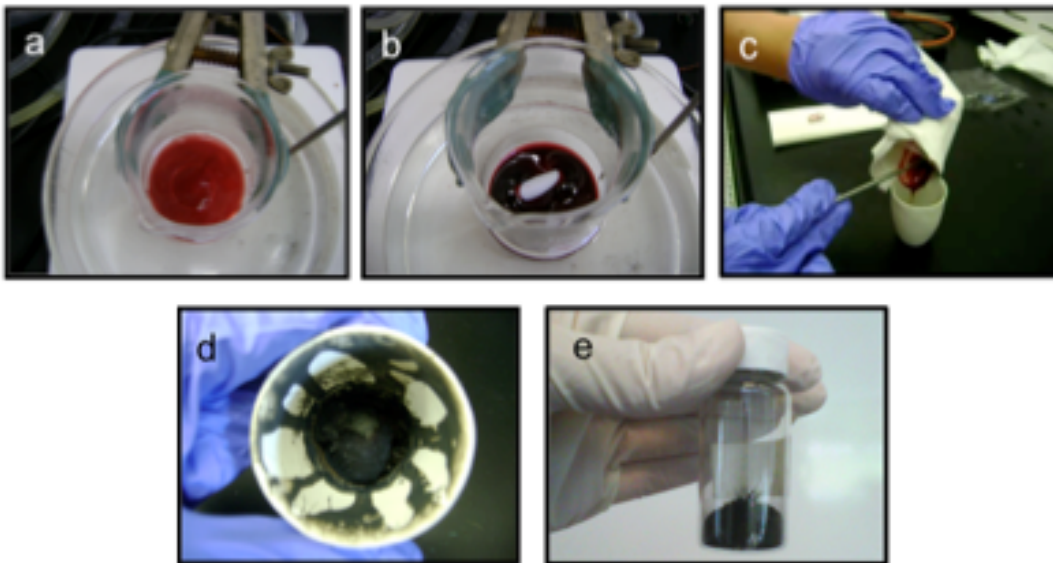


Figure 2.2 Different steps in the powders synthesis. 4.a) Citric acid aqueous solution with the cations. 4.b) Resin formed by ethylene glycol addition. 4.c) Resin transfer to the calcination ceramic recipient. 4.d) Porous powder obtained after heating at 450°C. 4.e) Perovskite powder.

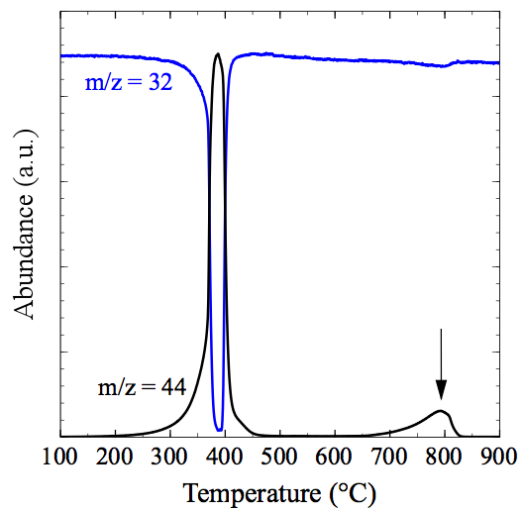


Figure 2.3 TPO profile of uncharred SrCoO<sub>3</sub> to determine the optimal charring temperature. Oxygen (m/z=32) and carbon dioxide (m/z=44) signals recorded. The arrows show the formation of the crystalline structure.

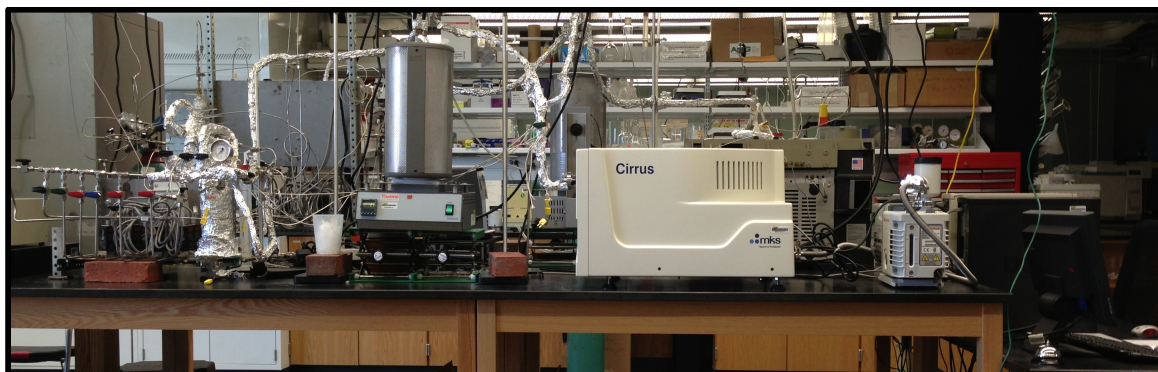


Figure 2.4 Mass spectrometer reaction set up. From left to right: mass flow controllers, furnace with U-tube reactor, Mass Spectrometer, computer.

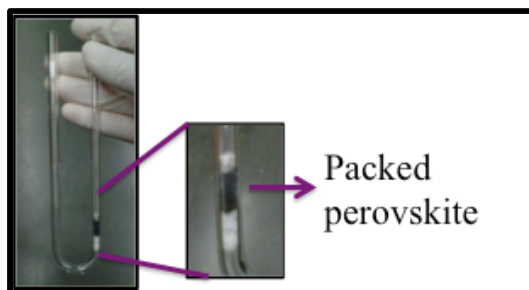


Figure 2.5 U-tube reactor packed with perovskite immobilized between glass wool



## CHAPTER 3: CARBON DIOXIDE CONVERSION BY REVERSE WATER GAS SHIFT CHEMICAL LOOPING ON PEROVSKITE-TYPE OXIDES<sup>2</sup>

### 3.1 Introduction

More than 30,000 Mt of CO<sub>2</sub> were released to the atmosphere in 2011, almost entirely due to burning coal, natural gas, and oil [105]. Yet, only around 140 Mt of these emissions are re-utilized annually as a feed for the production of fine chemicals such as urea and salicylic acid.[3] As a result, technologies for carbon capture and storage (CCS) are being developed to bridge the gap between CO<sub>2</sub> emissions and its conversion. The sequestration capacity of the presently active projects is under 40 Mt per year [106]. An analysis of these values reveals that the conversion of CO<sub>2</sub> to high production volume chemicals such as hydrocarbon fuels or methanol [107] becomes evident to significantly impact CO<sub>2</sub> emissions. In 2011, the world produced and consumed 4142 Mt of oil, from which more than 60% was for fuel production [105]. Ideally, if CO<sub>2</sub> could be transformed to fuels, a synthetic carbon loop could be closed with a feed that is both readily available and inexpensive [16, 108]. With these fuels, the carbon from CO<sub>2</sub> would provide the backbone for energy-dense liquid fuels required for transport needs in the foreseeable future.

Currently, the transformation of carbon dioxide to hydrocarbon fuels can occur by three main approaches. Thermochemical conversion yields high rates of CO production [109-112] and

---

<sup>2</sup> Reprinted with permission from Y. A. Daza, R. A. Kent, M. M. Yung, and J. N. Kuhn. Carbon dioxide conversion by reverse water gas shift chemical looping on perovskite-type oxides. *Industrial & Engineering Chemistry Research* **2014**, 53, 5828-5837. Copyright © 2014, American Chemical Society.

oxygen is simultaneously produced. Still, the high temperatures (1400 to 1600 °C) [109, 111-114] lead to energy intensive processes and infrastructure for solar concentrators results in large capital expenditures [115]. Photo-electro-catalysis systems are limited by low reaction rates, poor reaction selectivity, the inability to use a wide spectrum of visible light, and the need for continuous sources of sustainable electricity [116-118]. Finally, carbon dioxide hydrogenation through RWGS forms carbon monoxide and water, [16, 26] then hydrogen can be added to carbon monoxide to form methanol or liquid hydrocarbons by Fischer-Tropsch synthesis (FTS). Preliminary techno-economic analyses [115, 119] demonstrate cost competitiveness for methanol and diesel production as compared to other renewable options. Although RWGS is the most established of the three, it is an equilibrium-limited endothermic reaction that is favored at high temperatures. In some cases, the products must be removed to shift the equilibrium towards the RWGS rather than the forward WGS [16]. In addition, common catalysts (copper-, iron- or ceria-based systems) have poor thermal stability, and methane is commonly formed as an undesired side product [16, 26]. In spite of these drawbacks, Mallapragada et al. [42] determined that thermochemical conversion of CO<sub>2</sub> to liquid hydrocarbon fuels, with RWGS in a solar-heated reactor as a key step, was more (sun-to-fuel; STF) efficient and had the highest future estimated efficiency as compared to similar processes using land-based biomass, photosynthesis, and algae-based biomass. This comparison is based on hydrogen obtained by commercial electrolyzers operating with solar efficiencies of 10%. For these reasons, the thermochemical CO<sub>2</sub> conversion and specifically RWGS conversion are promising approaches for near-term implementation.

In this study, the reverse water gas shift reaction with chemical looping cycles (RWGS-CL) for the intensified conversion of carbon dioxide is presented. A scheme of the proposed

process is depicted in Figure 3.1. First, carbon dioxide is captured from its emissions source or separated from air and purified. The RWGS-CL operation converts CO<sub>2</sub> and H<sub>2</sub> to separate streams of CO and water. The water can be recycled, potentially to a sustainable hydrogen production system. The CO is combined with additional H<sub>2</sub> for liquid fuel production via FTS or methanol synthesis. These separate product streams eliminate the possibility of methanation as a side reaction because there is no direct interaction between CO<sub>2</sub> and H<sub>2</sub> and aid in avoiding thermodynamic limitations.

Here, a thorough study of the optimum composition of Co-based perovskite-type oxides (La<sub>1-x</sub>Sr<sub>x</sub>CoO<sub>3-δ</sub>) and conditions for the RWGS-CL are presented. These oxides are represented by an ABO<sub>3</sub> formula, where the A-site is typically occupied by lanthanides or alkaline earth metals, and the B-site is usually filled with transition metals [54-56]. With multiple cations combinations possible on each site, perovskite-type oxides can be easily customized to achieve desired properties like high oxygen mobility [56, 58]. These materials remain stable at high temperatures without aggregation, which makes them ideal for the proposed process because they can be used at the high temperatures required to achieve conversion of the stable CO<sub>2</sub> molecule.

The combination of La and Sr in the A-site and Co in the B-site enhances formation of oxygen vacancies [85, 86]. The difference in the La and Sr oxidation states generates a charge imbalance in the ABO<sub>3</sub> structure, which is stabilized by inducing some of the Co<sup>3+</sup> ions to coexist as Co<sup>4+</sup> [58, 74, 85, 87]. As the Sr substitution in the A-site increases, so does the amount of Co<sup>4+</sup> and the reducibility of the oxide in reducing conditions [56]. Aside from the cations on the A-and B-site, temperature and environment [65, 72-75], are factors that affect the reducibility of the oxides.

With high oxygen mobility and tunability, perovskite-type oxides have potential to be useful for a variety of chemical looping processes [120-122]. With CO<sub>2</sub> being a stable molecule and acidic, basic surface sites should enhance adsorption. The surface basicity of perovskite-type oxides has been described [56]. As a result, these materials would be expected to have better performance for chemical looping involving CO<sub>2</sub> conversion, than traditional metal/metal oxide pairs used (such as Fe/Fe<sub>2</sub>O<sub>3</sub>). In studies focused on chemical looping dry reforming, [49, 123] CO<sub>2</sub> was found not to be a strong oxidant for iron nanoparticles, iron oxides and iron silicates and carbon formation during the reduction of CO<sub>2</sub> was observed [49, 123].

The current study targets the use of parent perovskite-type oxides (ABO<sub>3-δ</sub>) and layered perovskite structures (AA'BO<sub>4-δ</sub>) [71] for the conversion of carbon dioxide to carbon monoxide. The schematic representation of the process is shown in Figure 3.2. When H<sub>2</sub> is flowed through the perovskite-type oxides, the oxides change phases to metallic cobalt and base oxides, which are re-oxidized back to a layered perovskite with a K<sub>2</sub>NiF<sub>4</sub>-type structure when exposed to CO<sub>2</sub>, and as a consequence, CO is produced.

### 3.2 Experimental Procedure

All gas purities are ≥99.99%. The temperature ramp rate used was 10°C/min and the total gas flow rates were held constant at 50 SCCM unless otherwise stated.

#### 3.2.1 Synthesis of Oxide Powders La<sub>1-x</sub>Sr<sub>x</sub>CoO<sub>3-δ</sub>

Following the synthesis procedure presented by Popa and Kakihana [97], La(NO<sub>3</sub>)<sub>3</sub> (Aldrich, purity 99.9%), SrCO<sub>3</sub> (Alfa Aesar, purity 99.994%) and CoCO<sub>3</sub> (Aldrich, Co 43-47%) were dissolved in an aqueous solution of citric acid (Aldrich, ACS grade ≥99.5%) at 60 °C and stirred at the same temperature for 2 h. Then, ethylene glycol (Aldrich, Reagent Plus ≥99%) was

added while stirring at 90 °C for 12 h. The compounds ratios used (A-site : B-site : citric acid : ethylene glycol = 1:1:10:40) were chosen in accordance with Ivanova et al. [78]

After the polymerization occurred, the sample was heated in air from room temperature until 450 °C at a ramp rate of 25 °C/min and was held at this temperature for 2 h. After cooling, the powders were slightly crushed. Next, a TPO-O<sub>2</sub> with 20% O<sub>2</sub>/He was performed to the samples with Sr content of X=0 and X=1 to determine their optimal charring temperature. Following, samples with a Sr content of 0≤X≤0.75 were charred in air by heating from room temperature to 700 °C at a ramp rate of 25 °C/min and were held at this temperature for 6 h, whereas the sample with X=1 was charred in air by heating from room temperature to 750 °C under the same conditions.

### 3.2.2 XRD

X-Ray Diffraction was performed in a Phillips X-Ray Diffractometer with a CuK $\alpha$  ( $\lambda = 0.154$  nm) using a step size of 0.02° at room temperature for all the fresh samples (after charring) La<sub>1-X</sub>Sr<sub>X</sub>CoO<sub>3</sub> (0≤X≤1) and for La<sub>0.75</sub>Sr<sub>0.25</sub>CoO<sub>3</sub> after a H<sub>2</sub>-reduction (10% H<sub>2</sub>/He for 30 min at 500 °C) and isothermal CO<sub>2</sub> conversion (10% CO<sub>2</sub>/He at 850 °C).

### 3.2.3 BET Surface Area

BET surface area studies were performed in a Gas Sorption System Autosorb iQ Quantachrome on the fresh samples and after a H<sub>2</sub>-reduction (10% H<sub>2</sub>/He for 30 min at 600 °C) and isothermal CO<sub>2</sub> conversion (10% CO<sub>2</sub>/He for 30 min at 850 °C).

### 3.2.4 Temperature-Programmed Reduction (TPR)

TPR experiments were performed with a thermal conductivity detector in a Gas Sorption System Autosorb iQ Quantachrome. The feed gas was a mixture of 5% H<sub>2</sub>/N<sub>2</sub>. The temperature was increased from room temperature to 800 °C where it was held for 30 min.

### 3.2.5 Temperature-Programmed Oxidation with CO<sub>2</sub> (TPO-CO<sub>2</sub>)

TPO-CO<sub>2</sub> experiments were performed in a lab-scale reactor system with multiple mass flow controllers (Alicat) and a MKS Cirrus mass spectrometer for gas-phase analysis (described elsewhere in more detail).[124, 125] The species (m/z) monitored for each gas-phase molecule are the same as described in more detail in the isothermal conversion studies. Each sample was reduced in 10% H<sub>2</sub>/He from room temperature to 600 °C and was held for 30 min. Next, the sample was cooled to 100 °C in He. Later, 10% CO<sub>2</sub>/He was flowed to the sample while undergoing heating up to 850 °C and was held at that temperature for 30 min.

### 3.2.6 Isothermal CO<sub>2</sub> Conversion

After an isothermal pretreatment (at either 400, 500, or 600 °C) under 10% H<sub>2</sub>/He for 30 min, the powders re-oxidation was studied in the reactor system described in the previous section. The reactor temperature was ramped up at a rate of 10 °C/min in He flow to specified temperatures (650, 750 and 850 °C). After the m/z signals were stable at the desired temperature, the reaction environment was changed to 10% CO<sub>2</sub>/He and was held until the carbon monoxide generation signal (m/z=28) was no longer observed. CO production was quantified with the fragmentation patterns of m/z=28. First, the nitrogen and carbon dioxide contributions to m/z=28 were subtracted. Then, the m/z=4, 28 and 44 (highest contributions of He, CO and CO<sub>2</sub>, respectively) were normalized to a total flow rate of 50 SCCM. The area under the curve was quantified with numerical integration and the moles of CO were calculated with the ideal gas law. CO was the only observed reaction product.

### 3.2.7 In-Situ XRD

In situ XRD was performed on the La<sub>1-x</sub>Sr<sub>x</sub>CoO<sub>3</sub> (X=0.25) in a Bruker D8 X Ray Diffractometer with a CuK $\alpha$  ( $\lambda = 0.154$  nm) while heating in a reducing environment (5 SCCM

H<sub>2</sub> /50 SCCM He). The heating ramp rate was 25 °C/min and was held for 10 min before the patterns were collected, at a scan rate of 2.5°/min.

### 3.2.8 Recyclability Studies

The performance of the recycled La<sub>1-x</sub>Sr<sub>x</sub>CoO<sub>3</sub> (X=0.25) was studied in the reactor system described previously. The sample was reduced under 10% H<sub>2</sub>/He for 30 min at 500 °C. Next, the temperature was ramped up in He until 850 °C was reached, here carbon dioxide was flowed (10% CO<sub>2</sub>/He) and this condition was held until the carbon monoxide generation signal was no longer observed. Afterward, the system was cooled down to 500 °C in He and the above-described procedure was repeated two more times for a total of three H<sub>2</sub>-reduction/CO<sub>2</sub>-conversion cycles. X-ray patterns of the samples were collected after each step in a Bruker X-Ray Diffractometer with a Cu K $\alpha$  ( $\lambda = 0.154$  nm) using a step size of 0.0102° at room temperature for La<sub>0.75</sub>Sr<sub>0.25</sub>CoO<sub>3</sub> fresh and after each H<sub>2</sub> pretreatment (10% H<sub>2</sub>/He for 30 min) at 500 °C and isothermal CO<sub>2</sub> conversion (10% CO<sub>2</sub>/He) at 850 °C. CO quantification was performed as described in section 3.2.6.

## 3.3 Results

### 3.3.1 Synthesis, Surface Analysis, and Bulk Structure Characterization of the (La<sub>1-x</sub>Sr<sub>x</sub>)CoO<sub>3- $\delta$</sub> Powders

The TPO performed on LaCoO<sub>3</sub> (X=0) after the esterification reaction and the first calcination at T = 450 °C is shown in Figure 3.3. At 360 °C, oxygen is consumed to form carbonate species, consistent with results [97] described elsewhere. As also discussed previously [97], a small peak at 650 °C indicated the crystallization of the amorphous powder that yields the perovskite crystalline structure. A similar experiment was performed on SrCoO<sub>3</sub> (X=1), and the crystallization peak was seen at T = 700 °C. From these experiments, calcination temperatures of

700 and 750 °C were chosen for the samples with Sr content of  $0 \leq X \leq 0.75$  and  $X=1$ , respectively. Calcination at the lowest possible temperature (as long as above the crystallization point), favors oxygen mobility [126] and higher surface area of the powders [79]. As noted in the next section, low calcination temperatures may be the source of the multi-phasic samples.

Fresh samples with Sr content of  $X=0$  were found to be rhombohedral, as commonly reported for low substituted lanthanum cobaltites [127, 128], whereas the powder with  $X=0.25$  exhibited a single-phase cubic structure (Figure 3.4). Cubic phase perovskite-type oxides have enhanced oxygen mobility and increased phase stability [56, 89]. Commonly, a pseudo cubic structure is observed with two close diffraction lines around  $33^\circ 2\theta$  (a rhombohedral structure with almost identical  $a$  and  $c$  lattice parameters). To corroborate the cubic structure, a detailed diffraction study (not shown here) was performed on the  $32.9^\circ$  diffraction line of the  $X=0.25$  sample from  $31^\circ$  to  $35^\circ 2\theta$  at  $0.005^\circ 2\theta$  step size with a scan rate of 10s /step and no evidence of a rhombohedral structure was noted. The  $\text{SrCoO}_{3-\delta}$  sample showed a hexagonal crystalline profile, consistent with other reports [129]. The powders with  $X=0.5$  and  $0.75$  contained a mixture of cubic and hexagonal phases, where the latter was probably due to a Sr-rich phase as the diffraction lines match well with the  $\text{SrCoO}_{3-\delta}$  ( $X=1$ ) sample. Traces of strontium carbonate were observed in samples with  $X=0.5$  and  $0.75$ . As mentioned in the previous section, the lowest temperature possible for the calcination of samples was kept to favor highest surface areas. As a consequence, the samples with  $X=0.5$  and  $0.75$  were found to be multiphasic. The surface areas showed no significant change between the fresh and post-reaction results (after isothermal  $\text{H}_2$ -reduction at  $600^\circ\text{C}$  and isothermal  $\text{CO}_2$ -conversion at  $850^\circ\text{C}$ ). Fresh samples possessed specific surface areas ranging from 3 to  $10\text{ m}^2/\text{g}$ ; whereas the post-reaction surface areas ranged between 3 to  $15\text{ m}^2/\text{g}$ . The results were consistent with literature [54, 55, 130, 131].



### 3.3.2 Effect of A-Site Composition on the Reducibility by H<sub>2</sub> and the Re-Oxidation by CO<sub>2</sub>

The TPR profiles shown in Figure 3.5 demonstrated the reducibility of the samples as a function of temperature and Sr content (X). Low and high temperature regions (signalized in orange and purple, respectively) were evident for each profile. The low temperature region is related to the formation of additional oxygen vacancies ( $\Delta\delta$ ) in the  $\text{La}_{1-x}\text{Sr}_x\text{CoO}_{3-\delta}$  structure [78]. In the  $\text{La}_{1-x}\text{Sr}_x\text{CoO}_{3-\delta}$  system, initial oxygen deficiencies increase with X. In other words and consistent with the findings [127] by others, higher Sr substitution leads to a high initial concentration of oxygen vacancies in the as-synthesized samples. Due to the  $\text{Sr}^{2+}$  substitution in the  $(\text{La}_{1-x}\text{Sr}_x)\text{CoO}_{3-\delta}$  system, cobalt coexisted as  $\text{Co}^{4+}$  and  $\text{Co}^{3+}$ . During the reduction, all  $\text{Co}^{4+}$  is reduced to  $\text{Co}^{3+}$  and then a portion of  $\text{Co}^{3+}$  is reduced to  $\text{Co}^{2+}$ . The high temperature region is attributed to a phase transition of the perovskite to base oxides and cobalt reduction to  $\text{Co}^0$  [63, 78].

A different reduction profile is evident between the samples where the perovskite-oxide exhibits as a cubic structure (X=0, 0.25 and 0.5) and the samples with predominant hexagonal structure (X=0.75 and 1). The sample without Sr (X=0) had the highest onset reduction temperature, whereas low Sr substituted samples (X=0.25 and 0.5) had onset temperatures of 250 °C lower. In these samples, Sr incorporation into the structure decreases the phase stability (enhances the reducibility) of the oxide [126]. Perovskite-oxides with X=0.75 and X=1, exhibit a similar reduction profile, with onset reduction temperatures of ~150 °C. Due to their predominant hexagonal or cubic-hexagonal phase mixture, they experience different structure changes than the cubic phases. As Sr substitution increases, the perovskite-oxides possess an oxygen deficient stable structure at room temperature [132], and the formation capacity of new

oxygen vacancies is lower than for a fully oxidized perovskite (where  $\delta$  is close to 0). In consequence, the oxides with  $0 \leq X \leq 0.5$  have more formation capabilities for new oxygen vacancies ( $\Delta\delta$ ) than the high Sr substituted powders, as consistent with results [127] from other studies.

The TPO-CO<sub>2</sub> profiles (Figure 3.6) showed that carbon dioxide was effectively reduced to carbon monoxide on the H<sub>2</sub>-pretreated oxides. The peak carbon monoxide formation was achieved at around 830 °C for all the reduced powders. The high-temperature nature of the reaction was a consequence of the stability of the CO<sub>2</sub> molecule. CO<sub>2</sub> reduction to CO and O<sub>2</sub> is thermodynamically unfavored and would happen spontaneously above 3000 K.

An increase in the reducibility of the perovskite resulted in a decrease in its re-oxidation ability. Although the current study is on CO<sub>2</sub> as the oxidizing agent, Nakamura and coworkers [126, 133] found a similar trend (increasing Sr-content decreased the re-oxidation ability of the reduced perovskite oxides) with O<sub>2</sub> as the oxidant. SrCoO<sub>3- $\delta$</sub>  showed two CO generation regions, suggesting that a phase transition occurred during the H<sub>2</sub> reduction and the resulting phases did not favor CO<sub>2</sub> conversion. The sample without Sr (X=0) exhibited the highest onset re-oxidation temperature (~700 °C). The lowest onset temperature (~560 °C) was achieved by the three samples with both cations on the A-site (X = 0.25, 0.5, 0.75), which suggested the existence of an optimum La/Sr ratio where the re-oxidation kinetics were fast and started at lower temperatures. Quantification of the area under the CO conversion curve below 850 °C demonstrated that the combination of La-Sr favored CO production over single metals on the A-site. La<sub>0.75</sub>Sr<sub>0.25</sub>CoO<sub>3</sub> produced the most CO below 850 °C, whereas La<sub>0.5</sub>Sr<sub>0.5</sub>CoO<sub>3</sub> produced 25% less, followed by La<sub>0.25</sub>Sr<sub>0.75</sub>CoO<sub>3</sub> with 39% less. The production area was around 50% smaller for samples containing either only La or Sr in the A-site.

The post-reaction XRD profiles (Figure 3.7) confirmed that the initial perovskite phase was not recovered after the reaction. On the contrary, for some samples, a Ruddlesden-Popper perovskite ( $A_{n-1}A'_2B_nX_{3n+1}$ ) with  $n=1$ , also called a layered perovskite or  $K_2NiF_4$  structure was formed. The abundance of the  $K_2NiF_4$  structure, has an inverse relationship to Sr content, being predominant in  $X=0$  and not detected in  $X=1$ . In the sample without Sr ( $X=0$ ), the predominant  $K_2NiF_4$  phase is orthorhombic  $La_2CoO_4$  and trace amounts of CoO were also detected. Oppositely, for the samples containing both La and Sr ( $X=0.25, 0.5, 0.75$ ), a majority of tetragonal  $La_{(2-y)}Sr_yCoO_4$  formed. The sample without La ( $X=1$ ) contained only orthorhombic  $SrCO_3$ , and metallic Co diffraction lines. As the Sr content ( $X$ ) increases, so does the abundance of  $SrCO_3$ , and Co, while the  $La_{(2-y)}Sr_yCoO_4$  is less predominant for samples with high Sr content. The  $Sr_2CoO_4$  layered perovskite structure is absent in the  $X=1$  post-reaction XRD because it is highly instable and requires high-pressures [70, 134] or a stabilizing substrate [135] to form. These findings suggested that the post-reaction samples with both La and Sr ( $X=0.25, 0.5, \text{ and } 0.75$ ) possess a  $K_2NiF_4$  structure presumably rich in La because part of the Sr was present in the  $SrCO_3$  phase.

### 3.3.3 Assessment of $La_{0.75}Sr_{0.25}CoO_3$ for $CO_2$ Conversion to CO

$La_{0.75}Sr_{0.25}CoO_3$  was selected to study isothermal conversion of carbon dioxide for the production of carbon monoxide for four reasons. First, the as-synthesized material exhibited a single-phase cubic structure without impurities. Second, the  $H_2$ -reduction profile of the sample showed a large low temperature reduction, suggesting significant oxygen vacancies formation capabilities. Also,  $CO_2$  conversion achieved in the  $H_2$ -reduced materials was maximized when  $X=0.25$ , at the lowest temperature. Finally, the post-conversion crystalline phases exhibited the

layered perovskite structure as the predominant phase, when compared to other Sr-substituted samples.

**3.3.3.1 Phase Evolution under Hydrogen as a Function of Temperature.** The in-situ XRD on  $\text{La}_{0.75}\text{Sr}_{0.25}\text{CoO}_3$  while undergoing  $\text{H}_2$ -reduction from room temperature to 600 °C (Figure 3.8) was performed. At room temperature, the fresh powder had a cubic phase consistent with the results shown in Figure 3.4. At  $T = 400$  °C (in the low temperature region), the diffraction lines shifted towards lower  $2\theta$  angles indicating an increase in the lattice parameter due to thermal expansion and oxygen vacancies formation [56, 87, 127]. The temperature increase caused the phase to begin transitioning to a layered perovskite phase ( $\text{La}_{(2-Y)}\text{Sr}_Y\text{CoO}_{4-\sigma}$ ). At  $T = 500$  °C (transition between low and high temperature region), the cubic perovskite phase was barely present and the  $\text{La}_{(2-Y)}\text{Sr}_Y\text{CoO}_{4-\sigma}$  phase had also been mostly reduced. The appearances of metallic cobalt and lanthanum oxide were noticeable. The absence of any identifiable phases containing Sr suggested that it was present in an amorphous phase or in small crystallites not detected by XRD. Further reduction above 600 °C (high temperature region) showed the predominance of  $\text{La}_2\text{O}_3$  and the disappearances of the initial cubic perovskite and the layered perovskite phases. As temperatures progresses, the powders slightly lost crystallinity. The diffraction lines at 50°, 51° and 55° seen on the profiles in Figure 3.8, were due to a quartz sample holder and remain at a fixed position throughout the experiment.

**3.3.3.2 Isothermal  $\text{CO}_2$  Conversion.** For  $\text{La}_{0.75}\text{Sr}_{0.25}\text{CoO}_{3-\delta}$ , carbon monoxide formation rates after isothermal  $\text{H}_2$ -reduction at 400, 500 and 600 °C and subsequent isothermal  $\text{CO}_2$  conversion at 650, 750 and 850 °C were measured (Table 1). For each reduction temperature, the production rates increased with increasing conversion temperature, as expected due to the stability of the  $\text{CO}_2$  molecule and the energy requirements for its activation.

CO production rates were favored when the isothermal H<sub>2</sub>-reduction was 500 °C, which coincided with the initial presence of metallic cobalt in the reduced oxides system that still contained both, according to Figure 3.8, the perovskite and perovskite layered phases. Since the lowest reduction temperature always yielded the lowest rate, the results implied that metallic Co is an important phase for reaction. An increase in the reduction temperature to 600 °C decreased the production rates, which may be caused by metallic Co aggregation. For these reasons, 500 and 850 °C were chosen as the isothermal reduction and conversion temperatures, respectively. For comparative purposes, Co<sub>3</sub>O<sub>4</sub> was tested using these conditions and the rate was 113.9 μmole CO/g/min (34% lower) despite having ~3 times as many Co atoms per mass as La<sub>0.75</sub>Sr<sub>0.25</sub>CoO<sub>3-δ</sub>.

**3.3.3.3 Recyclability.** As presented in Table 3.2, the amount of CO produced on each CO<sub>2</sub> conversion cycle, showed a maximum production during the first CO<sub>2</sub> conversion (Post-rxn1 in Figure 3.9). Then, CO production amount decreased ~25% during the second CO<sub>2</sub> conversion (Post-rxn2) and remained constant for the third re-oxidation (Post-rxn3). The crystallite size was calculated using Scherrer equation with K=1. The fresh material had a crystallite size of 17.7 nm (calculated from the peak positioned at 32.9°). After the first H<sub>2</sub>-reduction (R1), the crystallite size increased to 29.7 nm (calculated from the peak positioned at 29.9°) and during the subsequent treatments (Post-rxn1 and later), it was only slightly larger at 33.9 nm (calculated from the peak positioned at 31.4°). The CO formation amount and the crystallite size of the structures suggested that the phases formed during the first reduction (R1) were different than the ones formed during subsequent reductions (R2 and R3), and that the crystalline structures during Post-rxn2 and subsequent steps were similar. Furthermore, CO

yields indicated that CO<sub>2</sub> conversion was favored by phases formed during R1 in comparison to the ones formed during R2 and R3.

Changes in the crystalline structures formed after each step of the cycle are presented in Figure 3.9, which has been normalized from 0 to 1 for each pattern. The cubic perovskite structure was initially present. After the first reduction (R1), a significant amount of the initial perovskite was reduced to La<sub>2</sub>O<sub>3</sub>, metallic Co and SrCO<sub>3</sub>. The perovskite diffraction lines shifted towards lower angles, indicating an increase in lattice parameters due to oxygen vacancies formation which caused some of the Co<sup>3+,4+</sup> to reduce to Co<sup>2+</sup>. Only one Sr species was detected in one diffraction line of SrCO<sub>3</sub>, suggesting that amount of SrCO<sub>3</sub> is small and/or most of the Sr was present as an amorphous structure. A ratio comparison of the highest intensity peak of La<sub>2</sub>O<sub>3</sub> to SrCO<sub>3</sub> suggested that the initial perovskite could present a lower La/Sr ratio, which would also cause the perovskite to increase its lattice parameters and shift towards lower 2θ angles. After the first reaction (Post-rxn1), Co<sup>0</sup> and La<sub>2</sub>O<sub>3</sub> were oxidized to CoO and La<sub>2-y</sub>Sr<sub>y</sub>CoO<sub>4</sub>, respectively. Sr was then present in two phases, SrCO<sub>3</sub> and the K<sub>2</sub>NiF<sub>4</sub> structure. The presence of Sr in the SrCO<sub>3</sub> structure suggested that the La<sub>2-y</sub>Sr<sub>y</sub>CoO<sub>4</sub> phase contains a higher La/Sr than the perovskite after R1. From this cycle step forward, the predominant crystalline phases remained La<sub>2-y</sub>Sr<sub>y</sub>CoO<sub>4</sub> and SrCO<sub>3</sub>.

The main diffraction line for CoO (42.3°) decreased in the reduced phases (R2 and R3) as the metallic Co diffraction line increased (44.3°). Co was not detected in the re-oxidized phases (Post-rxn2 and Post-rxn3) and the intensity of the main CoO diffraction line increased. The difference observed between the crystalline structure found at 500 °C during the in-situ TPR (Figure 3.8) and the crystalline structure after isothermal H<sub>2</sub>-reduction at 500 °C (Figure 3.9-R1) was expected. During the in-situ experiments, the time the sample had undergone reduction at

500 °C was longer than the 30 min the sample spent under the isothermal reduction. As a consequence, during the in-situ XRD while undergoing TPR, the sample was further reduced and the perovskite structure could not be detected.

### 3.4 Discussion

#### 3.4.1 Role of Metallic Cobalt in the Reduction of Carbon Dioxide to Carbon Monoxide

Carbon dioxide adsorption onto perovskite-type oxides has been explained before [136], but contradicting points of view exist on the role that metallic cobalt could be playing in CO<sub>2</sub> adsorption/dissociation. Carbon dioxide could adsorb either dissociatively [137] or molecularly [138] onto metallic Co. Based on the experimental results here presented, two mechanism routes are proposed. First, carbon dioxide could adsorb on the layered perovskite [56], and then dissociate into CO and O. Then, the O atom could spillover into the metallic cobalt, oxidizing it into CoO and yielding CO as the only gas phase product. Second, carbon dioxide could chemisorb onto the metallic cobalt and dissociate into CO and O [137]. Following, O could re-oxidize the metallic cobalt into CoO while releasing CO. Both of these explanations would justify why the conversion was highest when the H<sub>2</sub>-reduction formed metallic cobalt (at 500 and 600 °C). In addition, the diffraction lines of the layered perovskite in the recyclability studies do not show evidence of oxygen vacancies formation or re-oxidation, which suggested that the layered perovskite La<sub>2-y</sub>Sr<sub>y</sub>CoO<sub>4</sub> could be stabilizing the Co<sup>0</sup> particles (rather than participating directly by oxidizing), preventing sintering during the H<sub>2</sub> reduction step. This claim is supported by comparison of CO production rate of the reduced La<sub>0.75</sub>Sr<sub>0.25</sub>CoO<sub>3- $\delta$</sub>  to that of Co<sub>3</sub>O<sub>4</sub>. As a result, CO<sub>2</sub> conversion rates would increase due to the small crystallites having faster re-oxidation kinetics.

### 3.4.2 Comparison of RWGS-CL to Other Techniques

Carbon monoxide production from carbon dioxide via the RWGS-CL process is compared to two-step thermochemical cycles, RWGS, and photochemical conversion with respect to materials, reaction temperatures and environment. A summary of the comparison is presented in Table 3. Studies that reduced CO<sub>2</sub> to C and O<sub>2</sub> [48, 51, 52, 123] will not be considered in the discussion.

**3.4.2.1 Thermochemical Cycles.** A variety of oxides with high oxygen mobility such as cerium oxide [109, 111-113], partially substituted cerium oxide [74, 114], and perovskite oxides [113], as well as base oxides [114], have been studied for CO<sub>2</sub> conversion. In general, partially substituting an oxide such as introducing Zr in CeO<sub>2</sub>[112] increases the rate of carbon monoxide formation. Using oxides with higher oxygen mobility than CeO<sub>2</sub> also increases reaction rates [112, 114], but a consensus on the optimum material has not yet been achieved. Even though Scheffe et al. [110] determined that La<sub>1-x</sub>Sr<sub>x</sub>MnO<sub>3-δ</sub> perovskites would be thermodynamically favored to become oxygen deficient at lower temperatures than ceria, the materials were unfavored to re-oxidize with carbon dioxide. McDaniel et al. [113] observed CO formation on oxygen deficient La<sub>1-x</sub>Sr<sub>x</sub>Mn<sub>1-y</sub>Al<sub>y</sub>O<sub>3-δ</sub> perovskite-type oxides, although with low CO formation rates, for as many as 80 cycles.

Hydrogen use is particularly attractive when the reaction temperatures between two-step thermochemical cycle and RWGS-CL processes are compared. The temperature needed for the oxygen desorption of the oxides (first step of thermochemical cycles) is at least 1350 °C [113], which is around 1000 °C more than the lowest reduction temperature used in this study. Moreover, CO<sub>2</sub> reduction temperatures for thermochemical cycles were at least 150 °C higher [109] than the lowest conversion temperatures used with RWGS-CL (650 °C). The CO



production rates observed in this study are within the same order of magnitude than the highest rates observed in two-step thermochemical cycles [109]. The technical trade-offs of this comparison is that the RWGS-CL process uses hydrogen to obtain materials more reactive with CO<sub>2</sub> and low temperatures whereas the two-step thermochemical cycles use higher temperatures with material less reactive with CO<sub>2</sub> to achieve similar rates. In both the two-step thermochemical and the RWGS-CL processes, the ability of CO<sub>2</sub> to re-oxidize the pre-treated material is a key feature. Depending on the original material used and the environment, the time needed to complete the CO<sub>2</sub> re-oxidization step can vary significantly. Therefore, in addition to reaction rates, the amount of CO produced per mass of initial oxide (labeled as amount in Table 3) can be a valuable tool in determining which oxides are favored towards the redox cycles with CO<sub>2</sub> as the oxidant. In general, the mass-normalized CO production amounts increases in partially substituted oxides when compared to the base oxides [112, 113]. The mass-normalized CO production amounts observed during this study are one order of magnitude higher than other results (see Table 3.3), suggesting that a H<sub>2</sub>-treatment of the perovskite and layered perovskite oxides results in maximum CO production at low temperatures compared to re-oxidation during thermo-chemical cycles.

Another important manner for comparison is the techno-economic assessments. The two-step thermochemical process driven by concentrated solar energy requires a special reactor system and a solar field, which both increase the capital costs [115]. Solar concentrators are being scaled up to heat water for electricity generation, but concentrators for thermochemical cycles are further away from larger scale studies. In light of these challenges, a techno-economic analysis [119] estimated that the minimum selling price of gasoline from a H<sub>2</sub>O-splitting/CO<sub>2</sub>-splitting (with solar concentrators) process with incorporated FTS as 7.01 US\$ per gallon of

gasoline equivalent. Alternatively, solar-thermo-chemical approaches, such as those already described by Mallapragada et al., [42] require renewable H<sub>2</sub> and most of the solar energy is directed towards its production. A review of estimates of renewable hydrogen production costs indicated 6.5 USD/KgH<sub>2</sub> [139] and the cost has been proposed [107] to decrease by roughly half in the upcoming decades. At 6.5 USD/KgH<sub>2</sub>, the cost of hydrogen roughly contributes \$3.80 to the cost per gallon of gasoline. With the renewable hydrogen production being a major contributor to the cost, it suggests that these two processes are within the same order of magnitude on cost. A direct techno-economic comparison between solar-thermo-chemical and thermochemical cycles processes has not yet been published, so it is unclear as to which method would be less expensive and the degree of success in the price reduction of renewable hydrogen is a major contributor.

**3.4.2.2 RWGS.** Carbon dioxide hydrogenation to form carbon monoxide and steam through RWGS takes place at temperatures as low as 400 °C [140]. At this condition, the process is thermodynamically unfavored and the equilibrium is shifted towards the reactants. RWGS-CL avoids the need for separation of the products because they are being formed independently, so the reaction can be driven forward without the need for increasing the reactants concentration or removing products. During the experiments performed in this work, there was no evidence of other products aside CO such as methane, as generally seen in RWGS [16, 26, 141, 142]. Common carbon monoxide production rates in the RWGS differ in one or two orders of magnitude (4.3 [142] to 850 [143]). These variations could be a consequence of a combination of different conditions at the feed and different catalysts. Although varying significantly, the higher RWGS rates are within the same order of magnitude than the rates found in this study. In addition, RWGS-CL does not require flow of excess hydrogen, which potentially translates to

lower H<sub>2</sub> consumption when compared to RWGS, which commonly uses H<sub>2</sub> in stoichiometric excess [16, 26, 143].

**3.4.2.3 Photochemical.** In general, photochemical reduction offers the advantage of CO<sub>2</sub> conversion at or near room temperature. The use of water [116, 117] instead of hydrogen as a proton source makes it advantageous when compared to RWGS-CL. However, low formation rates, long batch reaction times, low product selectivity, and dependence on the use of precious metals [116-118] all present major challenges for applying this technology. The RWGS-CL process is competitive when compared to the photochemical processes because its reaction times are approximately an order of magnitude quicker than batch reaction times for CO<sub>2</sub>-photo-reduction (see Table 3). Also, the mass-normalized CO production amount obtained with the RWGS-CL process is higher than the ones obtained by the common catalyst used in the photochemical CO<sub>2</sub> conversion [116-118]. As a result, even though photochemical approach may provide the best long-term route, further developments are needed and thermochemical approaches provide improved short-term impact.

### 3.5 Summary

A series of La<sub>1-x</sub>Sr<sub>x</sub>CoO<sub>3-δ</sub> (X = 0, 0.25, 0.50, 0.75, and 1) materials were synthesized, characterized, and examined for CO<sub>2</sub> conversion. Initial temperature-programmed studies determined that La<sub>0.75</sub>Sr<sub>0.25</sub>CoO<sub>3-δ</sub> had highest structure stability under reducing environments and the greatest CO production capacity during re-oxidation by CO<sub>2</sub>. For that reason, this sample was selected for further experimental evaluation. Isothermal CO<sub>2</sub> conversion studies demonstrated that the optimal isothermal reduction and conversion temperatures for maximizing the CO production rates were 500 °C (of 400, 500 and 600 °C) and 850 °C (of 650, 750 and 850 °C), respectively. Post-reaction XRD studies indicated that the initial perovskite structure phases

were converted to a layered perovskite structure ( $\text{La}_{2-y}\text{Sr}_y\text{CoO}_4$ ), which occurred likely because of the poor oxidation ability of  $\text{CO}_2$ . The optimal reduction temperature to maximize the CO production rate correlated to when the layered perovskite ( $\text{La}_{2-y}\text{Sr}_y\text{CoO}_4$ ) was in close contact with metallic Co. This sample was then stable for at least three cycles of reduction-conversion, as demonstrated by XRD and isothermal  $\text{CO}_2$  conversion experiments. The high CO production per mass of material, the inherent separation and selectivity achieved, and the recyclability of the process make the use of RWGS-CL promising as a plausible scalable  $\text{CO}_2$  reduction technology for the formation of  $\text{C}_1$  feeds. If a renewable hydrogen source is used, the entire conversion system could potentially become sustainable.

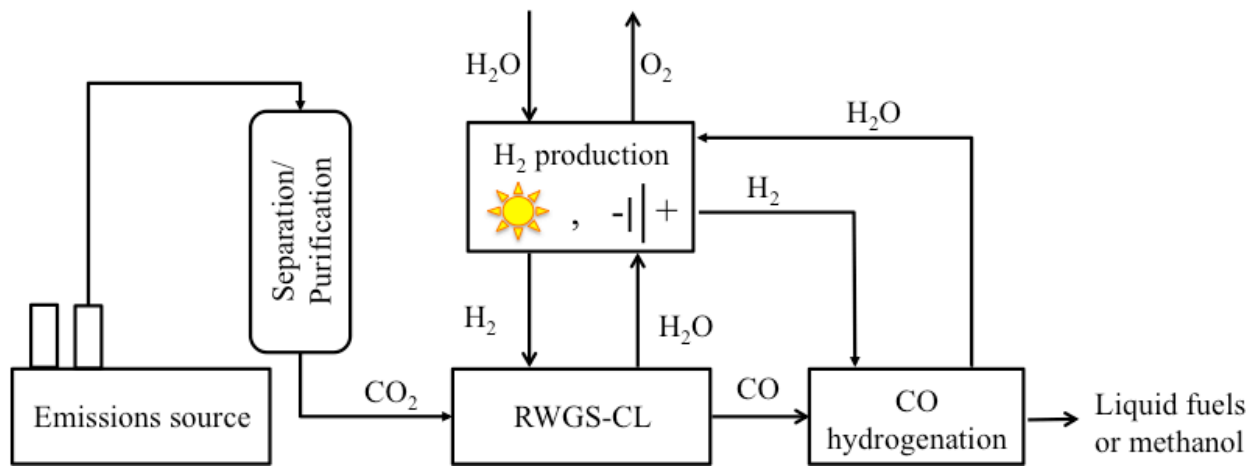


Figure 3.1 Schematic representation of the overall proposed process. Captured  $\text{CO}_2$  is flowed through the  $\text{H}_2$ -reduced oxides in the RWGS. The  $\text{CO}$  produced is fed to a  $\text{CO}$  hydrogenation reactor for fuel production.

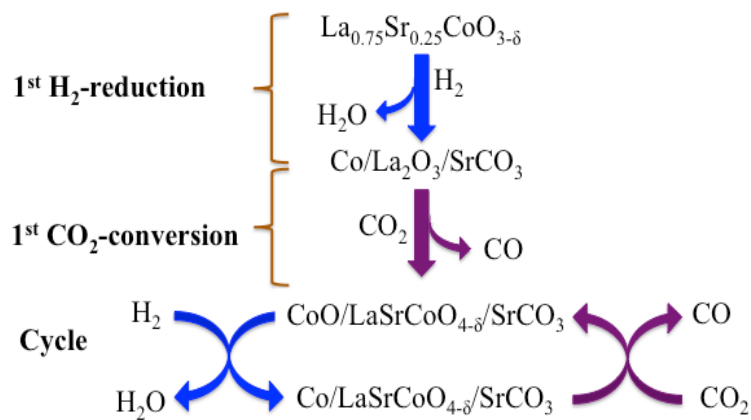


Figure 3.2 Schematic representation of  $\text{CO}_2$  conversion to  $\text{CO}$  on the oxygen deficient oxide system. A  $\text{H}_2$  treatment reduces the perovskite-type oxides to metallic cobalt and base oxides while producing water. With  $\text{CO}_2$  present, the reduced phases re-oxidize producing  $\text{CO}$ .

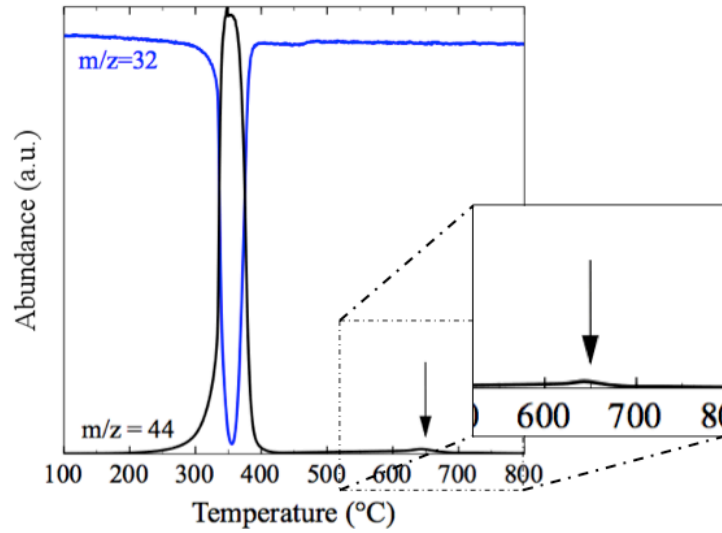


Figure 3.3 TPO profile of uncharred  $\text{LaCoO}_3$  to determine the optimal charring temperature. Oxygen ( $m/z=32$ ) and carbon dioxide ( $m/z=44$ ) signals are shown. The carbonates formation at  $650^\circ\text{C}$  shows the formation of single phase perovskite structure.

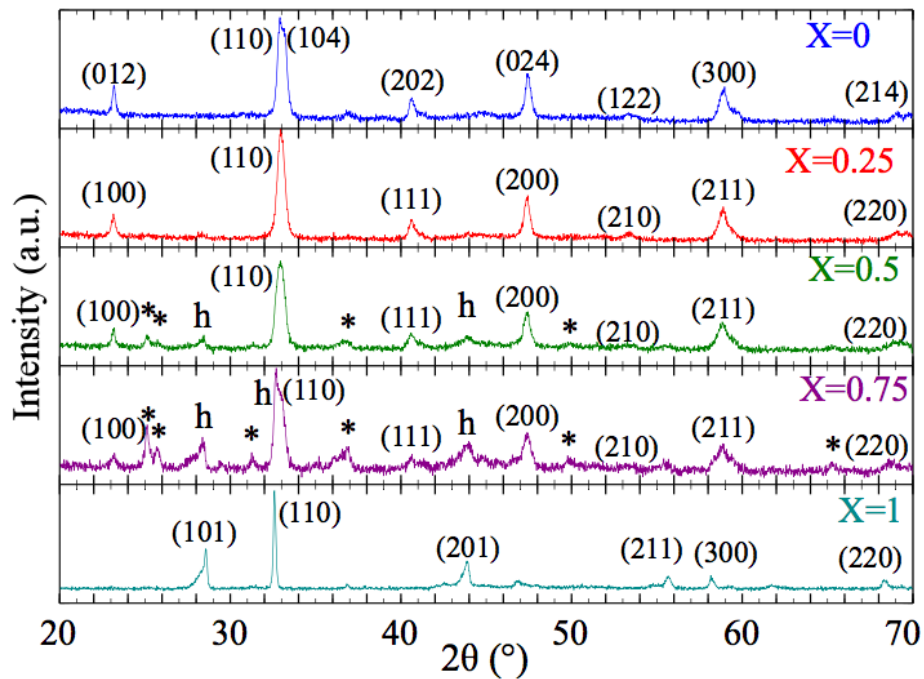


Figure 3.4 X-ray diffraction patterns of fresh  $(\text{La}_{1-x}\text{Sr}_x)\text{CoO}_{3-\delta}$  powders. The fresh powders with  $X=0$ ,  $X=0.25$  and  $X=1$  presented single-phase crystalline structures (rhombohedral, cubic and hexagonal, respectively). Powders with  $X=0.5$  and  $X=0.75$  presented predominantly cubic structure, with a mixture of hexagonal (h) and  $\text{SrCO}_3$  (\*) which increase with  $X$ .

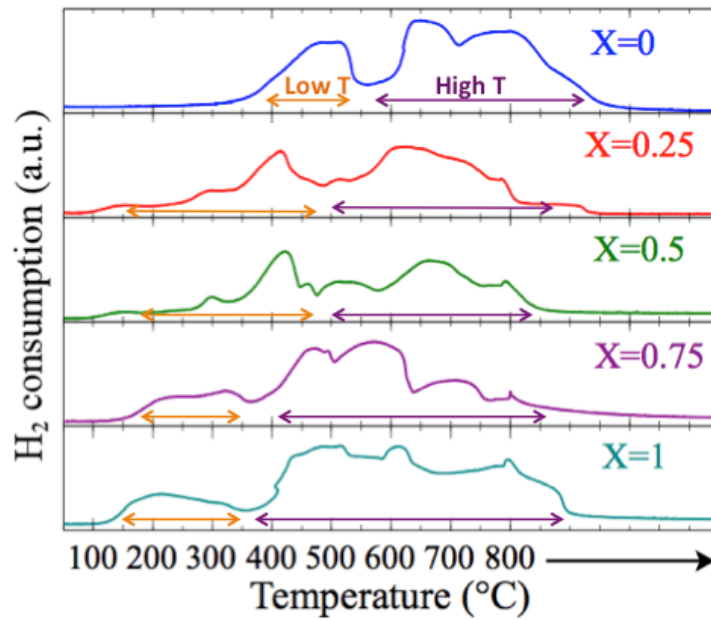


Figure 3.5 Temperature-programmed reduction with 5% $H_2/N_2$  of  $(La_{1-x}Sr_x)CoO_{3-\delta}$  samples.

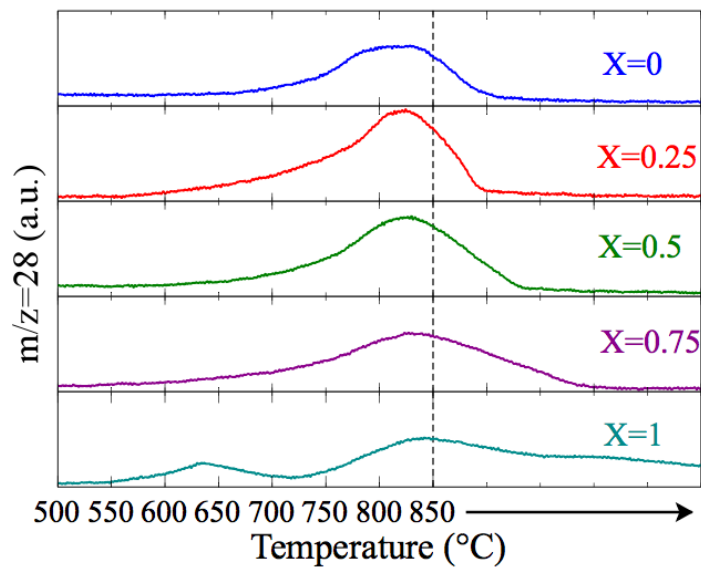


Figure 3.6 Carbon monoxide generation with 10% $CO_2/He$  using  $H_2$ -pretreated  $(La_{1-x}Sr_x)CoO_{3-\delta}$ .

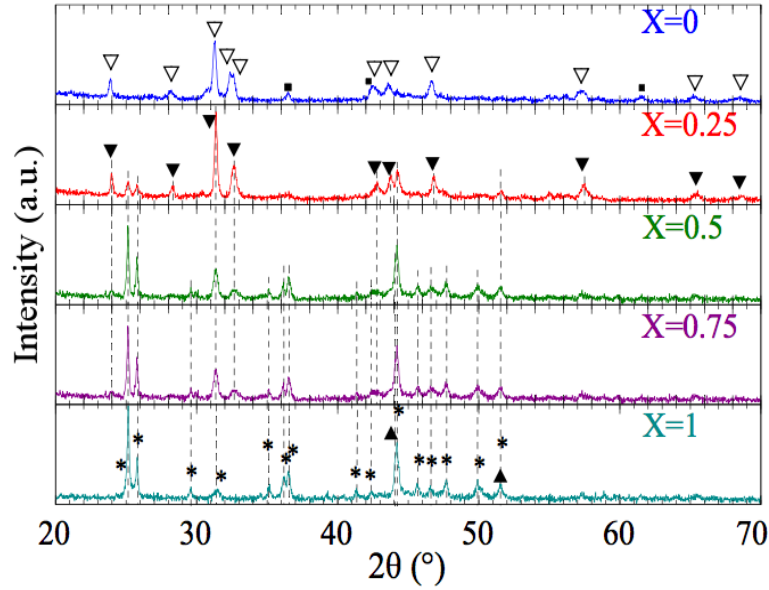


Figure 3.7 X-ray diffraction patterns of  $(\text{La}_{1-x}\text{Sr}_x)\text{CoO}_{3-\delta}$  samples after a 10%  $\text{H}_2/\text{He}$  pretreatment at 600 °C and after isothermal  $\text{CO}_2$  conversion with 10%  $\text{CO}_2/\text{He}$  at 850 °C. Phases found:  $\text{SrCO}_3$  (\*),  $\text{La}_{2-y}\text{Sr}_y\text{CoO}_4$  (▼),  $\text{La}_2\text{CoO}_4$  (▽),  $\text{CoO}$  (■) and  $\text{Co}$  (▲).

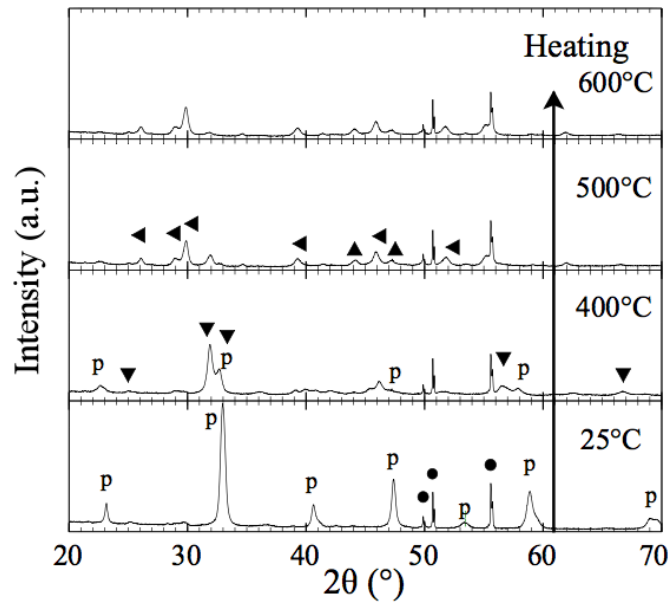


Figure 3.8 Changes in  $\text{La}_{0.75}\text{Sr}_{0.25}\text{CoO}_{3-\delta}$  crystalline structure while it is heated in 10%  $\text{H}_2/\text{He}$ . Phases observed include  $\text{La}_{0.75}\text{Sr}_{0.25}\text{CoO}_{3-\delta}$  (p),  $\text{La}_{2-y}\text{Sr}_y\text{CoO}_4$  (▼),  $\text{Co}$  (▲),  $\text{La}_2\text{O}_3$  (◄), and quartz sample holder (◻). All diffraction patterns are normalized to the most intense line in the room temperature pattern.



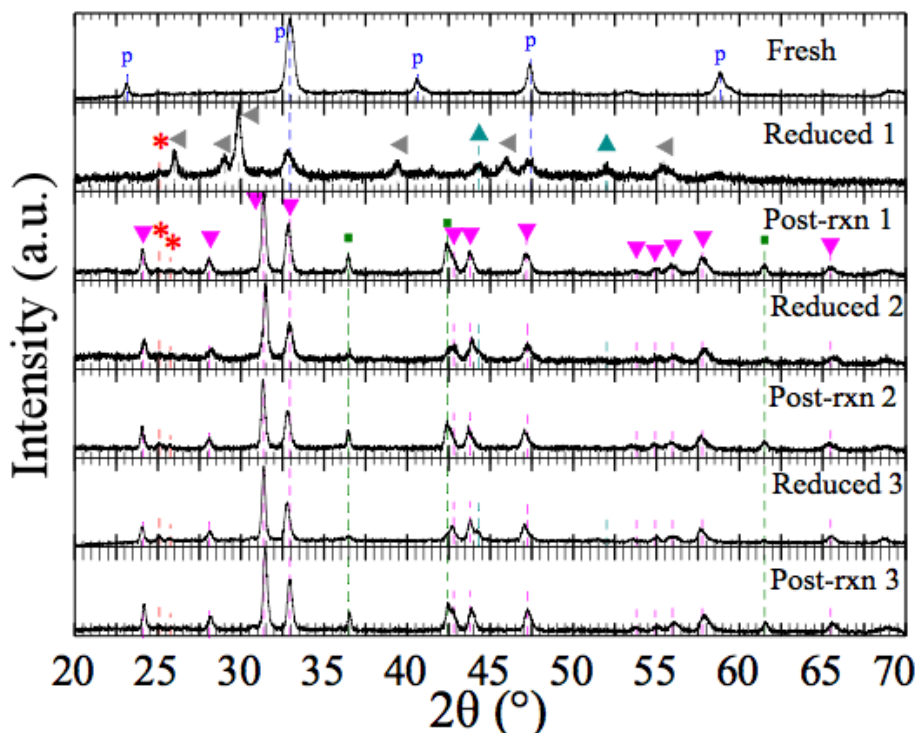


Figure 3.9 Changes in  $\text{La}_{0.75}\text{Sr}_{0.25}\text{CoO}_{3-\delta}$  crystalline structure throughout the cycles. Phases observed include  $\text{La}_{0.75}\text{Sr}_{0.25}\text{CoO}_{3-\delta}$  (p),  $\text{La}_{2-\text{Y}}\text{Sr}_{\text{Y}}\text{CoO}_4$  (▼),  $\text{SrCO}_3$  (\*),  $\text{La}_2\text{O}_3$  (◄), Co (▲), and CoO (■).

Table 3.1 CO generation rate during the first ten min of the reaction.

Rate		$\left(\frac{\mu\text{mol of CO}}{\text{grams of perovskite} * \text{min}}\right)$		
Sample	Red. T / Conv. T	650 °C	750 °C	850 °C
$\text{La}_{0.75}\text{Sr}_{0.25}\text{CoO}_{3-\delta}$ ●	400 °C	14.7	65.7	146.3
	500 °C	38.0	98.4	172.6 ± 17.4 <sup>a</sup>
	600 °C	20.6	73.4	198.1

<sup>a</sup> Experiment was performed three times.

Table 3.2 CO produced during the cycles of  $\text{H}_2$  reduction and  $\text{CO}_2$  re-oxidation of  $\text{La}_{0.75}\text{Sr}_{0.25}\text{CoO}_{3-\delta}$ .

$\text{CO}_2$ conversion cycle	CO (μmol)
First $\text{CO}_2$ conversion	302.5
Second $\text{CO}_2$ conversion	226.5
Third $\text{CO}_2$ conversion	226.7

Table 3.3 Rates and evolution of CO produced on different materials at STP conditions.

Method	Material	Treatment T (°C)	Conversion T (°C)	Amount (μmol CO/g)	Rate (μmol CO/min/g)	Reaction time (min)	Cycles	Reference
RWGS-CL	$\text{La}_{0.75}\text{Sr}_{0.25}\text{CoO}_{3-\delta}$	500 (under $\text{H}_2$ )	850	4032.8 <sup>c,d</sup>	100.8 <sup>c,d</sup>	40	3	This work
Two step thermochemical	$\text{CeO}_2$	1600 <sup>a,b</sup>	900	278.3	74.2 <sup>d,e</sup>	3.75 <sup>i</sup>	4	Chueh et al.[109]
		1500 <sup>a</sup>	800	781.8	208.5 <sup>d,e</sup>		NA	
	$\text{CeO}_2$	1400 <sup>a</sup>	1200	98 <sup>c</sup>	2.8	35	3	Le Gal et al.[112]
	$\text{Ce}_{0.75}\text{Zr}_{0.25}\text{O}_2$ <sup>f</sup>			142 <sup>c</sup>	4.1			
	$\text{CeO}_2$	1600 <sup>a,b</sup>	Cool from $T_{\text{red}}$ to ~300	232.6 <sup>e</sup>	6.5	36 <sup>h</sup>	NA	Furler et al.[111]
	$\text{CeO}_2$	1350 <sup>a</sup>	1000	46	3.4	13.4 <sup>g</sup>	NA	McDaniel et al.[113]
	$\text{Sr}_{0.4}\text{La}_{0.6}\text{Mn}_{0.6}\text{Al}_{0.4}\text{O}_{3-\delta}$			294	21.9			
	$\text{Sr}_{0.6}\text{La}_{0.4}\text{Mn}_{0.6}\text{Al}_{0.4}\text{O}_{3-\delta}$			286	21.3			
	$\text{Sr}_{0.4}\text{La}_{0.6}\text{Mn}_{0.4}\text{Al}_{0.6}\text{O}_{3-\delta}$			247	18.4			
	$\text{Sr}_{0.6}\text{La}_{0.4}\text{Mn}_{0.6}\text{Al}_{0.4}\text{O}_{3-\delta}$			140 <sup>g</sup>	9.3			
	$\text{Co}_{0.67}\text{Fe}_{2.33}\text{O}_4/\text{YSZ}$	1400 <sup>a</sup>	1100	127.8 <sup>e</sup>	0.7	180 <sup>g</sup>	7	Miller et al.[114]
$\text{Ce}_{0.25}\text{Zr}_{0.75}\text{O}_2$	1400 <sup>a</sup>	1100	144.9 <sup>e</sup>	0.5	310 <sup>g</sup>	NA		

Table 3.3 (Continued).

Method	Material	Feed	Conversion T (°C)	Amount (μmol CO/g)	Rate (μmol CO/min/g)	Reaction time (min)	Cycles	Reference
Photo-chemical	Cu/Pt/TiO <sub>2</sub>	CO <sub>2</sub> + H <sub>2</sub> O <sub>(l)</sub>	49.85	33.12	0.138	240	NA	Zhai et al.[116]
	5% Au/ZnO	H <sub>2</sub> /CO <sub>2</sub> : 3/1	RT raised to 650 with plasmonics	20.1	0.067	300	5	Wang et al.[118]
	1% Au/SrTiO <sub>3</sub>	CO <sub>2</sub> + H <sub>2</sub> O <sub>(l)</sub>	RT	8.64	0.006	1440	NA	Zhou et al.[117]
Method	Material	Feed	Conversion T (°C)	Rate (μmol CO/min/g)	Time-on-stream (min)	Reference		
RWGSR	Cu/Al <sub>2</sub> O <sub>3</sub>	H <sub>2</sub> /CO <sub>2</sub> : 1/9	~500	540 <sup>i,g</sup>	60	Chen et al.[141]		
	2% Pt/CeO <sub>2</sub>	H <sub>2</sub> /CO <sub>2</sub> : 4/1	290	842.45 <sup>i</sup>	1200	Goguet et al.[143]		
	Pd/CeO <sub>2</sub> (10) /Al <sub>2</sub> O <sub>3</sub> aged	H <sub>2</sub> /CO <sub>2</sub> : 1/1	260	4.3 <sup>i</sup>	NA	Pettigrew et al.[142]		

<sup>a</sup> Under inert environment. <sup>b</sup> Concentrated solar. <sup>c</sup> First cycle. Note that values are lower than corresponding results of Table 3.1 because the reaction time to complete CO production is used here. <sup>d</sup> Average rate. <sup>e</sup> μmol of CO calculated with ideal gas law from volumetric rates. <sup>f</sup> Synthesized by the Pechini method. <sup>g</sup> Estimated from figure in reference. <sup>h</sup> Calculated from mean specific and total specific CO evolution values in Table 1 from reference [111]. <sup>i</sup> Calculated from the yields with ideal gas law.

## CHAPTER 4: ISOTHERMAL REVERSE WATER GAS SHIFT CHEMICAL LOOPING

### ON $\text{La}_{0.75}\text{Sr}_{0.25}\text{Co}_{(1-Y)}\text{Fe}_Y\text{O}_3$ PEROVSKITE-TYPE OXIDES<sup>3</sup>

#### 4.1 Introduction

In 2011, the total CO<sub>2</sub> emissions exceeded 30,000 Mt [105], but less than 1% of the CO<sub>2</sub> produced is re-purposed in industrial processes [3]. Since late 2010, the EPA began contemplating setting restrictions to CO<sub>2</sub> emissions from stationary sources [144]. In particular, the EPA has promoted the use of alternative technology by CO<sub>2</sub> emitters including coal plants for emission reduction. Current efforts to decrease CO<sub>2</sub> emissions are dominated by carbon capture and storage (CCS), also called carbon sequestration. CCS is considered a potential CO<sub>2</sub> mitigation technique, but even at the top of its estimated storage capacity (120 Mt per year [145]), CCS will not be able to mitigate more than 1% of the global CO<sub>2</sub> emissions. In addition, CO<sub>2</sub> emissions are expected to increase due to population and economic growth. Here, an alternative to CCS is proposed, where CO<sub>2</sub> can be transformed to high-value chemicals needed to close a synthetic carbon cycle.

A potentially sustainable way to close a CO<sub>2</sub>-hydrocarbon cycle is to convert CO<sub>2</sub> to CO, as an intermediate step to synthesize liquid fuels [16]. Recently, Mallapragada et al. [42] performed a techno-economic analysis on the conversion of CO<sub>2</sub> to fuels by different approaches including using algae, photosynthesis and the reverse water gas shift reaction (RWGS). The

---

<sup>3</sup> Reprinted with permission from Y. A. Daza, D. Maiti, R. A. Kent, V. R. Bhethanabotla, and J. N. Kuhn. Isothermal reverse water gas shift chemical looping on  $\text{La}_{0.75}\text{Sr}_{0.25}\text{Co}_{(1-Y)}\text{Fe}_Y\text{O}_3$  perovskite type oxides. *Catalysis Today* **2015**, 258, 691-698. Copyright © 2015 Elsevier

study determined the RWGS process, operated at equilibrium at 976 °C and 30 atm, as the method with the highest estimated current and future efficiency. In this process, solar energy was used to heat the reactor to this temperature and to power electrolyzers, which provided the H<sub>2</sub> for the process. In analyzing the solar energy use in the overall process, the dominant need was to generate H<sub>2</sub> for the RWGS and CO hydrogenation reactions. Thus, improvements in the efficiency of H<sub>2</sub> use would aid in making the process more economically feasible.

Previously, we have developed the reverse water gas shift chemical looping (RWGS-CL) process on Co-based perovskites [45]. The RWGS-CL is a two-step process for the conversion of CO<sub>2</sub> to CO using a redox cycle of a parent metal oxide. The first step of the process is the reduction by H<sub>2</sub> of the parent metal oxide and the second step is the oxidation of the reduced material by CO<sub>2</sub> with CO forming. By performing the RWGS-CL rather than RWGS catalysis, H<sub>2</sub> use can be minimized by conducting stoichiometric reactions without the need of excess H<sub>2</sub> for kinetic and thermodynamic reasons and avoiding the side methanation reaction by inherently keeping the H<sub>2</sub> and CO separated. In our original report [45], Co stabilized on a layered perovskite oxide support was the active phase for CO<sub>2</sub> conversion and was formed by H<sub>2</sub> reduction at 500 °C. The use of hydrogen allows for the generation of the active phases in the perovskite, at temperatures ~500 °C lower than thermochemical studies with active phases generated by extensive heating performed on similar oxides [109, 111-114], but causes the Co-based perovskite to change crystalline phases. The second step is a CO<sub>2</sub> re-oxidation of the material, which yielded increasing CO generation rates with rising temperature. The obtained rates for CO formation on metallic cobalt supported on layered perovskite were competitive with RWGS [141-143], and significantly improved in comparison to photochemical reactions [116-

118]. But still, the minimum temperature for generation of CO was 650 °C and the highest rate was obtained at the highest temperature tested (850 °C).

Although this initial study with Co-based materials showed promise, there is a desire to lower the temperatures in the process and to use the same temperature (referred to as an isothermal cycle) for both steps in the process. Operation at lower temperatures allows for use of less expensive materials (i.e., stainless steel) in the reactor and reduces the potential heat losses in the system. Isothermal operation would decrease process inefficiencies caused by cycling between temperatures. Iron use is popular in oxygen carrier materials for chemical looping because of its non-toxic nature, low carbon formation, low cost and low tendency towards agglomeration [146, 147]. In addition, there is both experimental [51, 52, 123, 148] and computational [137] evidence that the use of Fe or Fe with Co in the perovskite phase would aid in lowering the temperatures in the RWGS-CL process.

Experimentally, two groups have studied conversion of CO<sub>2</sub> to CO by oxidizing a hydrogen reduced Fe-containing material. Bhavsar et al. [123, 148] studied CO<sub>2</sub> conversion on a three-step Chemical Looping Dry Reforming (CLDR) process using Fe-based oxides and supported Fe particles at 800 °C with either H<sub>2</sub> [123] or CH<sub>4</sub> [148] as the reducing agent. The three-step nature of the process is due to the poor oxidizing nature of CO<sub>2</sub>, which led to incorporation of a second oxidant (oxygen from air) to recuperate the original structure of the oxygen carrier. Similarly, Nordhei et al. [51] demonstrated CO<sub>2</sub> conversion to CO and C(s) at 300 °C, by incorporating Co, Zn and Ni into Fe-based spinels. The same group showed that by reducing Co-substituted Fe-spinels at 500 °C, a Co-Fe alloy was formed and both metals participate in the conversion of CO<sub>2</sub> to CO and C(s). Furthermore, a mixture of Co and Fe enhances CO<sub>2</sub> conversion when compared with the base material (Fe-spinel) [52]. It is unclear if

the CO production rates obtained from these studies on reduced spinels are comparable to the rates obtained on reduced perovskites. In a DFT study made by Bligaard et al. [137], the dissociative chemisorption of carbon dioxide was found to be more favorable on metallic iron than on metallic cobalt. Transition metals with lower energies for CO<sub>2</sub> dissociative chemisorption could lower the temperature for CO<sub>2</sub> conversion. However, it is not expected that the Fe perovskite phase will decompose to the base metal and metal oxides as Co-based materials did in the previous study on the RWGS-CL process. Incorporating Fe into the La<sub>0.75</sub>Sr<sub>0.25</sub>CoO<sub>3</sub> perovskite improves its crystalline structure stability under a reducing agent until ~850 °C [88, 149].

In addition to reactivity considerations that have been based on operation temperatures, product selectivity of the CO<sub>2</sub> conversion process may also prove significant. This is especially important as the work described above indicated C(s) may form when reacting CO<sub>2</sub> with Fe-containing oxide systems. The desired reaction pathway in the RWGS-CL process is described in reactions (2.1) and (2.2), first introduced in Chapter 2. In the first step, hydrogen is flowed and oxygen vacancies and water are formed. When CO<sub>2</sub> is flowed (second step), one O regenerates the perovskite to its initial fully oxidized state, while forming CO. This pathway intensifies our previous work because the first reaction (2.1) does not decompose the perovskite phase into its base and metallic oxides.



In addition to the desired pathway (reactions 2.1 and 2.2), a competing pathway (reaction 4.1) involving CO<sub>2</sub> decomposition to C(s) and O<sub>2</sub> may also be possible. In reaction (4.1), C(s)

could be deposited on the perovskite surface while O<sub>2</sub> could be oxidizing the oxygen deficient perovskite or leaving the system as gaseous O<sub>2</sub>.



In this study, the RWGS-CL has been intensified to work isothermally at 550 °C without phase change by incorporating Fe into the B site of the perovskite. Being a two-step process, the RWGS-CL avoids the need for additional set ups to further oxidize the oxygen carriers. The use of Fe-based perovskites allows for an isothermal RWGS-CL at a temperature 300 °C lower than the process developed on Co-based perovskites. Structure stability and CO production rates throughout five RWGS-CL cycles on an Fe-rich (La<sub>0.75</sub>Sr<sub>0.25</sub>Co<sub>(1-Y)</sub>Fe<sub>Y</sub>O<sub>3</sub>) perovskite were studied. CO production rates were found to be of the same order as our previous study. The enhanced structural stability caused by the incorporation of Fe in the perovskite is maintained throughout the reaction cycles. Furthermore, the selectivity of the process was determined as 300 times more favorable towards reaction 2.2 (CO) when compared to reaction 4.1 (C).

## 4.2 Experimental Procedure

### 4.2.1 Synthesis of Oxide Powders

A Pechini synthesis as described by Popa and Kakihana [97] was followed to synthesize the La<sub>0.75</sub>Sr<sub>0.25</sub>Co<sub>(1-Y)</sub>Fe<sub>Y</sub>O<sub>3</sub> powders. First, citric acid (Aldrich, ACS grade ≥99.5%) was dissolved in water at 60 °C while stirring. Then, the precursors La(NO<sub>3</sub>)<sub>3</sub> (Aldrich, 99.9%), SrCO<sub>3</sub> (Alfa Aesar, 99.994%), CoCO<sub>3</sub> (Aldrich, Co 43-47%) and Fe(NO<sub>3</sub>)<sub>3</sub> (Aldrich, 98+%) were added to the solution and were stirred at the same temperature for 2 h. Next, the solution temperature was raised to 90 °C and ethylene glycol (Aldrich, Reagent Plus ≥99%) was added. The solution was kept at this temperature for 7 h while stirring. The resulting resin was transferred to a crucible and was heated (at 25 °C/min) in a (Vulcan 3-550) furnace from room



temperature to 450 °C for 2 h. Upon cooling, the resulting powder was crushed and was heated at the same ramp rate, from room temperature to 950 °C for 6 h.

The molar ratios of the precursors used were (A site : B site : citric acid : ethylene glycol = 1:1:10:40) following the synthesis method of Ivanova et al. [78].

## 4.2.2 Characterization

**4.2.2.1 XRD.** A Bruker X-Ray Diffractometer was used to collect the diffraction patterns of the powders from 20 to 100 2 $\theta$ ° at room temperature. The X-ray source used was a Cu K $\alpha$  ( $\lambda$  = 0.154 nm) with a step size of 0.0102 2 $\theta$ ° and an average time per step of 1.2 s.

**4.2.2.2 BET Surface Area.** Surface areas were determined by the multi-point BET method using N<sub>2</sub> physisorption (at T = 77 K) performed in an Autosorb iQ Quantachrome Gas Sorption System. The samples were outgassed for 6 h at 180 °C prior to analysis.

## 4.2.3 Reaction Experiments

In each experiment, approximately 75 mg of powder was packed between high-temperature resistant glass wool in a quartz U-tube for each experiment. The U-tube was attached to a reactor system with connections to He, CO<sub>2</sub> and H<sub>2</sub>, (gas purities  $\geq$ 99.99%) regulated by Alicat mass flow controllers. The reaction products were monitored with a MKS Cirrus mass spectrometer (MS). For quantification of the CO<sub>2</sub>, H<sub>2</sub>O, H<sub>2</sub> and CO signals, the m/z ratios of 44, 18, 2 and 28 were monitored respectively. Ionization factors and fragmentation patterns of each species were analyzed and used in the quantifications. The quantification procedure is explained elsewhere in more detail [45].

The total gas flow rate was held constant at approximately 50 SCCM during H<sub>2</sub>/He and He flows and at 48.5 SCCM during the CO<sub>2</sub>/He flow. Prior to each experiment performed in the MS, the powders were treated in 20% O<sub>2</sub>/He from room temperature to 850 °C (ramp rate of 25

°C/min) and held for 20 min. Upon cooling under the same environment, the flow was changed to He until the monitored fragmentation patterns remained stable, before continuing with the experiments.

**4.2.3.1 Temperature-Programmed Reduction (TPR).** In 10% H<sub>2</sub>/He, the samples were heated to 850 °C at 10 °C/min and held at that temperature for at least 1h. The reductions were monitored by water formation via the m/z = 18 (H<sub>2</sub>O) signal.

**4.2.3.2 Temperature-Programmed Oxidation with CO<sub>2</sub> (TPO-CO<sub>2</sub>).** The samples were reduced in 10% H<sub>2</sub>/He at 550 °C for 30 min, after which, the samples were cooled to approximately 100 °C in He. Upon stabilization of the fragmentation patterns, 6.7% CO<sub>2</sub>/He was flowed to the samples for approximately 30 min, and then, the samples were heated to 850 °C (at 10 °C/min) and held at that temperature until the signals remained stable.

**4.2.3.3 Isothermal RWGS-CL.** Five RWGS-CL cycles at 550 °C were conducted on the La<sub>0.75</sub>Sr<sub>0.25</sub>FeO<sub>3</sub> sample. The sample was reduced under 10% H<sub>2</sub>/He for 20 min at 550 °C. This step was followed by a 20 min He flushing and a 6.7% CO<sub>2</sub>/He flow for 20 min. The system was flushed with He again for 20 min, and the cycle was repeated 4 more times. The first cycle of RWGS-CL was performed three times to determine the reproducibility of the results. H<sub>2</sub> and CO production were quantified as described previously.

**4.2.3.4 Carbon Deposit on La<sub>0.75</sub>Sr<sub>0.25</sub>FeO<sub>3</sub>.** The selectivity of the RWGS-CL process towards CO (reaction 2.2) and C(s) (reaction 4.1) was determined by quantifying the difference between two experiments, described below. In both experiments, the samples were pre-treated in O<sub>2</sub> as explained earlier, then, one cycle of RWGS-CL at 550 °C was performed. The environment was then changed to He and the sample was cooled to 100 °C.

In the first experiment, the environment was changed to 10% O<sub>2</sub>/He. Next, upon stabilization of the fragmentation patterns, the sample was heated up to 850 °C (at 10 °C/min) and the CO<sub>2</sub> produced was quantified similarly as to other species.

In the second experiment, the sample was heated up in He to 850 °C (at 10 °C/min) and the CO<sub>2</sub> desorbed was quantified as described before. The difference between the CO<sub>2</sub> produced (from experiment 1) and CO<sub>2</sub> desorbed (experiment 2) was taken as representative of the C(s) deposited during the RWGS-CL.

## 4.3 Results and Discussion

### 4.3.1 Surface Area, Bulk Structure, Reducibility, and Re-Oxidation Capabilities

The Y=0 sample exhibited a cubic structure (Figure 4.1), as reported before for La<sub>0.75</sub>Sr<sub>0.25</sub>CoO<sub>3</sub> synthesized by the Pechini method [45]. The diffraction pattern also showed the main diffraction line of Co<sub>3</sub>O<sub>4</sub> visible at 36.85° 2θ. The Y=0.5 sample was predominantly cubic (pink dotted lines), with orthorhombic diffraction lines visible (black dotted lines) and the main diffraction line of Co<sub>3</sub>O<sub>4</sub> visible at 36.77° 2θ. The presence of Co<sub>3</sub>O<sub>4</sub> in the Y= 0 and 0.5 samples could be a consequence of a B-site deficiency in the perovskite or caused by excess of cobalt precursor in the beginning of the synthesis. It is unclear if the orthorhombic diffraction lines are due a Fe-rich perovskite (with very high Fe/Co ratio) or the diffraction pattern of La<sub>0.75</sub>Sr<sub>0.25</sub>FeO<sub>3</sub>, which could be justified because some of the Co is already out of the structure as Co<sub>3</sub>O<sub>4</sub>.

The Y=0.75 and Y=1 samples exhibited an orthorhombic crystalline structure, consistent with other reports for La<sub>(1-x)</sub>Sr<sub>x</sub>FeO<sub>3</sub> perovskites rich in La [150-153] and contradicting other groups which have used different methods to synthesize La<sub>(1-x)</sub>Sr<sub>x</sub>FeO<sub>3</sub> and have obtained rhombohedral samples with an R3c symmetry [131]. The Y=0.75 sample also exhibited two

diffraction lines at  $30.34^\circ$  and  $35.75^\circ$   $2\theta$  corresponding to the most intense diffraction lines of cubic  $\text{Fe}_3\text{O}_4$ .

The lattice parameters and unit cell volume of the cubic samples increased with Fe content (as observed by others [151]) for both the predominantly cubic and predominantly orthorhombic samples (Table 3.1) due to the larger ionic radii of Fe [154]. The surface areas (Table 3.1) were lower than the surface areas obtained by our group previously [45] due to the synthesis conditions, which involved higher temperatures. As a consequence, the crystallinity of the samples increased using  $950^\circ\text{C}$ , when compared to previous samples synthesized at  $750^\circ\text{C}$ .

Two distinct reduction features are observed on the temperature-programmed reduction profiles of all the  $\text{La}_{0.75}\text{Sr}_{0.25}\text{Co}_{(1-Y)}\text{Fe}_{(Y)}\text{O}_3$  powders (Figure 4.2). The first (low-temperature) region corresponded to formation of oxygen vacancies in the structure of the material as a consequence of changes in the oxidation state of Co and Fe possibly changing from  $\text{Co}^{4+}$  to  $\text{Co}^{3+}$ ,  $\text{Co}^{3+}$  to  $\text{Co}^{2+}$  [78] and  $\text{Fe}^{4+}$  to  $\text{Fe}^{3+}$  [88] respectively. The second (high-temperature) region corresponded to the reduction of the oxygen-vacant perovskite into its base oxides [63, 78] and metal phases [155] for the Co-containing samples (with reduction proportional to their Co content), and predominantly oxygen vacancies formation on the Fe-rich perovskites [88], although  $\text{Fe}^0$  has been detected by XRD on  $Y=0.8$  samples after reduction under  $\text{H}_2$  at  $800^\circ\text{C}$  [151]. The TPR profiles showed that as the Fe:Co ratio increases, the two reduction regions shifted to higher temperatures and the TPR profiles decreased in intensity. The improved stability is in agreement with literature. Natile et al. found that perovskites containing Fe on the B site maintained a predominant perovskite structure even after reduction at  $600^\circ\text{C}$  for 30 min under  $\text{H}_2$  [151]. For the sample with  $Y=1$ , the reduction happens in one step, at temperatures

higher than 700 °C [155]. (La,Sr)(Co,Fe)O<sub>3</sub> perovskites typically reduce at higher temperatures as the Fe content increases [88].

As the Fe content increased, the amount of water produced during the reduction step prior to the TPO-CO<sub>2</sub> (T=550°C, data not shown), decreased from 1.09 mol H<sub>2</sub>O/ mol perovskite for Y=0, to 0.71 and 0.72 mol H<sub>2</sub>O/ mol perovskite for Y=0.5 and Y=0.75 respectively to 0.43 mol H<sub>2</sub>O/ mol perovskite for Y=1. An analysis of these numbers reveals that the oxygen removed from the Y=0 was at least 1.6 times higher than the rest of the samples. Therefore, it is likely that the Y=0 sample has been reduced to its base oxides and metals, consistent with the previous study [45]. The mixed Fe and Co perovskite samples may also undergo a reductive phase change to its base oxides and metals. However, as discussed later, XRD was conducted for the Fe sample (Y=1) after reduction and the stability of the perovskite phase was verified. The consequences of the degree of the reduction of the perovskites on CO formation will be discussed later.

The samples containing Fe (Y=0.5, 0.75, 1) have a higher structure stability than the Y=0 sample. The similarity in the reduction of the Y=0.5 and 0.75 samples was also evident from their reduction profiles (Figure 4.2), which are nearly identical and in between Y=0 and Y=1 samples. It is important to state that a portion of the H<sub>2</sub>O produced could be due to the reaction between H<sub>2</sub> and the O<sub>2</sub> adsorbed in the perovskite surface during the high-temperature O<sub>2</sub> treatment.

Carbon monoxide formation from CO<sub>2</sub> as a function of temperature on the reduced powders (Figure 4.3) exhibited different behavior when the samples containing Fe (Y=0.5, 0.75, 1) are compared to that without (Y=0). As the Fe content (Y) increased, the amount of CO produced during the CO<sub>2</sub>-conversion step decreased from 0.66 mol CO/ mol perovskite for Y=0,

to 0.19 mol CO/ mol perovskite for  $Y=0.5$ , 0.17 mol CO/ mol perovskite for  $Y=0.75$  and 0.12 mol CO/ mol perovskite for  $Y=1$ . The decreased production of CO as  $Y$  increased was directly related to the degree of reduction of each perovskite during the 30 min  $H_2$ -reduction step previous to the  $CO_2$ -conversion step (described above). Higher degrees of reduction caused the perovskite to partially or completely change crystalline phases. The production of CO was higher on the  $Y=0$  sample due to its higher degree of reduction, which caused it to change crystalline phases to Co stabilized on a  $La_2O_3$  support [45]. During the reduction of the  $Y=0.5$  sample, a smaller fraction of the crystalline perovskite could be reduced to base oxides and metals due to the higher structure stability induced by the partial substitution of Fe on the B site. XRD (not shown) was performed on the  $Y=0.5$  sample after reduction and no evidence of metallic cobalt was observed. However, metallic cobalt could still be present as others have seen in magnetization studies when it has been undetected by XRD [155], which is more sensitive to larger crystallites.

In the case that the  $Y=0.5$  and  $0.75$  samples also underwent reduction to base oxides and metallic Co and Fe, as in the case of the  $Y=0$  sample, it would make sense that increasing the amount of Fe on the B site would decrease the CO production onset temperature, because  $CO_2$  activation is presumed to be a key step on the conversion of  $CO_2$  to CO, and  $CO_2$  dissociative chemisorption is preferred on Fe than on Co single crystals [137]. Furthermore, other studies have determined that reaction rates for the RWGS reaction are faster on Fe than Co [156, 157]. The  $Y=0.75$  perovskite exhibited a different CO-production pattern with two evident peaks in the range of 500 to 750 °C possibly due to a phase change or phase segregation on the material upon its re-oxidation with  $CO_2$ . Due to its increased stability, the  $Y=1$  sample was the least likely to undergo crystalline phase changes during the  $H_2$ -reduction step. Presumably, less energy is

required to re-oxidize the oxygen vacant structure (reaction II) as opposed to re-oxidizing reduced phases (metallic Co, and reduced layered perovskites) as has been seen before in Co-based perovskites [45], as a consequence, the CO production onset temperature is  $\sim 200$  °C lower than in the Y=0, 0.5 samples and  $\sim 50$  °C lower than in the Y=0.75 sample.

#### 4.3.2 Isothermal RWGS-CL Using $\text{La}_{0.75}\text{Sr}_{0.25}\text{FeO}_3$

**4.3.2.1 Reaction Rates and Changes in Oxygen Stoichiometry.** The sample with Y=1 was able to produce CO at the lowest peak temperature (550 °C, Figure 4.3), which constituted a decrease of 300 °C with respect to our previous results [45] and of at least 250 °C with respect to other similar processes that without  $\text{H}_2$  use, also achieve conversion of  $\text{CO}_2$  on the oxygen vacancies of metal oxides [109, 111-114]. Five cycles of isothermal RWGS-CL were studied on the Y=1 sample, to evaluate the structure stability, CO yield and selectivity. Figure 4.4 shows the normalized flows of  $\text{H}_2$  and  $\text{CO}_2$  and the  $\text{H}_2\text{O}$  and CO produced on every reaction cycle. The areas representing the production of  $\text{H}_2\text{O}$  were larger than the area of CO produced, which suggested that more oxygen vacancies were formed during the reduction than filled during the  $\text{CO}_2$  conversion step.

Quantification of  $\text{H}_2\text{O}$  and CO production is presented in Figure 4.5 (primary vertical axis). The CO or  $\text{H}_2\text{O}$  amount term is defined as the moles of CO or  $\text{H}_2\text{O}$  formed per each mole of perovskite. The  $\text{H}_2\text{O}$  amount is representative of the formation of oxygen vacancies ( $\delta$ , reaction 2.1) and the CO amount describes the re-oxidation of the oxygen vacancies on the perovskite (reaction 2.2). For the first cycle, the  $\text{H}_2\text{O}$  amount is almost twice as much (41 mol  $\text{H}_2\text{O}$ / mol perovskite) as for the rest of the cycles. Starting from cycle two, it remains constant at  $\sim 28$  mol  $\text{H}_2\text{O}$ / mol perovskite. The difference from the first cycle to the rest was presumed to be caused by oxygen adsorbed in the surface of the perovskite during the high-temperature  $\text{O}_2$

treatment. Possibly,  $\sim 0.065$  mol  $O_2$ / mol perovskite could have been adsorbed in the perovskite surface, which could react with  $H_2$  forming  $\sim 0.13$  mol  $H_2O$ / mol perovskite during the reduction on the first cycle. This  $O_2$  adsorbed ( $0.065$  mol  $O_2$ / mol perovskite) is equivalent to 6% of an  $O_2$  monolayer on the perovskite surface. With this assumption, the  $\delta$  formed during each cycle can be considered as constant, demonstrating that  $\delta$  on the  $Y=1$  sample was strongly dependent on the reduction time. Also, it is important to note that the  $H_2O$  amount term remained always below  $0.5$  mol  $H_2O$ / mol perovskite, suggesting that the perovskite remained in its original crystalline structure.

The CO formation rates for each RWGS-CL cycle (secondary vertical axis) from our current and previous study are also shown in Figure 4.5. In the current study, the CO production rates increased in the first cycles and remained roughly constant after the second cycle. The rates of CO formation for the third, fourth and fifth cycle are  $69.57$ ,  $77.15$  and  $73.09$   $\mu\text{mol CO /grams of Perovskite/ min}$  respectively, and the deviation was determined as  $4$   $\mu\text{mol CO /grams of Perovskite/ min}$ . In comparison to our previous study, CO formation rates (after stabilization on the second cycle) when Co was reduced in the  $La_{0.75}Sr_{0.25}CoO_3$  were only  $\sim 5\%$  higher than with the  $La_{0.75}Sr_{0.25}FeO_3$  (after stabilization on the third cycle) even though the temperature was  $300^\circ\text{C}$  higher in the case of Co [45]. Additionally, upon the  $H_2$ -reduction step, more Co is available than oxygen vacancies on the  $La_{0.75}Sr_{0.25}FeO_3$  surface, as can be interpreted by evaluating the calculations of mol  $H_2O$ / mol perovskite in section 4.3.1. These results indicated that the reactivity of the Fe-based samples with  $CO_2$  is higher than with the Co-based samples.

**4.3.2.2 Role of Oxygen Vacancies on  $CO_2$  Adsorption.** For each cycle, the amount of  $H_2O$  produced was higher than the amount of CO produced. The CO production increased with cycle number until it stabilized at the third cycle. A detailed analysis of the oxygen stoichiometry



changes that the perovskite undergoes throughout the cycles is presented in Figure 4.6. Different arguments have been proposed on the oxygen stoichiometry of the Fe-rich  $\text{La}_{1-x}\text{Sr}_x(\text{Co,Fe})\text{O}_3$  system. A previous study [88] concluded that  $\text{La}_{0.6}\text{Sr}_{0.4}\text{Co}_{Y-1}\text{Fe}_Y\text{O}_3$  was stoichiometric (for  $Y=0.9, 0.8, 0.7$ ), whereas Tai et al. [158] measured the  $\text{La}_{1-x}\text{Sr}_x\text{Co}_{0.2}\text{Fe}_{0.8}\text{O}_3$  close to stoichiometric at  $X=0.4$  and that the stoichiometry increases with La content. Therefore, in our calculations, we have assumed that the perovskite is initially stoichiometric ( $\delta=0$ ) with respect to its oxygen content. The  $3-\delta$  amounts represent the extent of the oxygen non-stoichiometry of the perovskite at the end of either the  $\text{H}_2$ -reduction, where the oxygen vacancies are created (diagonal blue stripes) or at the end of the  $\text{CO}_2$ -conversion step, where the oxygen vacancies are refilled (red bars). In the first  $3-\delta$  value presented, even though the  $\text{H}_2\text{O}$  amount calculated was 0.41 mol  $\text{H}_2\text{O}$ / mol perovskite only  $\delta = 0.28$  is considered as the amount of oxygen vacancies produced.

The oxygen stoichiometry of the perovskite did not return to its originally oxidized state after each cycle (Figure 4.6). This indicated that the oxygen vacancies formed during each reduction step are not completely re-filled in the following  $\text{CO}_2$  conversion step. In other words, the accumulated oxygen deficiency on the perovskite increases on each cycle, because during each reduction step the same amount of oxygen is removed ( $\sim 0.28$  mol O /mol perovskite) but a smaller amount of vacancies are re-filled by  $\text{CO}_2$ . It is expected, due to the high structural stability of the Fe-based perovskites, that this discrepancy would eventually be negligible, and the exchanged oxygen and the rates would be consistent for further cycles. The presence of oxygen vacancies on the surface was hypothesized to help in a more rapid  $\text{CO}_2$  reaction process, which is supported by increasing  $\text{CO}_2$  adsorption strength with increasing vacancies. A computational collaborator studied the effect of the extent of oxygen vacancies ( $\delta$ ) on the

adsorption strength of CO<sub>2</sub> on the La<sub>0.75</sub>Sr<sub>0.25</sub>FeO<sub>3</sub> perovskite surface. It was found that the adsorption strength increases with increasing oxygen vacancies. The experimental and computational results suggest that the driving force to break the CO-O bond increases with  $\delta$ , resulting in more CO produced.

**4.3.2.3 Crystalline Structure Stability.** XRD of the Y=1 perovskite throughout the RWGS-CL cycles (Figure 4.7) showed that the structure remains stable as a single-phase orthorhombic powder. The intensity of the diffraction lines decreased after the first reduction possibly due to a decreased crystallinity as a consequence of the H<sub>2</sub>-treatment. Also, the diffraction lines of the sample shifted towards higher  $2\theta$  angles, causing a contraction in the lattice parameters and a decrease in the cell volume (Table 3.2). Upon re-oxidation with CO<sub>2</sub>, the intensity of the diffraction lines increased to nearly the same intensity as the fresh sample and shift back towards lower  $2\theta$  angles. These results indicated that the perovskite returned to nearly its original crystalline structure at the end of the cycles. This suggests that the RWGS-CL on the Y=1 sample could be recyclable beyond the 5 cycles tested here. The crystallite size was determined by the Scherrer equation using  $K=1$ . After the first reduction, the perovskite increases its crystallite size by 10%, and at the end of the last cycle, it displays another 10% increment, showing that after five RWGS-CL cycles, the sample has only incremented its crystallite size by ~20%.

**4.3.2.4 Selectivity Towards CO.** To determine the selectivity of the Y=1 sample in the RWGS-CL process towards reaction (2.2) as opposed to reaction (4.1), the combustion of the deposited C(s) was quantified as  $4.47e^{-3}$  mol CO<sub>2</sub> /mol perovskite, then, the CO<sub>2</sub> desorbed after the first conversion cycle was determined to be  $5.74e^{-4}$  mol CO<sub>2</sub> /mol perovskite. The  $3.89e^{-3}$  mol CO<sub>2</sub> /mol perovskite difference between the two experiments represents the CO<sub>2</sub> formed only

due to deposited C(s) combusting with O<sub>2</sub>. This number is two orders of magnitude lower than the moles of CO produced per moles of Perovskite during the first cycle of RWGS-CL. The selectivity of the process towards reaction (2.2) was calculated using the average 0.12 mol CO<sub>2</sub> /mol perovskite produced in the first cycle of the RWGS-CL (Figure 4.5) divided by the 3.89e<sup>-3</sup> mol CO<sub>2</sub> /mol perovskite combusted from the deposited C(s). The process is 30.9 times more selective towards reaction (2.2) than towards reaction (4.1). This represents an advantage over CO<sub>2</sub> conversion on Fe-based spinels, in which selectivity towards CO was found to be between 1 and 1.8 [52].

#### 4.4 Summary

Four Sr- and Fe- doped LaCoO<sub>3</sub> (La<sub>0.75</sub>Sr<sub>0.25</sub>Co<sub>1-Y</sub>Fe<sub>Y</sub>O<sub>3-δ</sub> with Y = 0, 0.50, 0.75, and 1) were synthesized and studied for their properties for possible use in the RWGS-CL process that converts CO<sub>2</sub> to CO. Temperature-programmed experiments determined that the Y=1 sample had the ability to convert CO<sub>2</sub> to CO at the lowest temperature (550 °C). Also, at this temperature, the H<sub>2</sub>-reduction of the sample does not decompose the perovskite into base and metal oxides. The RWGS-CL was tested for five cycles on the La<sub>0.75</sub>Sr<sub>0.25</sub>FeO<sub>3</sub> isothermally at 550 °C, which represents a ~300 °C decrease in the CO<sub>2</sub> conversion to CO when compared to our previous studies and similar processes. Upon quantification of the H<sub>2</sub>O and CO amounts produced on each cycle and analysis of DFT-calculated CO<sub>2</sub> adsorption energies as a function of oxygen vacancies (not shown here), it was concluded that δ in the perovskite is the driving force to break the CO-O bond and re-oxidizing the La<sub>0.75</sub>Sr<sub>0.25</sub>FeO<sub>3-δ</sub> sample. Post-reaction XRD studies showed that the sample retains its orthorhombic structure throughout the cycles. The conversion of CO<sub>2</sub> to CO was found to be two orders of magnitudes higher than its decomposition to C and O<sub>2</sub>, therefore, it was concluded that the decomposition of CO<sub>2</sub> on the perovskite surface is negligible. The low

conversion temperature of CO<sub>2</sub> while achieving competitive CO production rates and the temperature integration of the process, make for the RWGS-CL process a plausible technology for the formation of C1 feeds, if a renewable hydrogen source is used.

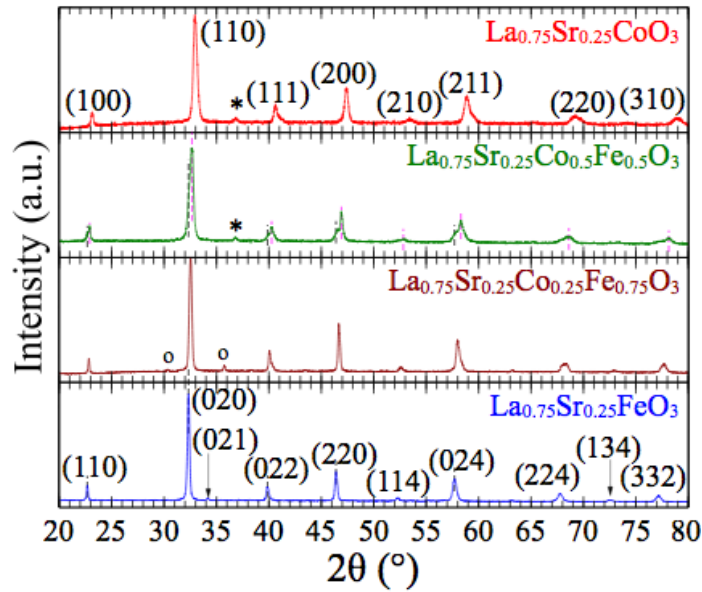


Figure 4.1 X-ray diffraction patterns of the  $\text{La}_{0.75}\text{Sr}_{0.25}\text{Co}_{(1-Y)}\text{Fe}_{(Y)}\text{O}_3$  powders. The  $Y=0$  and  $Y=0.5$  samples possessed a predominantly cubic structure with traces of  $\text{Co}_3\text{O}_4$  (\*) (Reference 03-065-3103). The  $Y=0.5$  sample also exhibited a mixture of cubic (dotted pink) and rhombohedral (dotted black) diffraction lines. The  $Y=0.75$  sample had a phase mixture of orthorhombic perovskite and  $\text{Fe}_3\text{O}_4$  (o) (Reference 00-019-0629). The  $Y=1$  sample had a single-phase orthorhombic structure.

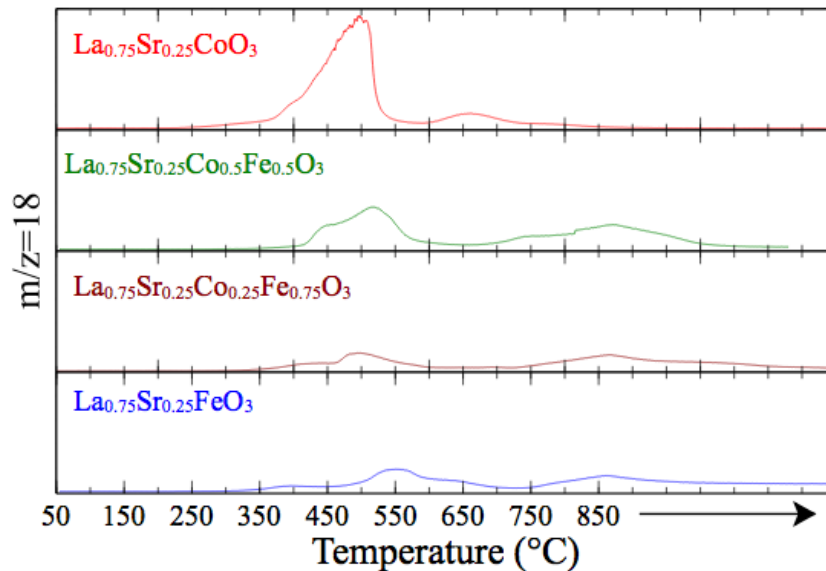


Figure 4.2 Temperature-programmed reduction of  $\text{La}_{0.75}\text{Sr}_{0.25}\text{Co}_{(1-Y)}\text{Fe}_{(Y)}\text{O}_3$  by 10%  $\text{H}_2/\text{He}$ . The profiles are normalized with respect to the  $\text{La}_{0.75}\text{Sr}_{0.25}\text{CoO}_3$  ( $Y=0$ ) sample.

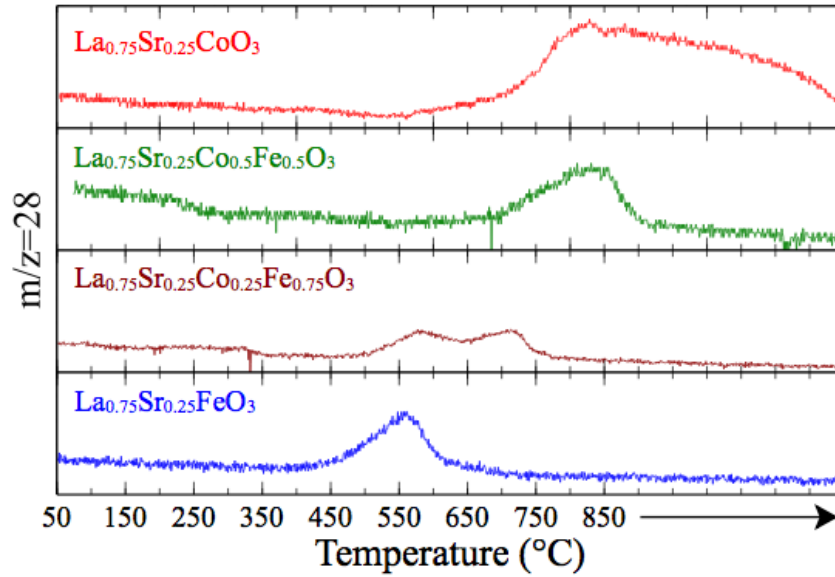


Figure 4.3 Temperature-programmed oxidation of  $\text{La}_{0.75}\text{Sr}_{0.25}\text{Co}_{(1-Y)}\text{Fe}_{(Y)}\text{O}_3$  under 6.7%  $\text{CO}_2/\text{He}$  after an isothermal reduction at 550 °C for 30 min by 10%  $\text{H}_2/\text{He}$ . The profiles are normalized with respect to the  $\text{La}_{0.75}\text{Sr}_{0.25}\text{CoO}_3$  ( $Y=0$ ) sample.

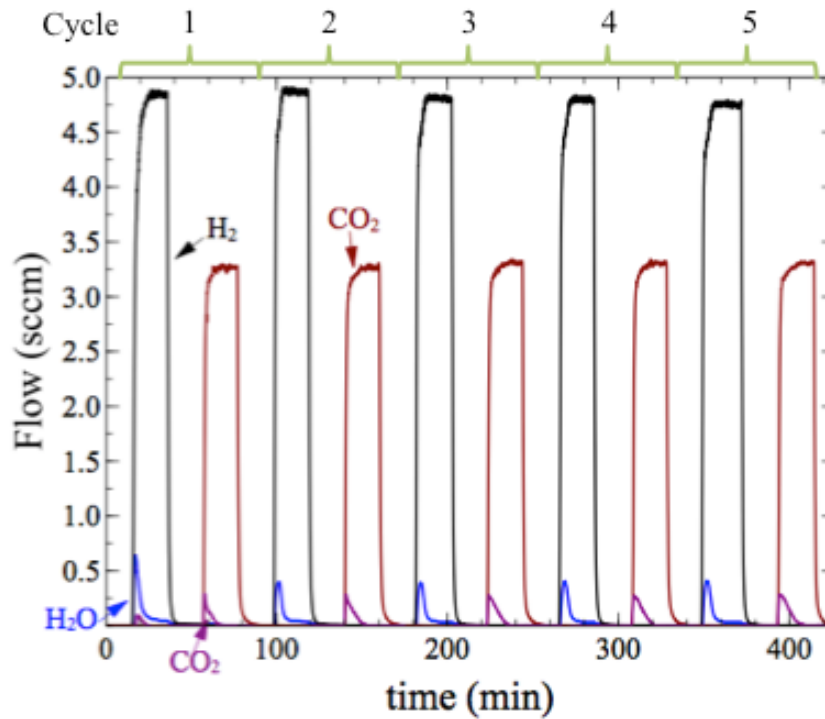


Figure 4.4 Five cycles of RWGS-CL on 76.1mg of  $\text{La}_{0.75}\text{Sr}_{0.25}\text{FeO}_3$  at 550 °C. Time on stream of  $\text{H}_2$  and  $\text{CO}_2$  flow and  $\text{H}_2\text{O}$  and  $\text{CO}$  production.

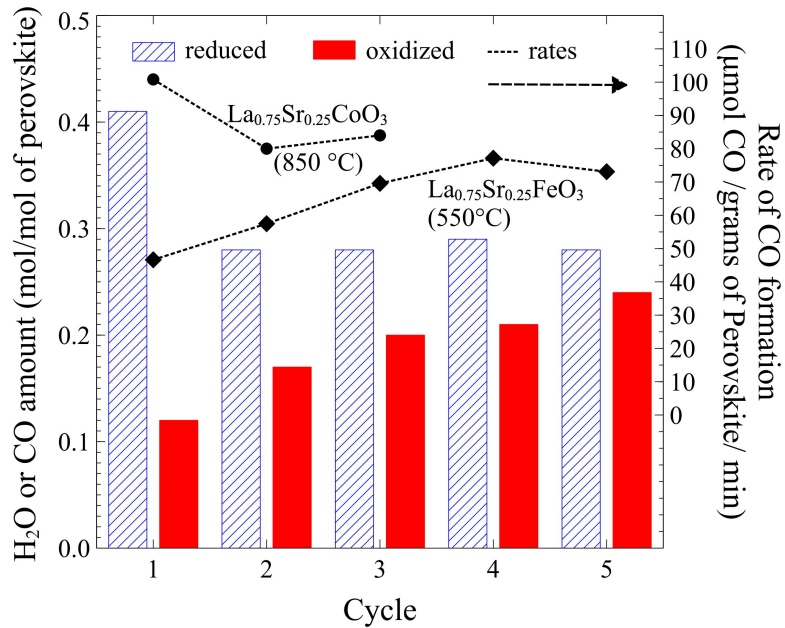


Figure 4.5 RWGS-CL on  $\text{La}_{0.75}\text{Sr}_{0.25}\text{FeO}_3$  at 550 °C. The molar ratios of  $\text{H}_2\text{O}$  and CO generated in each cycle (left axis) and CO production rates (right axis) are showed. The blue bars (diagonal stripes) represent the amount of  $\text{H}_2\text{O}$  formed (mol  $\text{H}_2\text{O}$ /mol perovskite) on each reduction step under 10%  $\text{H}_2/\text{He}$  for 20 min. The red bars (solid) represent the amount of CO formed on each oxidation step (under 6.7%  $\text{CO}_2/\text{He}$ ). CO production rates from this study ( $\text{La}_{0.75}\text{Sr}_{0.25}\text{FeO}_3$  at 550 °C, diamond markers) are compared to the rates from our previous study ( $\text{La}_{0.75}\text{Sr}_{0.25}\text{CoO}_3$  at 850 °C [45], circle markers) on the secondary y-axis. The first oxidation in the cycle experiment was performed three times and the rate standard deviation was 4  $\mu\text{mol CO / grams of perovskite / min}$ .

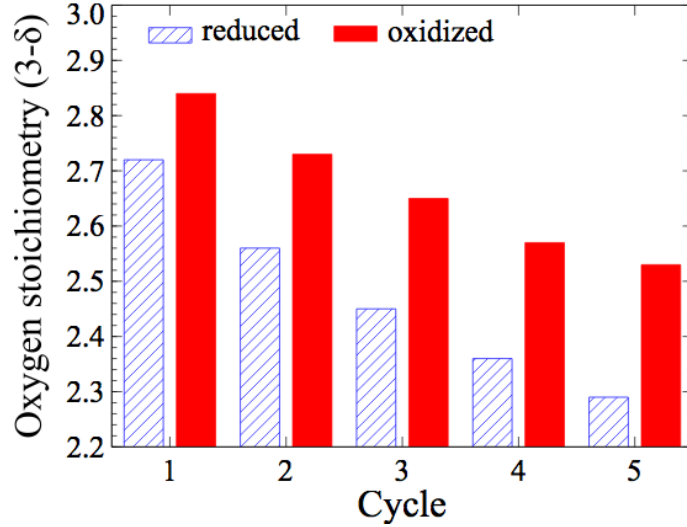


Figure 4.6 Oxygen stoichiometry variations on the  $\text{La}_{0.75}\text{Sr}_{0.25}\text{FeO}_3$  during the RWGS-CL at 550 °C. The sample was taken as fully oxidized ( $\delta=0$ ) initially. The bars represent the oxygen stoichiometry ( $3-\delta$ ) of the sample after each reduction step (blue horizontal stripes) and conversion step (solid red).

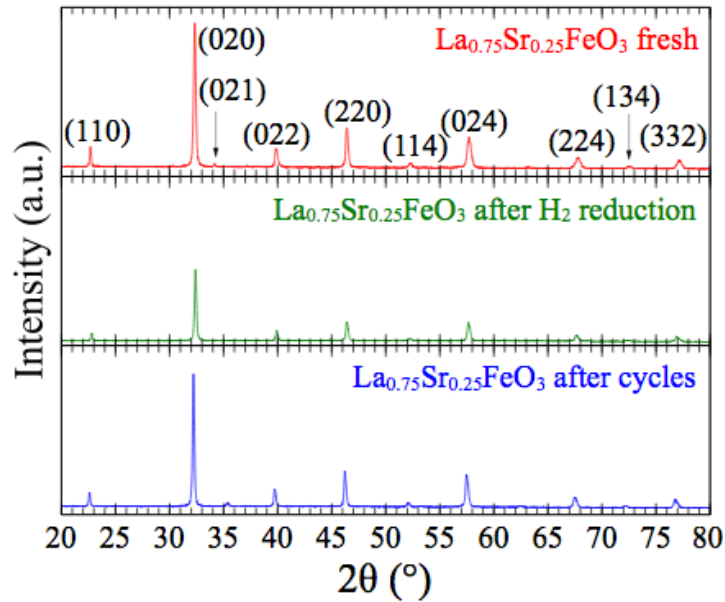


Figure 4.7 X-ray diffraction patterns of the  $\text{La}_{0.75}\text{Sr}_{0.25}\text{FeO}_3$  powder throughout the RWGS-CL cycles. The powder exhibits a single-phase orthorhombic crystalline structure when it is fresh, after the first  $\text{H}_2$ -reduction and at the end of the fifth cycle. The patterns are normalized with respect to the fresh sample.



Table 4.1 Surface area and crystallographic parameters of  $\text{La}_{0.75}\text{Sr}_{0.25}\text{Co}_{(1-Y)}\text{Fe}_Y\text{O}_3$ .

Y	Position of main diffraction line ( $2\theta$ )	Lattice parameters ( $\text{\AA}$ )			Unit cell volume ( $\text{\AA}^3$ )	BET surface area ( $\text{m}^2/\text{g}$ )
		a	b	c		
0	(110) 32.96	3.84	--	--	56.81	1.32
0.5	(110) 32.58*	3.87	--	--	57.91	0.54
0.75	(020) 32.54	5.47	5.50	7.78	233.72	0.59
1	(020) 32.21	5.53	5.55	7.84	240.62	0.41

\* Lattice parameters and Miller indices calculated from the cubic diffraction lines.

Table 4.2 Lattice parameters changes of the  $\text{La}_{0.75}\text{Sr}_{0.25}\text{FeO}_3$  sample throughout the RWGS-CL cycles.

Sample	Position of (020) diffraction line ( $2\theta$ )	Lattice parameters ( $\text{\AA}$ )			Unit cell volume ( $\text{\AA}^3$ )	Crystallite size ( $\text{\AA}$ )
		a	b	c		
Fresh	32.33	5.53	5.53	7.80	238.53	395.8
After 1 <sup>st</sup> $\text{H}_2$ -reduction	32.40	5.48	5.55	7.82	237.71	436.7
After 5 cycles	32.21	5.53	5.55	7.84	240.64	481.8

## CHAPTER 5: MORE CU, MORE PROBLEMS: DECREASED CO<sub>2</sub> CONVERSION ABILITY BY CU-DOPED LA<sub>0.75</sub>SR<sub>0.25</sub>FeO<sub>3</sub> PEROVSKITE OXIDES<sup>4</sup>

### 5.1 Introduction

In 2013, the atmospheric concentration of carbon dioxide reached 400 ppm [159], and emissions are expected to increase at least 20% by 2030 [160]. The world dependency on fossil fuels is steadily leading to their depletion while consumption trends are bound to increase, particularly because the development of technologies that can produce green fuels is still ongoing. An alternative to ensure a continuous supply of liquid fuels is to close a synthetic carbon cycle by transforming the highly available carbon dioxide to fuels.

The most popular technology for CO<sub>2</sub> mitigation is Carbon capture and storage (CCS). With around 14 operational plants worldwide, the projected capacity for the large scale processes is 0.106 Gt per year [161]. The main drawback of this process is the availability of sequestration sites, which are also a source of concern due to potential leakage [162-164]. Carbon capture and utilization (CCU) is an alternative to simultaneously decrease CO<sub>2</sub> emissions and ensure a continuous supply of carbon-based products including liquid fuels and chemicals [48, 165], while avoiding the drawbacks of CCS. But, with such an excessive amount of CO<sub>2</sub> available, only strategies that achieve high-volume products such as fuels would potentially impact CO<sub>2</sub> emissions noticeably. For example, use of CO<sub>2</sub> for methanol production would decrease CO<sub>2</sub> emissions by 0.26% at most, even though methanol is among the top ten commodity chemicals

---

<sup>4</sup> Reprinted with permission from Y. A. Daza, D. Maiti, B. J. Hare, V. R. Bhethanabotla, and J. N. Kuhn. More Cu, more problems: Decreased CO<sub>2</sub> conversion ability by Cu-doped La<sub>0.75</sub>Sr<sub>0.25</sub>FeO<sub>3</sub> perovskite oxides. *Surface Science*. In press. Copyright © 2015 Elsevier

produced [10]. The challenge is that CO<sub>2</sub> conversion requires hydrogen atoms, which directly or indirectly comes from water or methane. Since, as an example, methane steam reforming produces at least 9 t of CO<sub>2</sub> per t of H<sub>2</sub> produced [166], implementation of carbon-free hydrogen sources is required to impact CO<sub>2</sub> emission amounts. As a result, the cost of renewable hydrogen is key economic parameter in many CO<sub>2</sub> conversion processes [139].

The most energy efficient way to convert CO<sub>2</sub> using solar-assisted processes is reducing it to CO for liquid fuels synthesis [42]. Previously, we developed the Reverse Water Gas Shift Chemical Looping (RWGS-CL) process for the conversion of CO<sub>2</sub> to CO using mixed metal oxides as the redox material. Being a looping cycle process, the RWGS-CL inherently separates the reaction products (CO and H<sub>2</sub>O), decreasing potential deactivation of the material and the possibility of side reactions [45, 46]. Additionally, because the reactions taking place are stoichiometric, excess H<sub>2</sub> is not required. In the first step of the process, a stream of hydrogen reduces the metal oxides. In the second step, CO<sub>2</sub> is flowed to the reactor where it is converted to CO while one O atom is incorporated into the metal oxide structure. Perovskites oxides (ABO<sub>3</sub>) have been the material of focus due to their ability to accommodate oxygen vacancies in their structures. Oxygen vacancy formation depends on gas environment, temperature, and the metals on the A and B site of the oxide material [56, 58, 149, 167].

Previously, we used cobalt in the B site of the perovskites because it facilitates the generation of oxygen vacancies [56, 85] and stabilized metallic Co nanoparticles from the perovskite's decomposition were re-oxidized by CO<sub>2</sub> and CO was produced [45]. But, perovskite membranes with Co have proven unstable under demanding conditions [168-171], and particularly, Co-containing membranes suffer degradation due to contact with CO<sub>2</sub> [172]. To improve stability [88, 149], Fe was incorporated onto the B site which allowed for the two steps

of the RWGS-CL process to be isothermal at 550 °C [46]. Other groups have also used Fe-based materials to achieve CO<sub>2</sub> conversion in a Chemical Looping process with H<sub>2</sub> as a demonstration fuel, but the reduction and conversion temperatures used were at least 700 °C [48, 50]. In addition to stability imparted by Fe, the CO<sub>2</sub> conversion process may have also been improved by the increased CO<sub>2</sub> chemisorption energies on Fe surfaces [137, 173]. Even though an isothermal process is an important achievement for requiring lower energy consumption, a decrease in the process temperature to the ranges of Fischer-Tropsch (220 to 350 °C [174]) and methanol synthesis (210 - 260 °C [7, 115]) is desired.

In the present study, the doping of Cu onto the B site of Fe-based perovskite oxides is evaluated. Incorporation of small amounts of Cu into a La<sub>0.6</sub>Sr<sub>0.8</sub>(Fe,Co)O<sub>3</sub> perovskite, has shown increased oxygen vacancy formation when compared to un-doped materials [167]. Also, copper surfaces and stabilized copper nanoparticles have been studied for their CO<sub>2</sub> conversion properties in electrochemistry and photocatalysis [175-178]. Moreover, in methanol dehydrogenation reactions, CO production has been observed as low as 200–260°C in Cu-doped perovskites [179] and high CO formation has been achieved from CO<sub>2</sub> hydrogenation on Cu oxides supported on zinc, aluminum or silicon oxides [141, 180, 181]. An added advantage of incorporating Cu on the B site of the perovskite is related to its availability. There is approximately 100 times more Cu than Co in the world [182, 183], which is necessary to guarantee the continuous conversion of CO<sub>2</sub> and ability to replace the perovskite material when needed.

La<sub>0.75</sub>Sr<sub>0.25</sub>Fe<sub>1-Y</sub>Cu<sub>Y</sub>O<sub>3</sub> perovskites, (Cu100\*Y, with Y=0, 0.10, 0.25, 0.50, 0.75 and 1) were synthesized and characterized. Select reduced materials were then tested for their CO<sub>2</sub> conversion capabilities. Incorporation of Cu into the B site of the La<sub>0.75</sub>Sr<sub>0.25</sub>FeO<sub>3</sub> perovskite

inhibited the conversion of CO<sub>2</sub> when Cu is in high proportions. However, when Cu is doped in small amounts, CO formation occurred with a similar onset temperature as the Fe perovskite, which indicated negligible catalytic effect of the Cu doping. Moreover, the Cu doping decreased the total amount of CO formed and the stability of the perovskite. Complementary computational studies determined the oxygen vacancy formation energies as a consequence of A and B site composition and oxygen vacancy extent ( $\delta$ ) and correlated to experimental reducibility trends.

## 5.2 Materials and Methods

### 5.2.1 Synthesis of Oxide Powders

The Pechini method [97] was used to synthesize six perovskites: La<sub>0.75</sub>Sr<sub>0.25</sub>Fe<sub>1-Y</sub>Cu<sub>Y</sub>O<sub>3</sub> where Y = 0, 0.1, 0.25, 0.5, 0.75, 1.0. Citric acid (Aldrich >99.5%) was dissolved in deionized water to approximately a 2 M aqueous solution. La(NO<sub>3</sub>)<sub>3</sub> (Aldrich 99.9%), SrCO<sub>3</sub> (Aesar 99.994%), Fe(NO<sub>3</sub>)<sub>3</sub> (Aldrich ACS, grade 98+%), Cu(NO<sub>3</sub>)<sub>2</sub> (Aesar, 98%) were dissolved into the citric acid (CA) solution followed by a 2 h stirring period at 60 °C to ensure a homogenous mix. Ethylene glycol (Aldrich, >99%) was then added to initiate polyesterification and the mixture was stirred 7 h at 90 °C to decrease water content and form a viscous sol-gel. All reagents were measured to satisfy an La:Sr:B:Citric Acid:Ethylene Glycol mole ratio of 0.75:0.25:1:10:40 [78] with the corresponding Cu:Fe ratios varying to achieve each desired composition. Lanthanum nitrate and cobalt carbonate were 6 and 4% hydrated, respectively.

The gel was transferred into an alumina crucible and charred in air at 450 °C (at 25 °C/min) in a Vulcan 3-550 furnace for 2 h to evaporate any remaining water and produce an amorphous powder. The resulting powder was crushed and calcined in air at 950 °C (at 25 °C/min) for 6 h. The perovskites were labeled Cu0-100 with respect to their copper content.

### 5.2.2 XRD

Diffraction patterns were collected at room temperature in a Bruker X-Ray Diffractometer with Cu K $\alpha$  ( $\lambda = 0.154$  nm) from 20 to 100 2 $\theta^\circ$ . A step size of 0.0102 2 $\theta^\circ$  was used with 1.2 s per step.

### 5.2.3 Reaction Experiments

Approximately 75 mg of perovskite packed between glass wool in an U-tube quartz reactor were used in each experiment. All experiments were performed under a constant total flow rate of 50 sccm and a heating rate of 10  $^\circ\text{C}/\text{min}$  unless otherwise stated. All gases were purchased from Airgas in ultra-high purity (UHP) grade. The experiments were monitored by an MKS Cirrus mass spectrometer (MS). The reactor system used and species quantification methods were previously described [45, 46].

**5.2.3.1 Temperature-Programmed Oxygen Vacancy Formation.** Upon the stabilization of the signals in the MS, the samples were heated to 950  $^\circ\text{C}$  in He. The temperature was maintained until stabilization of the signals. The generation of oxygen vacancies was monitored via the  $m/z = 32$  ( $\text{O}_2$ ) signal.

**5.2.3.2 Temperature-Programmed Reduction (TPR).** Upon the stabilization of the signals in the MS, the environment was changed from He to 10%  $\text{H}_2/\text{He}$ . Again, after stabilization of the signals, the samples were heated to 950  $^\circ\text{C}$ . The heating was maintained at this temperature until the signals remained stable. Water formation was monitored via the  $m/z = 18$  ( $\text{H}_2\text{O}$ ) signal.

**5.2.3.3 Temperature-Programmed Oxidation with  $\text{CO}_2$  (TPO- $\text{CO}_2$ ).** Upon reduction at 450  $^\circ\text{C}$  for 30 min under 10%  $\text{H}_2/\text{He}$ , the samples were cooled under He to  $<100$   $^\circ\text{C}$ . After stabilization of the signals, 10%  $\text{CO}_2/\text{He}$  was flowed to the samples for at least 15 min (or until

the signals remained stable). Next, the samples were heated to 950 °C and the temperature was held until the MS signals remained stable.

### 5.3 Results

Thermodynamic properties of oxygen vacant metal oxides depend on the constituent metals and extent of oxygen vacancies ( $\delta$ ) formed during the reduction period [93]. Therefore, multiple studies have chosen oxygen vacancy formation energies, amongst others, as descriptors to predict the feasibility and potential efficiency of H<sub>2</sub>O and CO<sub>2</sub> thermochemical splitting to H<sub>2</sub> and CO respectively, on different metal oxides [92, 93, 184].

Deml et al. [184, 185] claim the existence of an ideal range of oxygen vacancy formation energies for which perovskites are thermodynamically favored to re-fill their vacancies with CO<sub>2</sub>. High Sr-substitution on the A site is undesired because it increases the oxygen non-stoichiometry of the perovskite [126, 133, 158, 186] and therefore only low Sr<sup>2+</sup> substitution was studied. This substitution induced changes in the oxidation state of the B site metal; as a consequence, the oxygen vacancy formation energies were enhanced [56, 86, 167, 186]. Substitution of the B site metal was still necessary to optimize the oxygen vacancy formation energy. Presence of copper in the B sites favored the formation of oxygen vacancies when compared to Fe perovskites. High Cu-substitution, however, lead to the decomposition of the perovskite, which is described in detail next.

#### 5.3.1 Effect of Cu Addition in the Crystalline Structure, Oxygen Vacancies Formation and Reducibility of the Samples

The effect of Cu doping on the diffraction patterns and perovskite crystalline structure are shown in Figure 5.1 and Table 5.1. The Cu0 sample only exhibited a single-phase orthorhombic (O) perovskite with a cell volume of 238.34 Å<sup>3</sup>. Small dopings of Cu (Cu10), decreased the

orthorhombic unit cell volume to  $237.84 \text{ \AA}^3$ , as expected due to the smaller size of Cu [154] compared to Fe. This effect was also observed when comparing the main diffraction line of the orthorhombic phases (020), which increased from  $32.33 2\theta^\circ$  for Cu0 to  $32.43 2\theta^\circ$  for Cu10, due to unit cell size decrease. A small amount of cubic CuO was detected at  $35.56$  and  $38.74 2\theta^\circ$ , with  $\sim 1\%$  relative intensity lines in the Cu10 sample.

In the Cu25 sample, the main diffraction line at  $32.37 2\theta^\circ$  was attributed to an orthorhombic (O) phase rich in Fe (cell volume  $237.99 \text{ \AA}^3$ ). A secondary phase (88.6% relative intensity) appeared at  $32.48 2\theta^\circ$ , possibly due to a tetragonal Cu-rich oxygen deficient phase,  $\text{La}_{0.75}\text{Sr}_{0.25}\text{Fe}_{1-y}\text{Cu}_y\text{O}_{3-\delta}$  (T1) with a cell volume  $454.13 \text{ \AA}^3$  (Figure 5.1 (b)). CuO was visible in higher proportions ( $\sim 5\%$  relative intensity) than on the Cu10 sample. The formation of the Cu-rich T1, and CuO, was presumably due to the difference in ionic radii of Fe and Cu and the preference of Cu to exist in lower oxidations states than Fe inside the perovskite. In consequence, the O phase tolerated only small substitutions of Cu.

The diffraction profile of Cu50 exhibited two secondary phases and CuO as impurity. The three main intensity lines are shown in the range  $32.2 - 32.8 2\theta^\circ$  (Figure 5.1 (b)). The main diffraction line ( $32.71 2\theta^\circ$ ) was attributed to a tetragonal oxygen deficient  $\text{A}_8\text{B}_8\text{O}_{20}$  (T2) structure [187]. The orthorhombic, Fe-rich phase (92.2% relative intensity) is seen at  $32.34 2\theta^\circ$ , a  $0.01 2\theta^\circ$  difference with respect to the Cu0 sample, suggesting that the incorporation of Cu into the structure is minimal, and the copper content in the structure was less than in the O phase of the Cu10 sample. The T1 phase (82.4% relative intensity) was also detected, with a main diffraction line at  $32.55 2\theta^\circ$  and a cell volume of  $453.82 \text{ \AA}^3$ . The decrease in its cell volume and the higher  $2\theta^\circ$  values for its main diffraction line, suggested that the Cu50\_T1 phase was richer in Cu than the Cu25\_T1.



The XRD profile of the Cu75 sample was similar to that of the Cu25. The main diffraction line ( $32.35\ 2\theta^\circ$ ) was attributed to the O phase with a unit cell volume of  $238.25\ \text{\AA}^3$ . The Cu75\_O phase shifted to lower  $2\theta^\circ$  values and exhibited a smaller cell volume, suggesting that this phase was richer in Fe than the Cu25\_O phase. The T1 phase was also evident at  $32.38\ 2\theta^\circ$  (94.5 % relative intensity) with a cell volume of  $460.61\ \text{\AA}^3$ . The Cu75\_T1 phase was likely richer in Fe than the Cu25\_T1 phase, as suggested by the T1 cell volume increase, and the shift in the diffraction pattern to lower  $2\theta^\circ$  values. The CuO lines had a relative intensity of ~6%, similar to the Cu25 sample. This finding was counterintuitive because the T1 and O crystalline phases on the Cu75 were richer in Fe than the phases found in the Cu25 sample. However, due to the favored thermodynamics for the inclusion of Fe vs. Cu on the B site, the similarity in the profiles for Cu25 and Cu75 suggested that in the Cu75 sample, a large proportion of Cu was in an amorphous phase, undetected by XRD.

In the Cu100 sample, the structure returned to a single-phase profile with a main diffraction line at  $\sim 32.91\ 2\theta^\circ$ , characteristic of a tetragonal structure similar to T1 but without Fe on the B site. The diffraction profile shifted to higher  $2\theta^\circ$  values and decreased its cell volume to  $453.49\ \text{\AA}^3$ . The Cu100 also had multiple unidentified diffraction lines. The most intense line (13% at  $37.89\ 2\theta^\circ$ ) was observed in a similar position to the most intense diffraction line of the highly unstable tetragonal  $\text{SrCu}_2\text{O}_2$  structure (reference 00-38-1178). The next most intense unidentified diffraction lines on the Cu25 XRD profile correspond to  $31.18$ ,  $31.26$  and  $38.73\ 2\theta^\circ$  with 6.8, 6.3 and 5.3% intensity respectively. These peaks could be attributed to an orthorhombic  $\text{Sr}_{14}\text{Cu}_{24}\text{O}_{41}$  structure, which is formed from the reaction of  $\text{SrCu}_2\text{O}_2$  with  $\text{O}_2$  at temperatures higher than  $300\ ^\circ\text{C}$  [188]. The rest of the unidentified diffraction lines had relative intensities lower than 5%.

The oxygen vacancy formation profiles of the perovskites (Figure 5.2 (a)) and the oxygen vacancies formed,  $\delta$  (Figure 5.2 (b)) were used to compare the samples in terms of reducibility. Overall, incorporation of Cu decreased the stability of the perovskite. The Cu0 sample exhibited enhanced stability when compared to the Cu-doped samples due to its less favored oxygen vacancy formation energy. Desorption of surface oxygen likely contributed to the profiles to a small extent. The profile of Cu10 demonstrated only one O<sub>2</sub> formation area from 810 to 870 °C (peak at 860 °C) consistent with having only one perovskite phase (Figure 5.1). The Cu25 sample, which initially possessed two main crystalline phases, produced 2.5 times more oxygen vacancies than the Cu10 sample, possibly due to oxygen vacancy formation and subsequent partial decomposition of the T1 structure, as suggested by post-reduction XRD (shown later). Decomposition of the samples to Cu<sub>2</sub>O was detected via red stains left on the reactors subsequent to the experiments, particularly in the samples with high Cu substitution. Even though, intuitively, the Cu25 sample was expected to initiate the formation of oxygen vacancies at lower temperatures than Cu10, the oxygen vacancies formation on the Cu25 sample occurred in the range of 810 to 900 °C (peak at 890 °C). This phenomenon was studied with DFT and will be discussed in section 5.3.3.

The two areas in the profiles of the Cu50, Cu75 and Cu100 samples, correlate with the co-existence of multiple crystalline phases. Likely, for the Cu50 and Cu75 samples, the two most predominant phases (O and T1) formed oxygen vacancies and decomposed to other phases at higher temperatures. The T2 structure, is known to be stable in its oxygen deficient state [189]. The first oxygen vacancy formation area in the Cu50 and Cu75 samples peaked at approximately the same temperature (870 °C) and formed almost the same amount of oxygen vacancies, which

is consistent with the presence of similar crystalline phases. The second oxygen vacancy formation area was larger in Cu75 than in Cu50, as it is expected due to its increased Cu doping.

The Cu100 sample also exhibited two oxygen vacancy formation areas, which could be attributed to decomposition of either the T3 or the unidentified phases.

The reduction profiles of the samples, in the presence of a reducing agent ( $H_2$ ), changed with Cu content (Figure 5.3 (a)). The O atoms removed from each perovskite during the reduction period (Figure 5.3 (b)), correspond to the mol of  $H_2O$  formed per mol of perovskite [46]. The Cu0 sample exhibited two reduction areas. The first one started at 350 °C and peaked at 550 °C. The smallest initial peak is likely formed during the reduction of the  $Fe^{4+}$  ions to  $Fe^{3+}$ , while the second one (onset at ~500 °C) was formed due to reduction of  $Fe^{3+}$  ions. In the samples with both metals on the B site, the onset reduction and peak reduction on the first area decreased by 100 and 300 °C, respectively.

The Cu10 sample had two low-temperature areas, the first from 250 to 350 °C potentially due to the reduction of  $Cu^{3+}$  and  $Fe^{4+}$  ions. The second reduction area (350 to 450 °C) was attributed to the reduction of the  $Fe^{3+}$  ions. The high temperature reduction area was larger in Cu0 than in Cu10 due to higher Fe content on the Cu0 sample, when compared to the Cu10 sample. In general, the low and high-temperature reduction areas had a direct and inverse relation to Cu content, respectively (Figure 5.3(b)). The Cu75 and Cu100 samples reduce almost completely below 650 °C. The  $m/z=18$  peak observed at ~850 °C on the Cu75 sample, was attributed to the reverse water gas shift reaction between previously adsorbed carbon dioxide and hydrogen.

The samples with both Cu and Fe on the B site (Cu10, Cu25, Cu50, Cu75), exhibited lower onset reduction temperatures than the Cu100 and Cu0. This effect was a consequence of

the combined stability of Fe with the reducibility of Cu. The TPR profile for Cu100 seemed to undergo a lumped reduction below 550 °C. A characteristic that makes an oxide material ideal for RWGS-CL or thermochemical cycles, is to have tunable oxygen vacancies as a function of temperature. A lumped reduction such as the one suffered by Cu100 is difficult to control. More discrete profiles such as the Cu0 and Cu10 are desired due to the multiple reduction areas with different onset and peak temperatures.

### **5.3.2 Effect of Cu Doping in the CO Formation Profiles of $\text{La}_{0.75}\text{Sr}_{0.25}\text{Fe}_{1-y}\text{Cu}_y\text{O}_3$**

#### **Perovskites**

The effects of Cu doping on CO<sub>2</sub> conversion characteristics for the Fe-based perovskite were investigated on samples with low doping of Cu (Cu10, Cu25). These samples were chosen due to their enhanced stability, as opposed to the high Cu-doped samples. The Cu0 sample was tested for comparison purposes. Prior to the temperature-programmed CO<sub>2</sub> conversion, the samples were reduced at 450 °C under 10% H<sub>2</sub>/He for 30 min. This temperature was chosen because it was at the end of the low-temperature reduction area for the samples containing both Cu and Fe, and inside that area for the Cu0 sample.

During the isothermal reduction period, water was formed, which was quantified as mol of H<sub>2</sub>O formed per mol of perovskite. The reduction increased with copper content. The Cu0, Cu10 and Cu25 samples formed 0.38, 0.44 and 0.65 mol of H<sub>2</sub>O per mol of perovskite, respectively (Table 5.2). These values suggested that the main phases of the Cu0, Cu10 and Cu25 samples only underwent minor reductions. Post-reduction XRD (Figure 5.4) confirmed that the samples retained their main crystalline structure. The reduced Cu10 and Cu25 samples exhibited increased crystallinity, as evident by the disappearance of the amorphous shoulder at low 2θ ° values, and the narrower main diffraction lines. The T1 phase was still present although

the main diffraction line decreased in relative intensity to 63.3%. Both phases were oxygen deficient, evident from the shift of XRD profiles to lower  $2\theta$  ° values. CuO was reduced to Cu<sup>0</sup> on the Cu10 and Cu25 samples. The Cu0 sample also underwent a reduction, as noted by the appearance of metallic Fe at  $\sim 45$   $2\theta$  °.

The onset CO production temperature was  $\sim 450$  °C for Cu0 and Cu10 (Figure 5.5) and the peak CO production occurs at 540 and 570 °C for Cu10 and Cu0, respectively. The similar onset temperatures suggested that Cu did not contribute to a catalytic effect. CO formation was not detected on the Cu25 sample. Expressly, the amount of O removed from the perovskites increased with Cu doping, and the CO production decreased with Cu. Also, the Cu10 sample only re-oxidized 13.6% of its oxygen vacancies, while the Cu0 sample re-oxidized 23.7% of the oxygen vacancies formed during the isothermal reduction (Table 5.2). These findings are not consistent with previous results, which showed that oxygen vacancies are the primary driving force for the CO<sub>2</sub> bond breaking in La<sub>0.75</sub>Sr<sub>0.25</sub>FeO<sub>3</sub> samples [46] and will be discussed in section 4.4. The decreased CO production on the Cu doped samples and the lower percentage of re-oxidized vacancies indicated that the RWGS-CL would be less favored than on the Cu0 sample, therefore, repeated cycle studies were not performed.

It is important to mention that in CO hydrogenation experiments, others have shown that introducing Cu ions into the LaMnO<sub>3</sub> perovskite promotes the formation of methanol from CO hydrogenation [190]. This suggested that Cu doping could promote the conversion of CO to other methanol on the La<sub>0.75</sub>Sr<sub>0.25</sub>FeO<sub>3</sub> perovskite. However,  $m/z = 31$  was tracked during the temperature-programmed CO<sub>2</sub> experiments and no formation of methanol was detected, this is due to the H<sub>2</sub> and CO<sub>2</sub> remaining separated during the looping-type experiment.

## 5.4 Discussion

The inhibition of CO formation during the temperature-programmed CO<sub>2</sub> oxidation experiments was directly proportional to Cu content. In the following sections, we investigate whether the effect was due to the changes in the Cu phase (Cu outside the perovskite) or due to the effect of B-site Cu substitution inside the perovskite structure.

### 5.4.1 Effect of Cu Containing Secondary Phases

CuO was found on the XRD profiles of the Cu10 and Cu25 samples in 1 and 5% relative intensities, respectively. The detail that relative intensities was a factor of 5 different whereas the Cu amount in the sample was factor of 2.5 different suggested the fraction of Cu in secondary phases was increasing with Cu amount in the sample. An impurity rich in Cu initially points to the conclusion that the perovskite was B-site deficient, but B-site cationic vacancies are not thermodynamically favored [56] and therefore, are rarely seen. Ge et al. [191] determined that high concentrations of B site vacancies on (Ba<sub>0.5</sub>Sr<sub>0.5</sub>)(Co<sub>0.8</sub>Fe<sub>0.2</sub>)<sub>y</sub>O<sub>3-δ</sub> membranes induced the appearance of A-metal oxides near the membrane surface, detected by FTIR but undetected by XRD. Previous efforts [149] found that, as Fe content decreased in La<sub>0.6</sub>Sr<sub>0.4</sub>Co<sub>y</sub>Fe<sub>1-y</sub>O<sub>3-δ</sub>, the surface composition of the oxides was enriched in La and Sr. An increased La and Sr concentration near the surface, presumably in the form of base metal oxides, could highly favor the adsorption of CO<sub>2</sub> as carbonate [192, 193] as opposed to breaking the C-O bond on the oxygen vacancy site of the perovskite oxide. To investigate potential carbonate adsorption, FTIR was performed on the Cu25 sample with and without CO<sub>2</sub> adsorption. A sample was treated to an isothermal reduction in H<sub>2</sub>/He for 20 min, He flushing for 20 min, and subsequent CO<sub>2</sub> flow for 20 min at 550 °C. Vibrations in the carbonate regions decreased in intensity (and some even disappeared) when compared to the same sample treated in He at 550 °C for the same period of

time where some carbonates from the atmospherically adsorption were not removed. This comparison suggested that carbonate formation was not the issue.

In addition to surface enriched oxides of La and Sr, Cu phases must be present. In this study, the samples were reduced for 10 minutes more than in previous efforts [46], therefore, metallic Fe<sup>0</sup> was also noted on the reduced La<sub>0.75</sub>Sr<sub>0.25</sub>FeO<sub>3</sub>. This Fe<sup>0</sup> could have enhanced CO formation, due to the enhanced dissociative chemisorption of CO<sub>2</sub> in Fe [137] surfaces. Dissociative chemisorption of CO<sub>2</sub> has been proven highly unfavorable on Cu surfaces [137, 173, 194, 195]. Therefore, higher amounts of metallic Cu present on the Cu25 sample could be inhibiting CO production due to highly electronegative localized CO<sub>2</sub> adsorption on Cu nanoparticles, which is more thermodynamically favored than CO<sub>2</sub> dissociation. But, CO<sub>2</sub> conversion to CO has been achieved on Cu vapor-deposited on TiC(001) [196]. In both Cu-containing samples (Cu10 and Cu25) tested for CO<sub>2</sub> conversion, the isothermal H<sub>2</sub> treatment reduced the CuO phase to metallic Cu<sup>0</sup>, which might be sintering upon reduction higher than 400 °C [90].

To investigate the effect of the reduced Cu<sup>0</sup> on CO formation, five consecutive cycles of RWGS-CL are studied (similar to previous studies [46]) on 5% Cu on La<sub>0.75</sub>Sr<sub>0.25</sub>FeO<sub>3</sub> synthesized by wet impregnation. The rates of CO formation on 5% Cu / La<sub>0.75</sub>Sr<sub>0.25</sub>FeO<sub>3</sub> were compared to those of La<sub>0.75</sub>Sr<sub>0.25</sub>FeO<sub>3</sub> (Table 3). CO formation was not inhibited by additional Cu, and the formation rates were very similar to those of La<sub>0.75</sub>Sr<sub>0.25</sub>FeO<sub>3</sub>. Although the temperatures were much lower than the synthesis temperature (550 vs 950°C), it is possible that the decrease with the 5% Cu / La<sub>0.75</sub>Sr<sub>0.25</sub>FeO<sub>3</sub> was associated to Cu migration into the perovskite oxide. Regardless, this comparison indicated that excess amount of Cu external to the perovskite oxide did not inhibit CO production.

### 5.4.2 Effects of B-site Doping of Cu into the $\text{La}_{0.75}\text{Sr}_{0.25}\text{FeO}_3$ Perovskite

Experimental studies (Figures 5.1 and 5.2) showed that increasing Cu content increased the oxygen vacancies formation abilities of the  $\text{La}_{0.75}\text{Sr}_{0.25}\text{Fe}_{1-Y}\text{Cu}_Y\text{O}_3$  materials. Even though the  $\text{CuO}$  and Cu-doped perovskites remained stable in the reduced state (Figure 5.4), the Cu-doped materials have a lower oxygen affinity than the  $\text{CuO}$  samples (as suggested by DFT, not shown here), which lowered the thermodynamic drive to re-fill the oxygen vacancies for the  $\text{Cu}_{10}$  and  $\text{Cu}_{25}$  samples, than in the  $\text{CuO}$  sample, particularly with a poor oxidant ( $\text{CO}_2$  [123]). Nakamura et al. [126, 133] studied similar materials ( $\text{La}_{1-x}\text{Sr}_x\text{CoO}_{3-\delta}$ ) and found that increasing the perovskites reducibility, decreases its ability to refill its oxygen vacancies. These results and findings contrasted significantly from results with a less reducible perovskite oxide. For the  $\text{La}_{0.75}\text{Sr}_{0.25}\text{FeO}_3$  sample ( $\text{Cu}_0$ ), production of  $\text{CO}$  increased (0.02, 0.13, 0.15 mol  $\text{CO}/\text{mol}$   $\text{La}_{0.75}\text{Sr}_{0.25}\text{FeO}_3$ ) with increasing reduction in the perovskite structure (0.13, 0.36, 0.71 mol  $\text{H}_2\text{O}/\text{mol}$   $\text{ABO}_3$  respectively). In these experiments, various amounts of  $\text{H}_2\text{O}$  were formed during isothermal reduction (at 3, 13.6 and 30 min respectively) under 10%  $\text{H}_2/\text{He}$ . This comparison, on conjunction with the Cu supported on  $\text{La}_{0.75}\text{Sr}_{0.25}\text{FeO}_3$  (Table 5.3) confirms that the stability of the reduced material is center to the low levels of  $\text{CO}$  production from the Cu containing samples.

### 5.5 Conclusion

The effects of Cu doping in Fe-based perovskites on the conversion of carbon dioxide to carbon monoxide were investigated. Six materials  $\text{La}_{0.75}\text{Sr}_{0.25}\text{Fe}_{1-Y}\text{Cu}_Y\text{O}_3$  with  $Y = 0, 0.1, 0.25, 0.5, 0.75$  and  $1$ , (labeled  $\text{Cu}_{100*Y}$ ) were synthesized, characterized, and tested for their reduction and oxygen vacancies formation capabilities. Select reduced materials were tested for their ability to convert  $\text{CO}_2$  to  $\text{CO}$ . Cu addition reduces the stability of the perovskite and



promotes the formation of oxygen vacancies. DFT calculations (not shown here) confirmed that, for the Cu0, Cu10 and Cu25 samples, the oxygen vacancies formation energies depend on both the Cu content and the extent of oxygen vacancies formed ( $\delta$ ). Only the perovskites with lowest Cu substitution ( $Y=0.1$ ) and no Cu ( $Y=0$ ) were able to produce CO. Results indicated that incorporating Cu into the perovskite structure induced a loss of oxygen affinity and decreased the ability of the perovskite to re-oxidize.

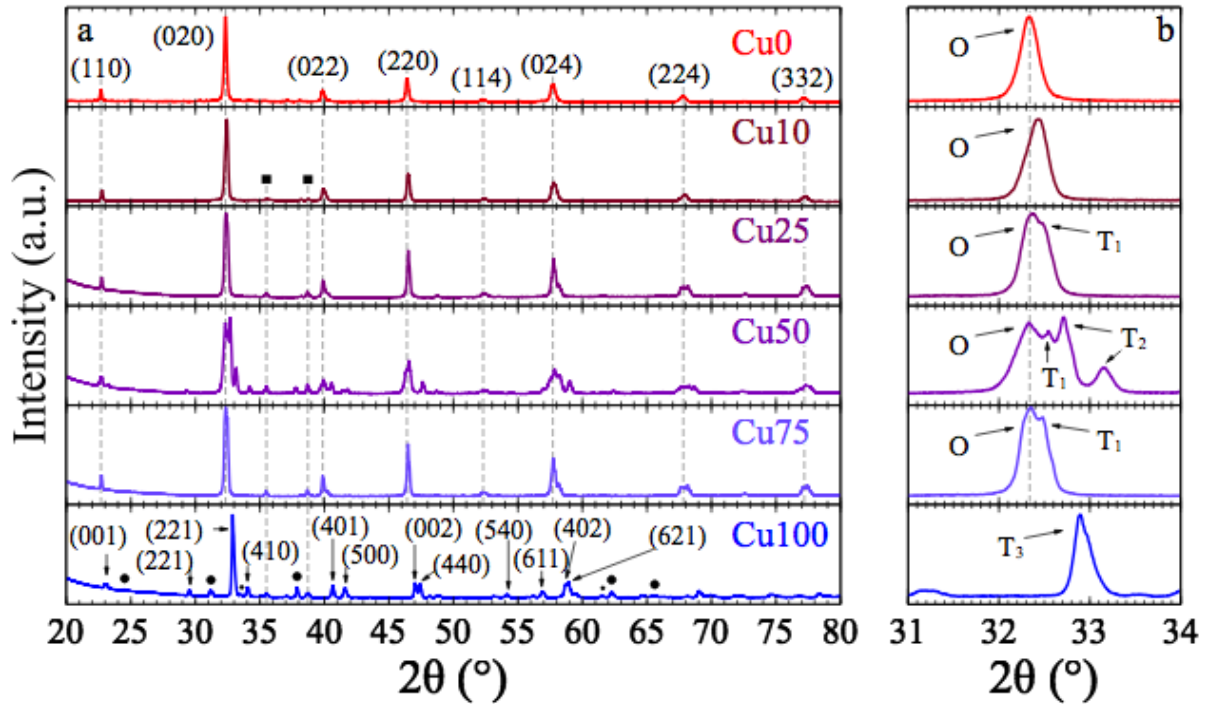


Figure 5.1 X-ray results. (a) X-ray diffraction patterns of the Cu-doped samples. Cu0 to Cu75 exhibit predominantly orthorhombic (O) crystalline structures (reference 00-035-1480). From Cu10 until Cu100, cubic CuO (■) was also found (reference 00-001-0428). The Cu100 sample exhibited a tetragonal pattern with at least one unidentified crystalline structure (●). (b) Main diffraction lines from 31 to 34  $2\theta$   $^\circ$ . The Cu25 and Cu75 samples exhibit the O phase and a secondary phase (T<sub>1</sub>), possibly a tetragonal  $\text{La}_{0.75}\text{Sr}_{0.25}\text{Fe}_{1-y}\text{Cu}_y\text{O}_{3-\delta}$ . The Cu50 sample exhibits three main phases: O, T<sub>1</sub> and a tetragonal  $\text{A}_8\text{B}_8\text{O}_{20}$  structure (T<sub>2</sub>, reference 01-083-0366). The Cu100 sample exhibits a tetragonal  $\text{La}_{0.75}\text{Sr}_{0.25}\text{CuO}_{2.44}$  (T<sub>3</sub>, reference 00-046-0653). Profiles are normalized to most intense line.

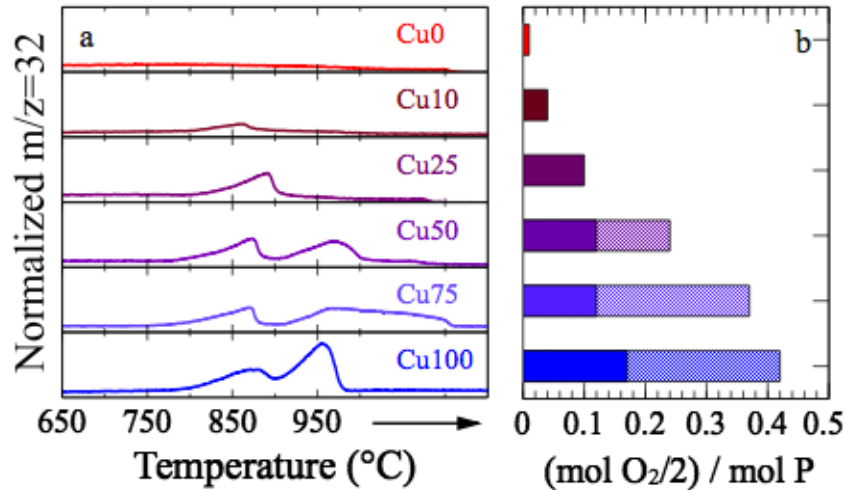


Figure 5.2 TP-Ovac formation results. (a) Temperature-programmed oxygen vacancy formation. The  $m/z=32$  signal was normalized with respect to He. (b) Quantification of the oxygen vacancies formed ( $(\text{mol of O}_2 / 2) / \text{initial mol P}$ ). For Cu50, Cu75 and Cu100, the solid bars represent the oxygen vacancies formed from 750 to  $\sim 900$  °C and translucent bars represent the oxygen vacancies formed from 900 °C until the stabilization of the  $m/z=32$  signal. The Cu10 oxygen vacancy formation experiment was performed three times and the standard deviation was  $1.5e^{-3}$  mol of  $\text{O}_2/2 / \text{mol P}$ .

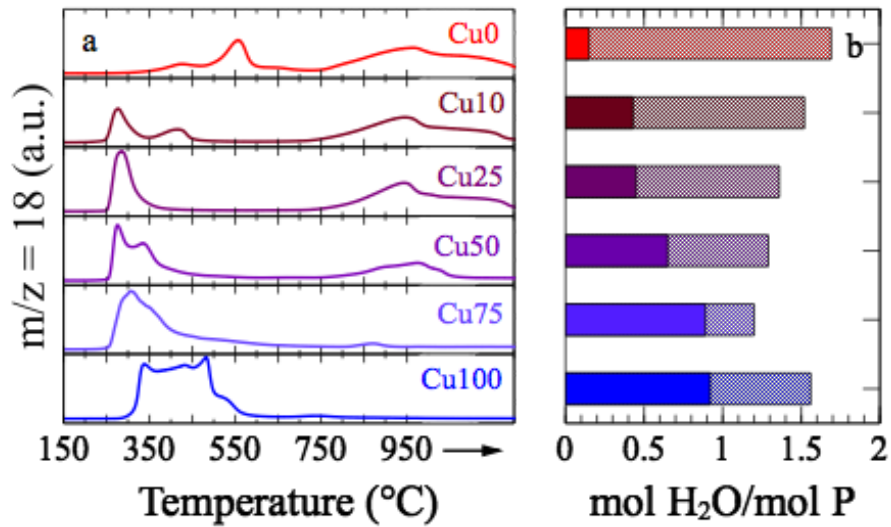


Figure 5.3 TPR results. (a) Temperature-programmed reduction of the samples under 10%  $\text{H}_2/\text{He}$ . (b) Quantification of moles of water produced during the reduction normalized by the initial moles of perovskites. The solid bars represent water formation below 450 °C, the translucent bars represent the reduction above 450 °C. The solid bars increase in size with Cu, showing that Cu addition increases the reducibility of the samples at lower temperatures.

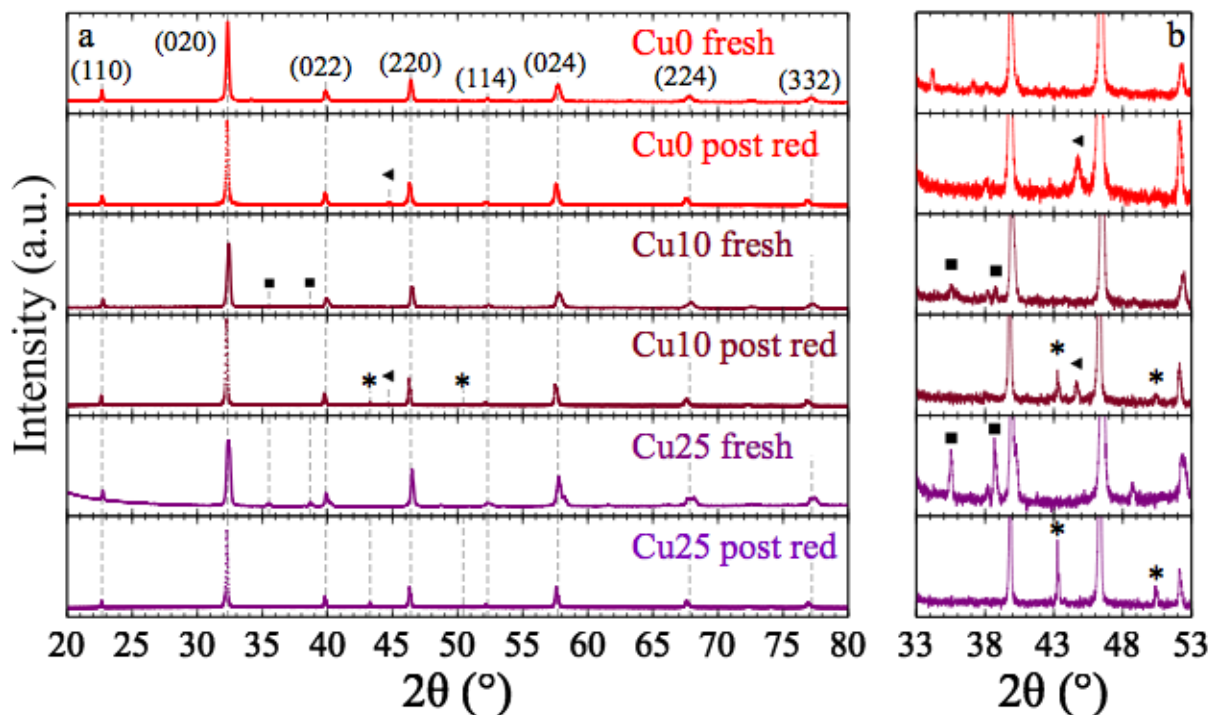


Figure 5.4 XRD patterns after isothermal reduction at 450 °C in 10% H<sub>2</sub>/He for 30 min. Fresh patterns are repeated from Figure 5.1. All samples exhibited mainly an orthorhombic (O) crystalline structure. Other phases found: metallic Fe (◄), metallic Cu (\*) and CuO (■). The profiles are normalized to the most intense peak.

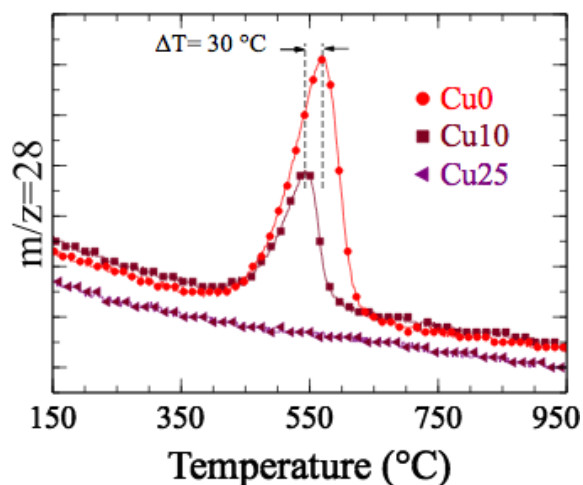


Figure 5.5 Temperature-programmed CO formation on Cu0, Cu10 and Cu25 (raw signals of m/z=28) after isothermal reduction at 450 °C in 10% H<sub>2</sub>/He for 30 min.

Table 5.1 Abbreviations.

Abbreviation	Sample
Cu0	$\text{La}_{0.75}\text{Sr}_{0.25}\text{FeO}_3$
Cu10	$\text{La}_{0.75}\text{Sr}_{0.25}\text{Cu}_{0.10}\text{Fe}_{0.90}\text{O}_3$
Cu25	$\text{La}_{0.75}\text{Sr}_{0.25}\text{Cu}_{0.25}\text{Fe}_{0.75}\text{O}_3$
Cu50	$\text{La}_{0.75}\text{Sr}_{0.25}\text{Cu}_{0.50}\text{Fe}_{0.50}\text{O}_3$
Cu75	$\text{La}_{0.75}\text{Sr}_{0.25}\text{Cu}_{0.75}\text{Fe}_{0.25}\text{O}_3$
Cu100	$\text{La}_{0.75}\text{Sr}_{0.25}\text{CuO}_3$

Table 5.2 Unit cell parameters of the perovskite phases for the fresh  $\text{La}_{0.75}\text{Sr}_{0.25}\text{Fe}_{1-Y}\text{Cu}_Y\text{O}_3$  samples as calculated from X-ray diffraction data.

Sample	Main diffraction line ( $2\theta$ °) and intensity (%)	Phase	a (Å)	b (Å)	c (Å)	Cell volume (Å <sup>3</sup> )
Cu0	32.33 (100%)	Orthorhombic	5.53	5.53	7.80	238.34
Cu10	32.43 (100%)	Orthorhombic	5.53	5.50	7.82	237.84
Cu25	32.37 (100%)	Orthorhombic	5.52	5.52	7.81	237.99
	32.48 (88.6%)	Tetragonal_1	10.94	10.64	3.90	454.13
Cu50	32.71 (100%)	Tetragonal_2	10.79	10.79	3.90	454.28
	32.34 (92.2%)	Orthorhombic	5.50	5.54	7.85	239.48
	32.55 (82.4%)	Tetragonal_1	10.81	10.78	3.89	453.82
Cu75	32.35 (100%)	Orthorhombic	5.50	5.53	7.82	238.25
	32.38 (94.5%)	Tetragonal_1	10.85	10.85	3.91	460.61
Cu100	32.91 (100%)	Tetragonal_3	10.84	10.85	3.86	453.49

Table 5.3 H<sub>2</sub>O and CO formation on the  $\text{La}_{0.75}\text{Sr}_{0.25}\text{Fe}_{1-Y}\text{Cu}_Y\text{O}_3$  (Y=0, 0.10 and 0.25) samples during the temperature-programmed oxidation with CO<sub>2</sub> (CO formation) experiments.

Sample	(mol H <sub>2</sub> O/mol P)	(mol CO/mol P)	% of vacancies re-oxidized
Cu0	0.38	0.09	23.7
Cu10	0.44	0.06	13.6
Cu25	0.65	--	--

Table 5.4 Rate of CO formation at T = 550°C on the RWGS-CL process on La<sub>0.75</sub>Sr<sub>0.25</sub>FeO<sub>3</sub> and Cu-supported La<sub>0.75</sub>Sr<sub>0.25</sub>FeO<sub>3</sub> perovskite oxides. Only data after the third cycle is shown because it represents the rates upon stabilization. The first two reductions/oxidation cycles on the 5%Cu/La<sub>0.75</sub>Sr<sub>0.25</sub>FeO<sub>3</sub> sample were used to reduce copper oxide to metallic Cu<sup>0</sup>. Data from these two cycles were not considered to be representative of accurate oxygen vacancies formation due to additional water production from oxygen in the copper oxides.

Sample	μmol CO/ gram of perovskite/min		
	Cycle 3	Cycle 4	Cycle 5
La <sub>0.75</sub> Sr <sub>0.25</sub> FeO <sub>3</sub> [46]	69.58	77.15	73.09
5% Cu/ La <sub>0.75</sub> Sr <sub>0.25</sub> FeO <sub>3</sub>	69.23	62.36	61.65

## CHAPTER 6: ENERGY REQUIREMENTS OF THE PROCESS

### 6.1 Overview

This chapter focuses on calculating the energy required to capture CO<sub>2</sub> from a power plant and converting it to CO through the RWGS-CL process using La<sub>0.75</sub>Sr<sub>0.25</sub>FeO<sub>3</sub>. Two potential scenarios for synthetic fuel production from CO hydrogenation, as depicted on Figure 3.1, will be considered: (i) methanol and (ii) diesel (FTS fuel). O<sub>2</sub> is produced from both scenarios, but selling this product won't be considered for the economic calculations.

Twice the amount of the necessary RWGS-CL packed bed reactors is envisioned to be used, so that a 4 port valve can be employed to provide CO<sub>2</sub> to the reactors with the reduced perovskites, while simultaneously, H<sub>2</sub> regenerates the re-oxidized perovskites, as depicted in Figure 6.1. This set up has the purpose of maintaining a constant conversion process. Additionally, preliminary economic calculations and energy requirements are also included.

### 6.2 Design Parameters

#### 6.2.1 CO<sub>2</sub> Source

Florida is ranked as the 6<sup>th</sup> state with the highest CO<sub>2</sub> emissions from fossil fuel combustion [197], in 2013 it produced 218 mega tonnes of CO<sub>2</sub> [198]. The Florida Central Power & Lime Power Plant, which in 2012 proposed a transition from being fueled by coal to being partly fueled by biomass, is one of the closest to the University of South Florida. Its current CO<sub>2</sub> emissions estimate is 1.06 mega tonnes CO<sub>2</sub>/year [199] from both fuel (woody biomass and coal) units. This CO<sub>2</sub> yearly production translates to 45.97 kmol CO<sub>2</sub>/min. This

plant is projected to generate 70 to 80 MW [199], then, 75 MW will be used for the calculations. Burning biomass is considered to be carbon neutral because the CO<sub>2</sub> emitted is compared with the CO<sub>2</sub> consumed by the biomass while it is growing, therefore, not much information is available regarding sequestration cost in biomass-based power plants. However, it has been previously stated, that the conversion of biomass can only contribute to lowering CO<sub>2</sub> emissions if the product of its conversions is fuel synthesis, else, CO<sub>2</sub> emissions wouldn't decrease, they would just enter another CO<sub>2</sub> exchange cycle [200, 201]. Therefore, preliminary energetic and economic costs will be calculated for the Power & Lime Power Plant.

All calculations reflected in the body of this chapter are based on designing a RWGS-CL system that can convert 45.97 kmol CO<sub>2</sub>/min to CO in a constant process. The costs of CO<sub>2</sub> capture will be taken from a conference proceeding by David and Herzog [202], where it was determined as 7.7 ¢/kWh (levelised cost) for post combustion power plants, with an energy requirement of 0.317 kWh/Kg of CO<sub>2</sub> processed (plants with highest energy requirements), using MEA scrubbing. Multiplying these two amounts, a capture cost of 24.41 USD/tonne of CO<sub>2</sub> is obtained.

Given the stability of the CO<sub>2</sub> molecule, in the following calculations, the energy density (specific energy) will be taken as the coal energy density but with a negative sign (-25 MJ/Kg).

### 6.2.2 H<sub>2</sub> Source

In order to keep the process renewable, H<sub>2</sub> will be modeled as generated from concentrated solar power, specifically by solar towers. Solar towers have high investment costs but lower operation and maintenance costs than other concentrated solar technologies, molten salts or synthetic oils can be used as heat transfer fluids [203]. According to the International Renewable Energy Agency, the levelised cost of electricity generated by solar concentrators is



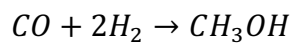
between 0.17 and 0.29 2010 USD/kWh [203]. 0.17 USD/kWh will be used as the electricity cost. Then, extrapolating from Turner [139] and Levene et al. [204], the cost of renewable H<sub>2</sub> from electrolysis at an electricity cost of 0.17 USD/kWh is ~ 11 USD/Kg H<sub>2</sub>. The specific energy of H<sub>2</sub> was taken to be 142 MJ/KgH<sub>2</sub>.

### 6.2.3 RWGS-CL Reactor

The reactor was assumed to be packed with La<sub>0.75</sub>Sr<sub>0.25</sub>FeO<sub>3</sub>. The maximum amount of oxygen vacancies generated during each H<sub>2</sub> reduction ( $\delta=0.5$ ) was completely re-oxidized by CO<sub>2</sub> upon the CO<sub>2</sub>-oxidation step. Reactions take place isothermally at 550 °C and 1 bar with 100% selectivity towards CO. The density of the material was assumed as  $\rho = 660 \text{ Kg/m}^3$ , as experimentally determined for a similar material [205]. Investment and operation and maintenance costs were not considered, and the materials were assumed stable throughout the study.

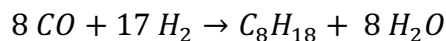
### 6.2.4 CO Hydrogenation Products

Two possibilities will be proposed as the CO hydrogenation products. First, methanol, following the reaction:



with a specific energy of 19.7 MJ/Kg CH<sub>3</sub>OH and a minimum selling price of 6.73 USD/GGE [119] from H<sub>2</sub> and CO produced from solar H<sub>2</sub>O and CO<sub>2</sub> splitting respectively.

And FTS fuel (diesel, C<sub>8</sub>H<sub>18</sub>) according to the reaction below:



with a specific energy of 48 MJ/Kg diesel and a reference minimum selling price of 7.01 USD/GGE [119] from H<sub>2</sub> and CO produced from solar H<sub>2</sub>O and CO<sub>2</sub> splitting respectively.

Selectivity is assumed as 100% to the desired product at both reactions, and material deactivation (or down time for regeneration) was not considered. Systems are assumed to be isothermal and isobaric, and costs (investment and operation and maintenance) were not considered for either reaction.

### 6.3 Results

The results obtained from the preliminary calculations are summarized on Table 6.1. As part of the design parameters, both systems consume the same amount of CO<sub>2</sub>, but the combined RWGS-CL with FTS system consumes less water because the FTS reaction produces water, that can be recycled to the H<sub>2</sub> generation system. Nonetheless, the combined FTS system requires more hydrogen because the reaction requires 2.125 moles of H<sub>2</sub> per mol of CO, whereas the methanol combined system requires 2 moles of H<sub>2</sub> per mol of CO. The mole balances for the combined FTS and methanol systems are depicted in Figure 6.2. As shown on the figure, the combined methanol system produces almost 100% more O<sub>2</sub> than the combined FTS process, which, in both cases, could be sold to increase profits.

The production of methanol is 99% higher (in volume) than the production of FTS fuel (modeled as C<sub>8</sub>H<sub>18</sub>), however, when compared by their energy content (in gallon gas equivalent, GGE), production of C<sub>8</sub>H<sub>18</sub> is 14% higher, which translates to 18% more revenue from selling the products (Table 6.1). Due to a higher H<sub>2</sub> consumption by the combined FTS system, it has a 4.17% higher solar H<sub>2</sub> cost. When Kim et al's [119] minimum selling price for methanol (6.73 USD/GGE) and FTS fuel (7.01 USD/GGE) are used, the economic analysis results in severe losses, of 43.5 billion USD (thousand millions) and 37.7 billion USD respectively. These losses are due to the high cost of solar H<sub>2</sub> (11 USD/kg). Nonetheless, it is important to note, that the losses from the combined FTS system are smaller due to the higher energy content of C<sub>8</sub>. If the

cost of solar hydrogen was maintained at 11 USD/kg, the breakeven point for methanol and  $C_8H_{18}$  would be 12.35 USD/GGE and 11.28 USD/GGE respectively. Otherwise, the cost of solar  $H_2$  would need to be 6 USD/Kg so that the prices of the products match Kim et al's [119] minimum selling prices.

In terms of energy, neither of the products matches the energy content of  $H_2$ . The energy that could be produced from directly combusting the hydrogen that is required to synthesize both products is 29% and 35% higher than the energy that would be obtained from combusting methanol or diesel, respectively. Nonetheless, if the stability of the  $CO_2$  molecule and the energy required for its conversion is considered, then the process can be compared in the transformation of a molecule that is highly inactive to fuels. If the energy required to convert  $CO_2$  is considered, then the implementation of both combined processes becomes energy positive, in other words, the energy content of the products is higher than that of the reactants.

Table 6.1 Results from preliminary economic and energy assessment

Parameters	FTS	Methanol
Global mass balance		
CO <sub>2</sub> input (kmol CO <sub>2</sub> /min)	45.97	45.97
H <sub>2</sub> needed (kmol H <sub>2</sub> /min)	143.64	137.90
moles of product (kmol/min)	5.746	45.97
Additional H <sub>2</sub> O (kmol H <sub>2</sub> O/min)	51.71	91.93
Economic results		
Production (Million gal/year)	7,777.40	15,495.28
Production (Million GGE/year)	8,837.95	7,747.64
Sales of product (Million USD/year) <sup>a</sup>	61,954.05	52,141.60
CO <sub>2</sub> cost (Million USD/year)	25.95	25.95
Solar H <sub>2</sub> cost (Million USD/year)	99,657.10	95,670.81
Losses= product sales – H <sub>2</sub> cost (Million USD/year)	-37,703.05	-43,529.21
Breakeven point (USD/GGE)	11.28	12.35
Energy		
Energy that could be produced from directly combusting the H <sub>2</sub> used to synthesize the fuel (MJ/min)	40,794.09	39,162.33
Required to convert CO <sub>2</sub> (MJ/min) <sup>b</sup>	-50,573.18	-50,573.18
Obtained from burning fuel (MJ/min)	31,501.96	29,012.67
Fuel – H <sub>2</sub> – CO <sub>2</sub>	41,281.05	40,423.52
Fuel – H <sub>2</sub>	-9,292.14	-10,149.66

<sup>a</sup> with Kim et al. [62] minimum selling prices.

<sup>b</sup> modeled as inverse of coal

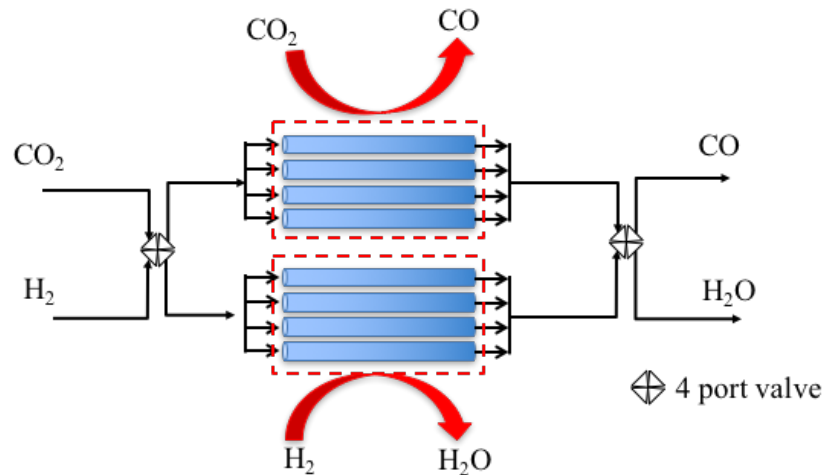


Figure 6.1 Schematic representation of the reactor configuration on the applied RWGS-CL process. The representation has been customized to the described power plant.

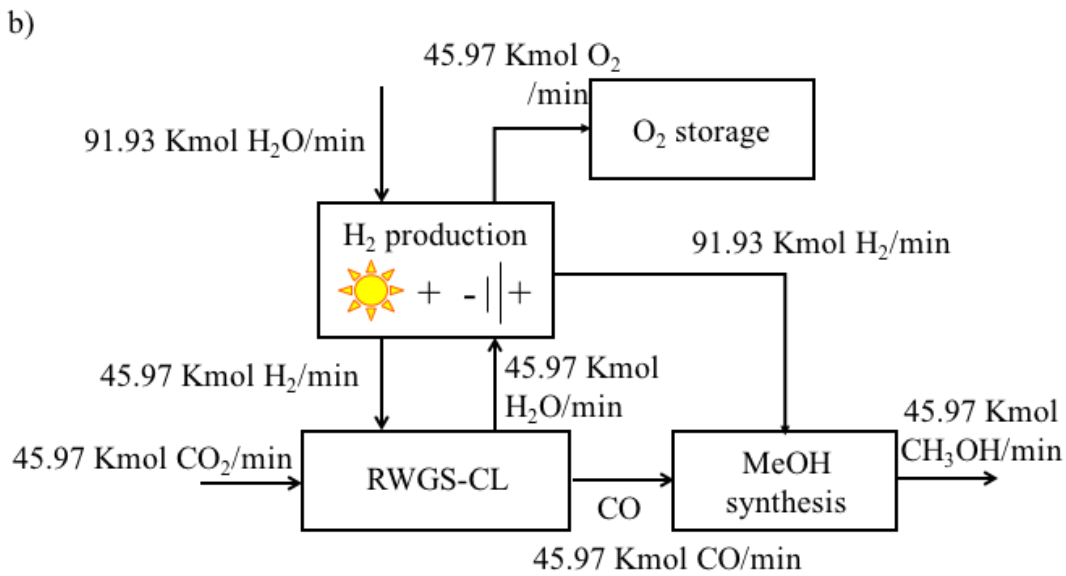
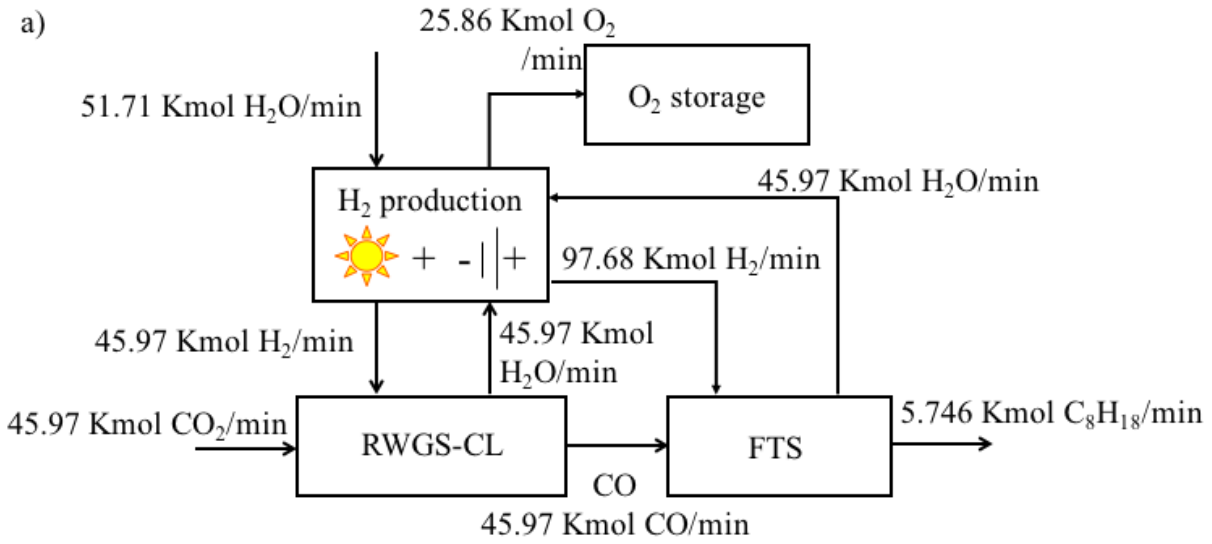


Figure 6.2 Mass balance scheme of the RWGS-CL combined processes. (a) with FTS and (b) with methanol.

## CHAPTER 7: CONCLUSIONS AND FUTURE WORK

### 7.1 Conclusions

In the present study, the reverse water gas shift chemical looping (RWGS-CL) process for the conversion of CO<sub>2</sub> to CO was developed. The incorporation of chemical looping to the conventional reverse water gas shift (RWGS) reaction avoided the deactivation of the catalyst and suppressed formation of methane, which are common drawbacks of conventional RWGS. The RWGS-CL process was demonstrated with (La,Sr)(Co,Fe,Cu)O<sub>3</sub> perovskites. Bulk structure and redox capabilities of the samples were investigated with X-ray diffraction and temperature-programmed experiments respectively.

In the first study, the composition of the A-site of the perovskite was investigated. The goal was to design a material with a balance between stability and oxygen vacancy formation capabilities that allowed for a maximized CO production in a recyclable process. Temperature-programmed studies determined that La<sub>0.75</sub>Sr<sub>0.25</sub>CoO<sub>3</sub> exhibited the most stable structure under the reducing environment and the greatest CO production capacity below 850 °C.

Amongst the temperatures tested for isothermal H<sub>2</sub> reduction (400, 500 and 600 °C), and CO<sub>2</sub> conversion (of 650, 750 and 850 °C), 500 and 850 °C were chosen for the reduction and oxidation temperatures respectively in a cycled RWGS-CL experiment. XRD studies after each step of the cycle demonstrated that after the first reduction, the La<sub>0.75</sub>Sr<sub>0.25</sub>CoO<sub>3</sub> perovskite is reduced to the base oxide La<sub>2</sub>O<sub>3</sub>, SrCO<sub>3</sub> and metallic Co. After the first CO<sub>2</sub>-oxidation, the reduced species were incorporated into a layered perovskite structure (La<sub>2-y</sub>Sr<sub>y</sub>CoO<sub>4</sub>). Metallic

Co formed during each reduction was found to be the key agent in the reduction of CO<sub>2</sub> to CO, due to the favored dissociative chemisorption energies of CO<sub>2</sub> on Co. The layered perovskite (La<sub>2-γ</sub>Sr<sub>γ</sub>CoO<sub>4</sub>) acted as a support possibly by keeping the reduced Co particles from aggregating, by enhancing CO<sub>2</sub> adsorption, which is favored in La,Sr-based materials due to their slight basicity.

Incorporation of Fe into the La<sub>0.75</sub>Sr<sub>0.25</sub>CoO<sub>3</sub> proportionally increased the stability of the oxide. The La<sub>0.75</sub>Sr<sub>0.25</sub>FeO<sub>3</sub> perovskite demonstrated capabilities for isothermal H<sub>2</sub>-reduction and CO<sub>2</sub>-reoxidation, therefore it was tested in five consecutive RWGS-CL cycles at 550 °C. The La<sub>0.75</sub>Sr<sub>0.25</sub>FeO<sub>3</sub> was found to have high stability, maintaining the perovskite phase throughout the cycles, as opposed to the La<sub>0.75</sub>Sr<sub>0.25</sub>CoO<sub>3</sub> material. Due to the enhanced stability of the Fe-based perovskite, the H<sub>2</sub> flow did not decomposed the material, rather generated oxygen vacancies that were the driving force for the CO<sub>2</sub> bond cleavage. CO<sub>2</sub> is a poor oxidant and was not able to refill all the vacancies formed during each H<sub>2</sub>-reduction step, therefore, the cumulative amount of oxygen vacancies increased with each cycle. In consequence, the amount of CO produced also increased with cycle. CO production rates from the Fe-based study were comparable to the ones obtained in the Co-based study, even though the latter took place 300 °C higher. Furthermore, the process exhibited very high selectivity towards CO.

Cu was incorporated into the Fe-based perovskite due to its high activity in the conventional RWGS and on photochemical CO<sub>2</sub> reduction. Cu addition increased the reducibility of the Fe-based perovskites and severely decreased CO production. The perovskites with high Cu content underwent a lumped reduction at low temperatures, which likely caused decomposition to multiple phases. The La<sub>0.75</sub>Sr<sub>0.25</sub>FeO<sub>3</sub>, La<sub>0.75</sub>Sr<sub>0.25</sub>Fe<sub>0.9</sub>Cu<sub>0.1</sub>O<sub>3</sub> and La<sub>0.75</sub>Sr<sub>0.25</sub>Fe<sub>0.75</sub>Cu<sub>0.25</sub>O<sub>3</sub> were tested for their ability to convert CO<sub>2</sub> to CO. The perovskites with copper reduced at lower

temperatures but were difficult to re-oxidize with CO<sub>2</sub>. On the other hand, the Fe-perovskite was able to re-oxidize with CO<sub>2</sub>, producing CO as expected. It was found experimentally, and confirmed with DFT, that the materials with very high reducibility were stable in their oxygen vacant state, which reduced the re-oxidation capabilities of the Cu-containing perovskites.

## 7.2 Future Work

Future work should focus on the design and subsequent test of perovskites that can form oxygen vacancies and convert carbon dioxide below 1000 °C and the use of less expensive and scarce metals. Particular attention should be given to oxides that do not require H<sub>2</sub> to make oxygen vacancies, and using metals that have higher earth abundance and lower costs than rare earths and lanthanides.

### 7.2.1 Role of Supports

Mixing a common inexpensive support with the La<sub>0.75</sub>Sr<sub>0.25</sub>FeO<sub>3</sub> perovskite on materials with higher stability could enhance CO production. A physical mixture of an oxide (such as SiO<sub>2</sub>) that does not typically reduce in the temperature range at which the RWGS-CL experiments take place, could prevent aggregation from the perovskite and could potentially enhance the redox properties of the composite by forming extra oxygen vacancies that could also re-oxidize with CO<sub>2</sub>, increasing CO production.

### 7.2.2 Low Temperature Thermochemical Cycles

The natural next step after an isothermal, low temperature RWGS-CL is to decrease the use of H<sub>2</sub>. In thermochemical cycles (TC), high temperatures, instead of hydrogen, are used to make oxygen vacancies in a metal oxide, which is then re-oxidized with CO<sub>2</sub>, producing CO. Materials used in TC include ceria (CeO<sub>2</sub>) [109] and other La- and Sr-based perovskites with manganese, aluminum and chromium on the B site [113, 206], which form oxygen vacancies at



$T > 1000$  °C. However, a computationally driven design of materials can lead to metal oxides with capacity of operating at lower temperatures [184, 185]. Co-based perovskites can form oxygen vacancies at low temperatures, without decomposition as experienced by Cu-based perovskites, while Fe-based perovskites have been shown to convert carbon dioxide at the lowest temperatures. Adding Co and Fe to these metals (Mn, Al and Cr) with higher stability would make a good starting point for low-temperature TC.

### **7.2.3 Earth-Abundant Metals**

Copper, Iron and Cobalt are amongst the metals with highest availability and lower cost. But this is not the case for lanthanum and strontium. These metals were chosen because of two reasons. First, having two different oxidation states ( $\text{La}^{3+}$  and  $\text{Sr}^{2+}$ ), their combination on the A site induces changes in the oxidation state of the metals on the B site, which leads to enhanced redox properties. Second, lanthanide-based oxides are known to be slightly basic; therefore, they have good capacities for adsorption of the slightly acidic carbon dioxide. But an alkaline earth abundant metal, such as calcium, could have potential to be included on the A-site of the perovskite. Calcium has also shown enhanced capabilities for  $\text{CO}_2$  adsorption as  $\text{CaCO}_3$ . But having only  $\text{Ca}^{2+}$  on the A-site would make necessary a combination of metals on the B-site that would create a balance between high stability and enhanced redox capacity.

### **7.2.4 Process Energy Requirements and Potential Economic Outlook**

The preliminary calculations showed on Chapter 6 can be enhanced by including investment, operation and maintenance cost, and energy requirements of the RWGS-CL, FTS and methanol synthesis reactors. Also, within the reactors, modeling of accurate kinetic data, reaction rates and including products selectivity and conversions would also lead to the inclusion of separation units, that would yield more realistic results.

## REFERENCES

- (1) *2014 Key World Energy Statistics*; International Energy Agency, Paris, France, 2014
- (2) *The Global Status of CCS: 2015*; Global C.C.S. Institute, Melbourne, Australia, 2015
- (3) M. Aresta and A. Dibenedetto. Utilization of CO<sub>2</sub> as a chemical feedstock: opportunities and challenges. *Dalton Transactions* **2007**, 2975-2992.
- (4) J. J. Dooley, R. T. Dahowski, and C. L. Davidson. On the Long-Term Average Cost of CO<sub>2</sub> Transport and Storage. *Joint Global Change Research Institute. Pacific Northwest National Laboratory*. **2008**, PNNL-17389,
- (5) R. Angamuthu, P. Byers, M. Lutz, A. L. Spek, and E. Bouwman. Electrocatalytic CO<sub>2</sub> Conversion to Oxalate by a Copper Complex. *Science* **2010**, 327, 313-315.
- (6) S. Sato, T. Arai, T. Morikawa, K. Uemura, T. M. Suzuki, H. Tanaka, and T. Kajino. Selective CO<sub>2</sub> Conversion to Formate Conjugated with H<sub>2</sub>O Oxidation Utilizing Semiconductor/Complex Hybrid Photocatalysts. *Journal of the American Chemical Society* **2011**, 133, 15240-15243.
- (7) G. A. Olah, A. Goeppert, and G. K. S. Prakash. Chemical Recycling of Carbon Dioxide to Methanol and DIMethyl Eter: From Greenhouse Gas to Renewable, Environmentally Carbon Neutral Fuels and Synthetic Hydrocarbons. *The Journal of Organic Chemistry* **2009**, 74, 487-498.
- (8) A. Goeppert, M. Czaun, J.-P. Jones, G. K. Surya Prakash, and G. A. Olah. Recycling of carbon dioxide to methanol and derived products - closing the loop. *Chemical Society Reviews* **2014**, 43, 7995-8048.
- (9) G. Job, S. D. Allen, C. Simoneau, R. Valente, and J. J. Farmer, "Metal complexes," USA Patent, 2015.
- (10) P. M. Mortensen and I. Dybkjær. Industrial scale experience on steam reforming of CO<sub>2</sub>-rich gas. *Applied Catalysis A: General* **2015**, 495, 141-151.
- (11) P. Kaiser, R. B. Unde, C. Kern, and A. Jess. Production of Liquid Hydrocarbons with CO<sub>2</sub> as Carbon Source based on Reverse Water-Gas Shift and Fischer-Tropsch Synthesis. *Chemie Ingenieur Technik* **2013**, 85, 489-499.
- (12) *Demonstrating CO<sub>2</sub> capture in the UK cement, chemicals, iron and steel and oil refining sectors by 2025: A Techno-economic Study*; Department for Business, Innovation & Skills (BIS) and Department of Energy & Climate Change (DECC), Cambridge CB1 2JD, 2014
- (13) X. Xiaoding and J. A. Moulijn. Mitigation of CO<sub>2</sub> by Chemical Conversion: Plausible Chemical Reactions and Promising Products. *Energy & Fuels* **1996**, 10, 305-325.
- (14) M. B. Ansari and S.-E. Park. Carbon dioxide utilization as a soft oxidant and promoter in catalysis. *Energy & Environmental Science* **2012**, 5, 9419-9437.
- (15) M. Poliakoff, W. Leitner, and E. S. Streng. The Twelve Principles of CO<sub>2</sub> CHEMISTRY. *Faraday Discussions* **2015**, 183, 9-17.

- (16) G. Centi and S. Perathoner. Opportunities and prospects in the chemical recycling of carbon dioxide to fuels. *Catalysis Today* **2009**, *148*, 191-205.
- (17) S. Chunshan; 1. In *CO<sub>2</sub> Conversion and Utilization* ACS Symposium Series; American Chemical Society: 2002, pp. 2-30.
- (18) T. Riedel, M. Claeys, H. Schulz, G. Schaub, S.-S. Nam, K.-W. Jun, M.-J. Choi, G. Kishan, and K.-W. Lee. Comparative study of Fischer–Tropsch synthesis with H<sub>2</sub>/CO and H<sub>2</sub>/CO<sub>2</sub> syngas using Fe- and Co-based catalysts. *Applied Catalysis A: General* **1999**, *186*, 201-213.
- (19) G. Centi, S. Perathoner, and G. Iaquaniello; 2. In *CO<sub>2</sub>: A Valuable Source of Carbon*. vol., M. De Falco, G. Iaquaniello, and G. Centi; Green Energy and Technology; Springer London: 2013, pp. 27-43.
- (20) S. Chu and A. Majumdar. Opportunities and challenges for a sustainable energy future. *Nature* **2012**, *488*, 294-303.
- (21) H. S. Chung, C. S. H. Chen, R. A. Kremer, and J. R. Boulton. Recent Developments in High-Energy Density Liquid Hydrocarbon Fuels. *Energy & Fuels* **1999**, *13*, 641-649.
- (22) C. Song. Global challenges and strategies for control, conversion and utilization of CO<sub>2</sub> for sustainable development involving energy, catalysis, adsorption and chemical processing. *Catalysis Today* **2006**, *115*, 2-32.
- (23) O.-S. Joo, K.-D. Jung, I. Moon, A. Y. Rozovskii, G. I. Lin, S.-H. Han, and S.-J. Uhm. Carbon Dioxide Hydrogenation To Form Methanol via a Reverse-Water-Gas-Shift Reaction (the CAMERE Process). *Industrial & Engineering Chemistry Research* **1999**, *38*, 1808-1812.
- (24) N. Meiri, Y. Dinburg, M. Amoyal, V. Koukouliev, R. V. Nehemya, M. V. Landau, and M. Herskowitz. Novel process and catalytic materials for converting CO<sub>2</sub> and H<sub>2</sub> containing mixtures to liquid fuels and chemicals. *Faraday Discussions* **2015**, *183*, 197-215.
- (25) K. Oshima, T. Shinagawa, Y. Nogami, R. Manabe, S. Ogo, and Y. Sekine. Low temperature catalytic reverse water gas shift reaction assisted by an electric field. *Catalysis Today* **2014**, *232*, 27-32.
- (26) W. Wang, S. Wang, X. Ma, and J. Gong. Recent advances in catalytic hydrogenation of carbon dioxide. *Chemical Society Reviews* **2011**, *40*, 3703-3727.
- (27) E. V. Kondratenko, G. Mul, J. Baltrusaitis, G. O. Larrazábal, and J. Pérez-Ramírez. Status and perspectives of CO<sub>2</sub> conversion into fuels and chemicals by catalytic, photocatalytic and electrocatalytic processes. *Energy & Environmental Science* **2013**, *6*, 3112-3135.
- (28) A. Taheri, E. J. Thompson, J. C. Fettinger, and L. A. Berben. An Iron Electrocatalyst for Selective Reduction of CO<sub>2</sub> to Formate in Water: Including Thermochemical Insights. *ACS Catalysis* **2015**, *5*, 7140-7151.
- (29) M. D. Porosoff, B. Yan, and J. G. Chen. Catalytic reduction of CO<sub>2</sub> by H<sub>2</sub> for synthesis of CO, methanol and hydrocarbons: challenges and opportunities. *Energy & Environmental Science* **2016**, *9*, 62-73.
- (30) N. H. Elsayed, N. R. M. Roberts, B. Joseph, and J. N. Kuhn. Low temperature dry reforming of methane over Pt–Ni–Mg/ceria–zirconia catalysts. *Applied Catalysis B: Environmental* **2015**, *179*, 213-219.

- (31) J. Skrzypek, M. Lachowska, and D. Serafin. Methanol synthesis from CO<sub>2</sub> and H<sub>2</sub>: dependence of equilibrium conversions and exit equilibrium concentrations of components on the main process variables. *Chemical Engineering Science* **1990**, *45*, 89-96.
- (32) K.-H. Ernst, C. T. Campbell, and G. Moretti. Kinetics of the Reverse Water-Gas Shift Reaction over Cu(110). *Journal of Catalysis* **1992**, *134*, 66-74.
- (33) M. J. L. Ginés, A. J. Marchi, and C. R. Apesteguía. Kinetic study of the reverse water-gas shift reaction over CuO/ZnO/Al<sub>2</sub>O<sub>3</sub> catalysts. *Applied Catalysis A: General* **1997**, *154*, 155-171.
- (34) C.-S. Chen, W.-H. Cheng, and S.-S. Lin. Study of iron-promoted Cu/SiO<sub>2</sub> catalyst on high temperature reverse water gas shift reaction. *Applied Catalysis A: General* **2004**, *257*, 97-106.
- (35) C.-S. Chen, J. H. Lin, J. H. You, and C. R. Chen. Properties of Cu(thd)<sub>2</sub> as a Precursor to Prepare Cu/SiO<sub>2</sub> Catalyst Using the Atomic Layer Epitaxy Technique. *Journal of the American Chemical Society* **2006**, *128*, 15950-15951.
- (36) W. Wang, Y. Zhang, Z. Wang, J.-M. Yan, Q. Ge, and C.-J. Liu. Reverse water gas shift over In<sub>2</sub>O<sub>3</sub>-CeO<sub>2</sub> catalysts. *Catalysis Today* **2016**, *259*, 402-408.
- (37) B. Zhao, Y.-X. Pan, and C.-J. Liu. The promotion effect of CeO<sub>2</sub> on CO<sub>2</sub> adsorption and hydrogenation over Ga<sub>2</sub>O<sub>3</sub>. *Catalysis Today* **2012**, *194*, 60-64.
- (38) L. Wang, H. Liu, Y. Liu, Y. Chen, and S. Yang. Effect of precipitants on Ni-CeO<sub>2</sub> catalysts prepared by a co-precipitation method for the reverse water-gas shift reaction. *Journal of Rare Earths* **2013**, *31*, 969-974.
- (39) P. Panagiotopoulou, D. I. Kondarides, and X. E. Verykios. Mechanistic aspects of the selective methanation of CO over Ru/TiO<sub>2</sub> catalyst. *Catalysis Today* **2012**, *181*, 138-147.
- (40) K.-W. Jun, H.-S. Roh, K.-S. Kim, J.-S. Ryu, and K.-W. Lee. Catalytic investigation for Fischer-Tropsch synthesis from bio-mass derived syngas. *Applied Catalysis A: General* **2004**, *259*, 221-226.
- (41) C. Bosch and W. Wild, "Producing hydrogen," 1914.
- (42) D. S. Mallapragada, N. R. Singh, V. Curteanu, and R. Agrawal. Sun-to-Fuel Assessment of Routes for Fixing CO<sub>2</sub> as Liquid Fuel. *Industrial & Engineering Chemistry Research* **2013**, *52*, 5136-5144.
- (43) J. E. Whitlow and C. F. Parrish. Operation, Modeling and Analysis of the Reverse Water Gas Shift Process. *AIP Conference Proceedings* **2003**, *654*, 1116-1123.
- (44) D. P. VanderWiel, J. L. Zilka, Y. Wang, A. Y. Tonkovich, and R. S. Wegeng, "Carbon Dioxide Conversions in Microreactors," presented at the IMRET 4: Proceedings of the 4th International Conference on Microreaction Technology, Topical Conference Proceedings, AIChE Spring National Meeting; American Institute of Chemical Engineers, Atlanta, GA, 2000.
- (45) Y. A. Daza, R. A. Kent, M. M. Yung, and J. N. Kuhn. Carbon dioxide conversion by reverse water gas shift chemical looping on perovskite-type oxides. *Industrial & Engineering Chemistry Research* **2014**, *53*, 5828-5837.
- (46) Y. A. Daza, D. Maiti, R. A. Kent, V. R. Bhethanabotla, and J. N. Kuhn. Isothermal reverse water gas shift chemical looping on La<sub>0.75</sub>Sr<sub>0.25</sub>Co<sub>(1-Y)</sub>Fe<sub>Y</sub>O<sub>3</sub> perovskite type oxides. *Catalysis Today* **2015**, *258*, 691-698.

- (47) Y. A. Daza, D. Maiti, B. J. Hare, V. R. Bhethanabotla, and J. N. Kuhn. More Cu, more problems: Decreased CO<sub>2</sub> conversion ability by Cu-doped La<sub>0.75</sub>Sr<sub>0.25</sub>FeO<sub>3</sub> perovskite oxides. *Surface Science* **2016**, *648*, 92-99.
- (48) M. Najera, R. Solunke, T. Gardner, and G. Vesper. Carbon capture and utilization via chemical looping dry reforming. *Chemical Engineering Research and Design* **2011**, *89*, 1533-1543.
- (49) R. D. Solunke and G. Vesper. Hydrogen Production via Chemical Looping Steam Reforming in a Periodically Operated Fixed-Bed Reactor. *Industrial & Engineering Chemistry Research* **2010**, *49*, 11037-11044.
- (50) V. V. Galvita, H. Poelman, V. Bliznuk, C. Detavernier, and G. B. Marin. CeO<sub>2</sub>-Modified Fe<sub>2</sub>O<sub>3</sub> for CO<sub>2</sub> Utilization via Chemical Looping. *Industrial & Engineering Chemistry Research* **2013**, *52*, 8416-8426.
- (51) C. Nordhei, K. Mathisen, I. Bezverkhyy, and D. G. Nicholson. Decomposition of carbon dioxide over the putative cubic spinel nanophase cobalt, nickel and zinc ferrites. *Journal of Physical Chemistry* **2008**, *112*, 6531-6537.
- (52) C. Nordhei, K. Mathisen, O. Safonova, W. van Beek, and D. G. Nicholson. Decomposition of carbon dioxide at 500°C over reduced iron, cobalt, nickel and zinc ferrites: a combined XANES-XRD study. *Journal of Physical Chemistry* **2009**, *113*, 19568-19577.
- (53) D. Maiti, Y. A. Daza, M. M. Yung, J. N. Kuhn, and V. R. Bhethanabotla. Oxygen vacancy formation characteristics in the bulk and across different surface terminations of La<sub>(1-x)</sub>Sr<sub>x</sub>Fe<sub>(1-y)</sub>Co<sub>y</sub>O<sub>(3-δ)</sub> perovskite oxides for CO<sub>2</sub> conversion. *Submitted* **2015**,
- (54) R. K. C. de Lima, M. S. Batista, M. Wallau, E. A. Sanches, Y. P. Mascarenhas, and E. A. Urquieta-González. High specific surface area LaFeCo perovskites—Synthesis by nanocasting and catalytic behavior in the reduction of NO with CO. *Applied Catalysis B: Environmental* **2009**, *90*, 441-450.
- (55) T. Ishihara; Structure and Properties of Perovskite Oxides. In *Perovskite Oxide for Solid Oxide Fuel Cells*. vol., N. P. Bansal; Fuel Cells and Hydrogen Energy; Springer: U.S., 2009, pp. 1-16.
- (56) M. A. Peña and J. L. G. Fierro. Chemical Structures and Performance of Perovskite Oxides. *Chemical Reviews* **2001**, *101*, 1981-2017.
- (57) C. H. Kim, G. Qi, K. Dahlberg, and W. Li. Strontium-Doped Perovskites Rival Platinum Catalysts for Treating NO<sub>x</sub> in Simulated Diesel Exhaust. *Science* **2010**, *327*, 1624-1627.
- (58) N. Yamazoe, Y. Teraoka, and T. Seiyama. TPD and XPS Study on Thermal Behavior of Absorbed Oxygen in La<sub>1-x</sub>Sr<sub>x</sub>CoO<sub>3</sub>. *Chemistry Letters* **1981**, *11*, 1767-1770.
- (59) K. Huang, H. Y. Lee, and J. B. Goodenough. Sr- and Ni- Doped LaCoO<sub>3</sub> and LaFeO<sub>3</sub> Perovskites: New Cathode Materials for Solid-Oxide Fuel Cells. *Journal of the Electrochemistry Society* **1998**, *145*, 3220.
- (60) Y.-H. Huang, R. I. Dass, Z.-L. Xing, and J. B. Goodenough. Double Perovskites as Anode Materials for Solid-Oxide Fuel Cells. *Science* **2006**, *312*, 254.
- (61) L. Marchetti and L. Forni. Catalytic combustion of methane over perovskites. *Applied Catalysis B: Environmental* **1998**, *15*, 179.
- (62) L. Forni and I. Rossetti. Catalytic combustion of hydrocarbons over perovskites. *Applied Catalysis B: Environmental* **2002**, *38*, 29.
- (63) D. Fino, N. Russo, G. Saracco, and V. Specchia. The role of suprafacial oxygen in some perovskites for the catalytic combustion of soot. *Journal of Catalysis* **2003**, *217*, 367-375.

- (64) X. Yang, L. Luo, and H. Zhong. Catalytic properties of LnSrCoO<sub>4</sub> (Ln=La, Sm) in the oxidation of CO and C<sub>3</sub>H<sub>8</sub>. *React. Kinet. Catal. Lett.* **2004**, *81*, 219-227.
- (65) D. Klvana, J. Kirchnerová, and C. Tofan. Catalytic Decomposition of Nitric Oxide by Perovskites. *Korean Journal of Chemical Engineering* **1999**, *16*, 470-477.
- (66) J. Zhu, X. Yang, X. Xu, and K. Wei. Active Site Structure of NO Decomposition on Perovskite(-like) Oxides: An Investigation from Experiment and Density Functional Theory. *Journal of Physical Chemistry C* **2007**, *111*, 1487-1490.
- (67) D. Ferri, L. Forni, M. A. P. Dekkers, and B. E. Nieuwenhuys. NO reduction by H<sub>2</sub> over perovskite-like mixed oxides. *Applied Catalysis B: Environmental* **1998**, *16*, 339-345.
- (68) B. V. Beznosikov and K. S. Aleksandrov. Perovskite-like crystals of the Ruddlesden-Popper series. *Crystallography Reports* **2000**, *45*, 792-798.
- (69) S. N. Ruddlesden and P. Popper. New compounds of the K<sub>2</sub>NiF<sub>4</sub> type. *Acta Crystallographica* **1957**, *10*, 538-539.
- (70) X. L. Wang, H. Sakurai, and E. Takayama-Muromachi. Synthesis, structures, and magnetic properties of novel Ruddlesden-Popper homologous series Sr<sub>n+1</sub>Co<sub>n</sub>O<sub>3n+1</sub> (n=1,2,3,4, and ∞). *Journal of Applied Physics* **2005**, *97*, 10M519:1-3.
- (71) C. Tealdi, C. Ferrara, L. Malavasi, P. Mustarelli, C. Ritter, A. Spinella, D. Massiot, and P. Florian. Average versus local structure in K<sub>2</sub>NiF<sub>4</sub>-type LaSrAlO<sub>4</sub>: direct experimental evidence of local cationic ordering. *Journal of Materials Chemistry* **2012**, *22*, 10488-10495.
- (72) Q. Yang and J. Y. S. Lin. Fixed-bed performance for production of oxygen-enriched carbon dioxide stream by perovskite-type ceramic sorbent. *Separation and Purification Technology* **2006**, *49*, 27-35.
- (73) Q. Yin, J. Kniep, and Y. S. Lin. Oxygen sorption and desorption properties of Sr-Co-Fe oxide. *Chemical Engineering Science* **2008**, *63*, 2011-2218.
- (74) J. E. ten Elshof, H. J. M. Bouwmeester, and H. Verweij. Oxygen transport through La<sub>1-x</sub>Sr<sub>x</sub>FeO<sub>3-d</sub> membranes II. Permeation in air/CO, CO<sub>2</sub> gradients. *Solid State Ionics* **1996**, *89*, 81-92.
- (75) M. Radovic, S. A. Speakman, L. F. Allard, E. A. Payzant, E. Lara-Curzio, W. M. Kriven, J. Lloyd, L. Fegely, and N. Orlovskay. Thermal, mechanical and phase stability of LaCoO<sub>3</sub> in reducing and oxidizing environments. *Journal of Power Sources* **2008**, *184*, 77-83.
- (76) Z. H. Yang and Y. S. Lin. Synergetic thermal effects for oxygen sorption and order-disorder transition on perovskite-type oxides. *Solid State Ionics* **2005**, *176*, 89.
- (77) T. Arakawa, N. Ohara, and J. Shiokawa. *Journal of Materials Science* **1986**, *21*, 1824-1827.
- (78) S. Ivanova, A. Senysshyn, E. Zhecheva, K. Tenchev, V. Nikolov, R. Stoyanova, and H. Fuess. Effect of the synthesis route on the microstructure and the reducibility of LaCoO<sub>3</sub>. *Journal of Alloys and Compounds* **2009**, *480*, 279-285.
- (79) V. Fruth, M. Popa, J. Calderon-Moreno, E. Tenea, M. Anastasescu, P. Osiceanu, E. Anghel, L. Predoana, B. Malic, and M. Zaharescu. Perovskite type nanopowders and thin films obtained by chemical methods. *Processing and Application of Ceramics* **2010**, *4*, 167-182.
- (80) J. G. Bednorz and K. A. Müller; In *Ten Years of Superconductivity: 1980–1990*. vol., H. R. Ott; Springer Netherlands: Dordrecht, 1993, pp. 267-271.

- (81) R. J. Cava, B. Batlogg, R. B. van Dover, D. W. Murphy, S. Sunshine, T. Siegrist, J. P. Remeika, E. A. Rietman, S. Zahurak, and G. P. Espinosa. Bulk superconductivity at 91 K in single-phase oxygen-deficient perovskite  $\text{Ba}_2\text{YCu}_3\text{O}_{9-\delta}$ . *Physical Review Letters* **1987**, 58, 1676-1679.
- (82) U. Shimony and J. M. Knudsen. Mössbauer Studies on Iron in the Perovskites  $\text{La}_{1-x}\text{Sr}_x\text{FeO}_3$  ( $0.0 < x < 1.0$ ). *Physical Review* **1966**, 144, 361-366.
- (83) O. Haas, R. P. W. J. Struis, and J. M. McBreen. Synchrotron X-ray absorption of  $\text{LaCoO}_3$  perovskite. *Journal of Solid State Chemistry* **2004**,
- (84) L. G. Tejuca and J. L. G. Fierro. XPS and TPD probe techniques for the study of  $\text{LaNiO}_3$  perovskite oxide. *Thermochimica Acta* **1989**, 147, 361-375.
- (85) S. Royer, D. Duprez, and S. Kaliaguine. Role of bulk and grain boundary oxygen mobility in the catalytic oxidation activity of  $\text{LaCo}_{1-x}\text{Fe}_x\text{O}_3$ . *Journal of Catalysis* **2005**, 234, 364-375.
- (86) A. Ringuedé and J. Fouletier. Oxygen reaction on strontium-doped lanthanum cobaltite dense electrodes at intermediate temperatures. *Solid State Ionics* **2001**, 139, 167-177.
- (87) N. Yamazoe, S. Furukawa, Y. Teraoka, and T. Seiyama. The effect of oxygen sorption on the crystal structure of  $\text{La}_{1-x}\text{Sr}_x\text{CoO}_{3-\delta}$ . *Chemistry Letters* **1982**, 10, 2019-2022.
- (88) J. N. Kuhn and U. S. Ozkan. Effect of Co Content Upon the Bulk Structure of Sr- and Co-doped  $\text{LaFeO}_3$ . *Catalysis Letters* **2008**, 121, 179-188.
- (89) J. N. Kuhn, P. H. Matter, J.-M. M. Millet, R. B. Watson, and U. S. Ozkan. Oxygen Exchange Kinetics over Sr- and Co-Doped  $\text{LaFeO}_3$ . *Journal of Physical Chemistry C* **2008**, 112, 12468-12476.
- (90) M. L. Rojas, J. L. G. Fierro, L. G. Tejuca, and A. T. Bell. Preparation and characterization of  $\text{LaMn}_{1-x}\text{Cu}_x\text{O}_{3+\lambda}$  perovskite oxides. *Journal of Catalysis* **1990**, 124, 41-51.
- (91) L. G. Tejuca and J. L. G. Fierro, Eds., *Properties and applications of perovskite-type oxides*. New York: Marcel Dekker, Inc., 1993, p. pp. Pages.
- (92) B. Meredig and C. Wolverton. First-principles thermodynamic framework for the evaluation of thermochemical  $\text{H}_2\text{O}$ - or  $\text{CO}_2$ -splitting materials. *Physical Review B* **2009**, 80, 245119:1-8.
- (93) J. E. Miller, A. H. McDaniel, and M. D. Allendorf. Considerations in the Design of Materials for Solar-Driven Fuel Production Using Metal-Oxide Thermochemical Cycles. *Advanced Energy Materials* **2014**, 4, 1300469:1-19.
- (94) J. Mizusaki, M. Yoshihiro, S. Yamauchi, and K. Fueki. Thermodynamic quantities and defect equilibrium in the perovskite-type oxide solid solution  $\text{La}_{1-x}\text{Sr}_x\text{FeO}_{3-\delta}$ . *Journal of Solid State Chemistry* **1987**, 67, 1-8.
- (95) M. S. G. Baythoun and F. R. Sale. Production of strontium-substituted lanthanum manganite perovskite powder by the amorphous citrate process. *Journal of Material Science* **1982**, 17, 2757-2769.
- (96) J. Kirchnerová, D. Klvana, and J. Chaouki. Evaluation of some cobalt and nickel based perovskites prepared by freeze-drying as combustion catalysts. *Catalysis Letters* **1993**, 21, 77-87.
- (97) M. Popa and M. Kakihana. Synthesis of lanthanum cobaltite ( $\text{LaCoO}_3$ ) by the polymerizable complex route. *Solid State Ionics* **2002**, 151, 251-257.
- (98) G. H. Annal, M. Dinamani, and V. Kamath. Electrochemical synthesis of perovskite oxides. *Journal of Applied Electrochemistry* **2005**, 35, 459-465.

- (99) Z. Shao, G. Xiong, Y. Ren, and Y. Cong. Low temperature synthesis of perovskite oxide using the adsorption properties of cellulose. *Journal of Materials Science* **2000**, *35*, 5639-5644.
- (100) A. Civera, M. Pavese, G. Saracco, and V. Specchia. Combustion synthesis of perovskite-type catalysts for natural gas combustion. *Catalysis Today* **2003**, *83*, 199-211.
- (101) J. A. Schwartz. Methods for Preparation of Catalytic Materials. *Chemical Reviews* **1995**, *95*, 477-510.
- (102) S. Brunauer, P. H. Emmett, and E. Teller. Adsorption of Gases in Multimolecular Layers. *Journal of the American Chemical Society* **1938**, *60*, 309-319.
- (103) B. D. Cullity. *Elements of X-ray Diffraction*: Addison-Wesley Publishing Company, 1956.
- (104) L. G. Wade. *Organic Chemistry*. Madrid, Spain: Prentice Hall PTR, 2004.
- (105) *2013 Key World Energy Statistics*; International Energy Agency, Paris, France, 2013
- (106) *The global status of CCS:2013*; Global Carbon Capture and Storage Institute, Melbourne, Australia, 2013
- (107) G. Centi, E. A. Quadrelli, and S. Perathoner. Catalysis for CO<sub>2</sub> conversion: a key technology for rapid introduction of renewable energy in the value chain of chemical industries. *Energy & Environmental Science* **2013**, *6*, 1711-1731.
- (108) G. A. Olah. The role of catalysis in replacing oil by renewable methanol using carbon dioxide capture and recycling (CCR). *Catalysis Letters* **2013**, *143*, 983-987.
- (109) W. C. Chueh, C. Falter, M. Abbott, D. Scipio, P. Furler, S. M. Haile, and A. Steinfeld. High-Flux Solar-Driven Thermochemical Dissociation of CO<sub>2</sub> and H<sub>2</sub>O Using Nonstoichiometric Ceria. *Science* **2010**, *330*, 1797-1801.
- (110) J. R. Scheffe, D. Weibel, and A. Steinfeld. Lanthanum-Strontium-Manganese Perovskites as Redox Materials for Solar Thermochemical Splitting of H<sub>2</sub>O and CO<sub>2</sub>. *Energy & Fuels* **2013**, *27*, 4250-4257.
- (111) P. Furler, J. R. Scheffe, M. Gorbar, L. Moes, U. Vogt, and A. Steinfeld. Solar thermochemical CO<sub>2</sub> splitting utilizing a reticulated porous ceria redox system. *Energy & Fuels* **2012**, *26*, 7051-7059.
- (112) A. Le Gal, S. Abanades, and G. Flamant. CO<sub>2</sub> and H<sub>2</sub>O splitting for thermochemical production of solar fuels using nonstoichiometric ceria and ceria/zirconia solid solutions. *Energy & Fuels* **2011**, *25*, 4836-4845.
- (113) A. H. McDaniel, E. C. Miller, D. Arifin, A. Ambrosini, E. N. Coker, R. O'Hayre, W. C. Chueh, and J. Tong. Sr- and Mn-doped LaAlO<sub>3-σ</sub> for solar thermochemical H<sub>2</sub> and CO production. *Energy & Environmental Science* **2013**, *6*, 2024-2028.
- (114) J. E. Miller, M. D. Allendorf, R. B. Diver, L. R. Evans, N. P. Siegel, and J. N. Stuecker. Metal oxide composites and structures for ultra-high temperature solar thermochemical cycles. *Journal of Materials Science* **2008**, *43*, 4714-4728.
- (115) J. Kim, C. A. Henao, T. A. Johnson, D. E. Dedrick, J. E. Miller, E. B. Stechel, and C. T. Maravelias. Methanol production from CO<sub>2</sub> using solar-thermal energy: process development and techno-economic analysis. *Energy & Environmental Science* **2011**, *4*, 3122-3132.
- (116) Q. Zhai, S. Xie, W. Fan, Q. Zhang, Y. Wang, W. Deng, and Y. Wang. Photocatalytic conversion of carbon dioxide with water into methane: platinum and copper(I) oxide co-catalyst with a core-shell structure. *Angewandte Chemie International Edition* **2013**, *52*, 5776-5779.



- (117) H. Zhou, J. Guo, P. Li, T. Fan, D. Zhang, and J. Ye. Leaf-architected 3-D hierarchical artificial photosynthetic system of perovskite titanates towards CO<sub>2</sub> photoreduction into hydrocarbon fuels. *Scientific Reports* **2013**, *3*, 1667:1-9.
- (118) C. Wang, O. Ranasingha, S. Natesakhawat, P. R. Ohodnicki, M. Andio, J. P. Lewis, and C. Matranga. Visible light plasmonic heating of Au-ZnO for the catalytic reduction of CO<sub>2</sub>. *Nanoscale* **2013**, *5*, 6968-6974.
- (119) J. Kim, T. A. Johnson, J. E. Miller, E. B. Stechel, and C. T. Maravelias. Fuel production from CO<sub>2</sub> using solar-thermal energy: system level analysis. *Energy & Environmental Science* **2012**, *5*, 8417-8429.
- (120) J. E. Readman, A. Olafsen, Y. Larring, and R. Blom. La<sub>0.8</sub>Sr<sub>0.2</sub>Co<sub>0.2</sub>Fe<sub>0.8</sub>O<sub>3-δ</sub> as a potential oxygen carrier in a chemical looping type reactor, an in-situ powder X-ray diffraction study. *Journal of Materials Chemistry* **2005**, *15*, 1931-1937.
- (121) A. V. Murugan, A. Thursfield, and I. S. Metcalfe. A chemical looping process for hydrogen production using iron-containing perovskites. *Energy & Environmental Science* **2011**, *4*, 4639-4649.
- (122) Z. Sarshar, F. Kleitz, and S. Kaliaguine. Novel oxygen carriers for chemical looping combustion: La<sub>1-x</sub>Ce<sub>x</sub>BO<sub>3</sub> (B = Co, Mn) perovskites synthesized by reactive grinding and nanocasting. *Energy & Environmental Science* **2011**, *4*, 4258-4269.
- (123) S. Bhavsar, M. Najera, and G. Vesper. Chemical Looping Dry Reforming as Novel, Intensified Process for CO<sub>2</sub> Activation. *Chemical Engineering & Technology* **2012**, *35*, 1281-1290.
- (124) S. Hokenek and J. N. Kuhn. Methanol Decomposition over Palladium Particles Supported on Silica: Role of Particle Size and Co-Feeding Carbon Dioxide on the Catalytic Properties. *ACS Catalysis* **2012**, *2*, 1013-1019.
- (125) V. A. Castillo and J. N. Kuhn. Role of the Ni:Fe Ratio in Ethylene Hydrogenation Activity for Silica-Supported Ni-Fe Clusters Prepared by Dendrimer-Templating. *Journal of Physical Chemistry C* **2012**, *116*, 8627-8633.
- (126) T. Nakamura, M. Misono, and N. Yoneda. Catalytic properties of perovskite-type mixed oxides, La<sub>1-x</sub>Sr<sub>x</sub>CoO<sub>3</sub>. *Bulletin of the Chemical Society of Japan* **1982**, *55*, 394-399.
- (127) A. N. Petrov, O. F. Kononchuk, A. V. Andreev, V. A. Cerepanov, and P. Kofstad. Crystal structure, electrical and magnetic properties of La<sub>1-x</sub>Sr<sub>x</sub>Co<sub>3-y</sub>. *Solid State Ionics* **1995**, *80*, 189-199.
- (128) T. V. Aksenova, M. V. Anan'ev, L. Y. Gavrilova, and V. A. Cherepanov. Phase equilibria and crystal structures of solid solutions in the system LaCoO<sub>3-δ</sub>-SrCoO<sub>2.5±δ</sub>-SrFeO<sub>3-δ</sub>-LaFeO<sub>3-δ</sub>. *Inorganic Materials* **2007**, *43*, 296-300.
- (129) P. Zeng, R. Ran, Z. Chen, W. Zhou, H. Gu, Z. Shao, and S. Liu. Efficient stabilization of cubic perovskite SrCoO<sub>3-δ</sub> by B-site low concentration scandium doping combined with sol-gel synthesis. *Journal of Alloys and Compounds* **2008**, *455*, 465-470.
- (130) L. Predoana, B. Malic, M. Kosec, M. Carata, M. Caldararu, and M. Zaharescu. Characterization of LaCoO<sub>3</sub> powders obtained by water-based sol-gel method with citric acid. *Journal of the European Ceramic Society* **2007**, *27*, 4407-4411.
- (131) S. Rousseau, S. Loridant, P. Delichere, A. Boreave, J. P. Deloune, and P. Vernoux. La<sub>(1-x)</sub>Sr<sub>x</sub>Co<sub>1-y</sub>Fe<sub>y</sub>O<sub>3</sub> perovskites prepared by sol-gel method: Characterization and relationships with catalytic properties for total oxidation of toluene. *Applied Catalysis B: Environmental* **2009**, *88*, 438-447.

- (132) J. Mizusaki, Y. Mima, S. Yamauchi, K. Fueki, and H. Tagawa. Nonstoichiometry of the Perovskite-Type Oxides  $\text{La}_{1-x}\text{Sr}_x\text{CoO}_{3-\delta}$ . *Journal of Solid State Chemistry* **1989**, 80, 102-111.
- (133) T. Nakamura, M. Misono, and Y. Yoneda. Reduction-oxidation and catalytic properties of  $\text{La}_{1-x}\text{Sr}_x\text{CoO}_3$ . *Journal of Catalysis* **1983**, 83, 151-159.
- (134) X. L. Wang and E. Takayama-Muromachi. Magnetic and transport properties of the layered perovskite system  $\text{Sr}_{2-y}\text{Y}_y\text{O}_4$  ( $0 \leq y \leq 1$ ). *Physical Review B* **2005**, 72, 064401:1-7.
- (135) J. Matsuno, Y. Okimoto, Z. Fang, X. Z. Yu, Y. Matsui, N. Nagaosa, M. Kawasaki, and Y. Tokura. Metallic Ferromagnet with Square-Lattice  $\text{CoO}_2$  Sheets. *Physical Review Letters* **2004**, 93, 167202:1-4.
- (136) L. G. Tejuca, C. H. Rochester, J. L. G. Fierro, and J. M. D. Tascón. Infrared spectroscopic study of the adsorption of pyridine, carbon monoxide and carbon dioxide on the perovskite-type oxides  $\text{LaMO}_3$ . *Journal of the Chemical Society, Faraday Transactions 1: Physical Chemistry in Condensed Phases* **1984**, 80, 1089-1099.
- (137) T. Bligaard, J. K. Nørskov, S. Dahl, J. Matthiesen, C. H. Christensen, and J. Sehested. The Brønsted–Evans–Polanyi relation and the volcano curve in heterogeneous catalysis. *Journal of Catalysis* **2004**, 224, 206-217.
- (138) D. Brennan and D. O. Hayward. The adsorption of carbon dioxide on evaporated metal films. *Philosophical Transactions of the Royal Society A* **1965**, 258, 375-386.
- (139) J. A. Turner. Sustainable Hydrogen Production. *Science* **2004**, 305, 972-974.
- (140) I. Omae. Aspects of carbon dioxide utilization. *Catalysis Today* **2006**, 115, 33-52.
- (141) C.-S. Chen, W.-H. Cheng, and S.-S. Lin. Mechanism of CO formation in reverse water-gas shift reaction over  $\text{Cu}/\text{Al}_2\text{O}_3$  catalyst. *Catalysis Letters* **2000**, 68, 45-48.
- (142) D. J. Pettigrew, D. L. Trimm, and N. W. Cant. The effects of rare earth oxides on the reverse water-gas shift reaction on palladium/alumina. *Catalysis Letters* **1994**, 28, 313-319.
- (143) A. Goguet, F. Meunier, J. P. Breen, R. Burch, M. I. Petch, and A. F. Ghenciu. Study of the origin of the deactivation of a  $\text{Pt}/\text{CeO}_2$  catalyst during reverse water gas shift (RWGS) reaction. *Journal of Catalysis* **2004**, 226, 382-392.
- (144) E. P. Agency. (2014, October 6 2014). *Regulations & Standards*. Available: <http://www.epa.gov/nsr/actions.html> - 2010
- (145) G. C. C. S. Institute. (2013, January 29 2013). *Large Scale Integrated CCS Projects*. Available: <http://www.globalccsinstitute.com/data/status-ccs-project-database>
- (146) A. Abad, T. Mattison, A. Lyngfelt, and M. Johansson. The use of iron oxide as oxygen carrier in a chemical-looping reactor. *Fuel* **2007**, 86, 1021-1035.
- (147) S. Bhavsar and G. Vesper. Bimetallic Fe-Ni Oxygen Carriers for Chemical Looping Combustion. *Industrial & Engineering Chemistry Research* **2013**, 52, 15342-15352.
- (148) S. Bhavsar, M. Najera, R. Solunke, and G. Vesper. Chemical looping: To combustion and beyond. *Catalysis Today* **2014**, 228, 96-105.
- (149) J. N. Kuhn and U. S. Ozkan. Surface properties of Sr- and Co-doped  $\text{LaFeO}_3$ . *Journal of Catalysis* **2008**, 253, 200-211.
- (150) A. A. Leontiou, A. K. Ladavos, T. V. Bakas, T. C. Vaimakis, and P. J. Pomonis. Reverse uptake of oxygen from  $\text{La}_{1-x}\text{Sr}_x(\text{Fe}^{3+}/\text{Fe}^{4+})\text{O}_{3+\delta}$  perovskite-type mixed oxides ( $x = 0.00, 0.15, 0.30, 0.40, 0.60, 0.70, 0.80, 0.90$ ). *Applied Catalysis A: General* **2003**, 241, 143-154.

- (151) M. M. Natile, F. Poletto, A. Galenda, A. Glisenti, T. Montini, L. De Rogatis, and P. Fornasiero. La<sub>0.6</sub>Sr<sub>0.4</sub>Co<sub>1-y</sub>Fe<sub>y</sub>O<sub>3-δ</sub> Perovskites: Influence of the Co/Fe Atomic Ratio on Properties and Catalytic Activity toward Alcohol Steam-Reforming. *Chem. Mater.* **2008**, *20*, 2314-2327.
- (152) S. Tao and J. T. S. Irvine. Catalytic Properties of the Perovskite Oxide La<sub>0.75</sub>Sr<sub>0.25</sub>Cr<sub>0.5</sub>Fe<sub>0.5</sub>O<sub>3-d</sub> in Relation to Its Potential as a Solid Oxide Fuel Cell Anode Material. *Chem. Mater.* **2004**, *16*, 4116-4121.
- (153) L. W. Tai, M. M. Nasrallah, H. U. Anderson, D. M. Sparlin, and S. R. Sehlin. Structure and electrical properties of La<sub>1-x</sub>Sr<sub>x</sub>Co<sub>1-y</sub>Fe<sub>y</sub>O<sub>3</sub>. Part 1. The system La<sub>0.8</sub>Sr<sub>0.2</sub>Co<sub>1-y</sub>Fe<sub>y</sub>O<sub>3</sub>. *Solid State Ionics* **1995**, *76*, 259-271.
- (154) R. D. Shannon. Revised effective ionic radii and systematic studies of Interatomic distances in halides and chalcogenides. *Acta Crystallographica* **1976**, *A32*, 751-767.
- (155) L. Bedel, A.-C. Roger, C. Estournes, and A. Kiennemann. Co<sup>0</sup> from partial reduction of La(Co,Fe)O<sub>3</sub> perovskites for Fischer–Tropsch synthesis. *Catalysis Today* **2003**, *85*, 207-218.
- (156) M. K. Gnanamani, W. D. Shafer, D. E. Sparks, and B. H. Davis. Fischer–Tropsch synthesis: Effect of CO<sub>2</sub> containing syngas over Pt promoted Co/γ-Al<sub>2</sub>O<sub>3</sub> and K-promoted Fe catalysts. *Catal. Comm.* **2011**, *12*, 936-939.
- (157) C. Liu, L. Munjanja, T. R. Cundari, and A. Wilson. Theoretical studies on the catalysis of reverse water-gas shift reaction using first-row transition metal B-diketiminato complexes. *Journal of Physical Chemistry A* **2010**, *21*, 6207-6216.
- (158) L. W. Tai, M. M. Nasrallah, H. U. Anderson, D. M. Sparlin, and S. R. Sehlin. Structure and electrical properties of La<sub>1-x</sub>Sr<sub>x</sub>Co<sub>1-y</sub>Fe<sub>y</sub>O<sub>3</sub>. Part 2. The system La<sub>1-x</sub>Sr<sub>x</sub>Co<sub>0.2</sub>Fe<sub>0.8</sub>O<sub>3</sub>. *Solid State Ionics* **1995**, *76*, 273-283.
- (159) D. Bilanovic; 4. In *Environmental Indicators*. vol., R. H. Armon and O. Hänninen; Springer Netherlands: 2015, pp. 51-66.
- (160) *2014 World Energy Outlook*; International Energy Agency, Paris, France, 2014
- (161) *The global status of CCS: 2014*; Global CCS Institute 2014, Melbourne, Australia, 2014
- (162) K. Lackner. A Guide to CO<sub>2</sub> Sequestration. *Science* **2003**, *300*, 1677-1678.
- (163) P. Riemer. Greenhouse gas mitigation technologies, an overview of the CO<sub>2</sub> capture, storage and future activities of the IEA Greenhouse Gas R&D programme. *Energy Conversion and Management* **1996**, *37*, 665-670.
- (164) S. Holloway, J. M. Pearce, V. L. Hards, T. Ohsumi, and J. Gale. Natural emissions of CO<sub>2</sub> from the geosphere and their bearing on the geological storage of carbon dioxide. *Energy* **2007**, *32*, 1194-1201.
- (165) N. von der Assen, J. Jung, and A. Bardow. Life-cycle assessment of carbon dioxide capture and utilization: avoiding the pitfalls. *Energy & Environmental Science* **2013**, *6*, 2721-2734.
- (166) Y. Zhang, S. Zhang, H. H. Lou, J. L. Gossage, and T. J. Benson. Steam and Dry Reforming Processes Coupled with Partial Oxidation of Methane for CO<sub>2</sub> Emission Reduction. *Chemical Engineering & Technology* **2014**, *37*, 1493-1499.
- (167) N. Lakshminarayanan, H. Choi, J. N. Kuhn, and U. S. Ozkan. Effect of additional B-site transition metal doping on oxygen transport and activation characteristics in La<sub>0.6</sub>Sr<sub>0.4</sub>(Co<sub>0.18</sub>Fe<sub>0.72</sub>X<sub>0.1</sub>)O<sub>3-δ</sub> (where X = Zn, Ni or Cu) perovskite oxides. *Applied Catalysis B: Environmental* **2011**, *103*, 318-325.

- (168) H. Luo, K. Efimov, H. Jiang, A. Feldhoff, H. Wang, and J. Caro. CO<sub>2</sub>-Stable and Cobalt-Free Dual-Phase Membrane for Oxygen Separation. *Angewandte Chemie (International ed. in English)* **2011**, *50*, 759-763.
- (169) H. J. M. Bouwmeester. Dense ceramic membranes for methane conversion. *Catalysis Today* **2003**, *82*, 141-500.
- (170) H. Wang, C. Tablet, A. Feldhoff, and J. Caro. A Cobalt-Free Oxygen-Permeable Membrane Based on the Perovskite-Type Oxide Ba<sub>0.5</sub>Sr<sub>0.5</sub>Zn<sub>0.2</sub>Fe<sub>0.8</sub>O<sub>3-δ</sub>. *Advanced Materials* **2005**, *17*, 1785-1788.
- (171) H. Luo, H. Jiang, T. Klande, Z. Cao, F. Liang, H. Wang, and J. Caro. Novel Cobalt-Free, Nobel Metal-Free Oxygen-Permeable 40Pr<sub>0.6</sub>Sr<sub>0.4</sub>FeO<sub>3-δ</sub>-60Ce<sub>0.9</sub>Pr<sub>0.1</sub>O<sub>2-δ</sub>. *Chemistry of Materials* **2012**, *24*, 2148-2154.
- (172) Q. Zeng, Y.-B. Zuo, C.-G. Fan, and C.-S. Chen. CO<sub>2</sub>-tolerant oxygen separation membrane targeting CO<sub>2</sub> capture application *Journal of Material Science* **2009**, *335*, 140-144.
- (173) S.-G. Wang, X.-Y. Liao, D.-B. Cao, C.-F. Huo, Y.-W. Li, J. Wang, and H. Jiao. Factors Controlling the Interaction of CO<sub>2</sub> with Transition Metal Surfaces. *Journal of Physical Chemistry C* **2007**, *111*, 16934-16940.
- (174) S. A. Gardezi, B. Joseph, F. Prado, and A. Barbosa. Thermochemical biomass to liquid (BTL) process: Bench-scale experimental results and projected process economics of a commercial scale process. *Biomass and Bioenergy* **2013**, *59*, 168-186.
- (175) K. P. Kuhl, E. R. Cave, D. N. Abram, and T. F. Jaramillo. New insights into the electrochemical reduction of carbon dioxide on metallic copper surfaces. *Energy & Environmental Science* **2012**, *5*, 7050-7059.
- (176) S. S. Fu and G. A. Somorjai. Interactions of O<sub>2</sub>, CO, CO<sub>2</sub>, and D<sub>2</sub> with the stepped Cu(311) crystal face: Comparison to Cu(110). *Surface Science* **1992**, *262*, 68-76.
- (177) A. A. Peterson, F. Abild-Pedersen, F. Studt, J. Rossmeisl, and J. K. Nørskov. How copper catalyzes the electroreduction of carbon dioxide into hydrocarbon fuels. *Energy & Environmental Science* **2010**, *3*, 1311-1315.
- (178) G.-C. Wang, L. Jiang, Y. Morikawa, J. Nakamura, Z.-S. Cai, Y.-M. Pan, and X.-Z. Zhao. Cluster and periodic DFT calculations of adsorption and activation of CO<sub>2</sub> on the Cu(hkl) surfaces. *Surface Science* **2004**, *570*, 205-217.
- (179) I. Rodriguez-Ramos, A. Guerrero-Ruiz, M. L. Rojas, and J. L. G. Fierro. Dehydrogenation of methanol to methyl formate over copper-containing perovskite-type oxides. *Applied Catalysis* **1991**, *68*, 217.
- (180) C.-S. Chen, W.-H. Cheng, and S.-S. Lin. Enhanced activity and stability of a Cu/SiO<sub>2</sub> catalyst for the reverse water gas shift reaction by an iron promoter. *Chemical Communications* **2001**, 1770-1771.
- (181) C.-S. Chen, W.-H. Cheng, and S.-S. Lin. Study of reverse water gas shift reaction by TPD, TPR and CO<sub>2</sub> hydrogenation over potassium-promoted Cu/SiO<sub>2</sub> catalyst. *Applied Catalysis A: General* **2003**, *238*, 55-67.
- (182) *Cobalt Facts*, 2010
- (183) *The Long-Term Availability of Copper*; International Copper Association, Ltd., New York, USA, 2013
- (184) A. M. Deml, V. Stevanović, C. L. Muhich, C. B. Musgrave, and R. O'Hayre. Oxide enthalpy of formation and band gap energy as accurate descriptors of oxygen vacancy formation energetics. *Energy & Environmental Science* **2014**, *7*, 1996-2004.

- (185) A. M. Deml, V. Stevanović, A. M. Holder, M. Sanders, R. O'Hayre, and C. B. Musgrave. Tunable Oxygen Vacancy Formation Energetics in the Complex Perovskite Oxide  $\text{Sr}_x\text{La}_{1-x}\text{Mn}_y\text{Al}_{1-y}\text{O}_3$ . *Chemistry of Materials* **2014**, *26*, 6595-6602.
- (186) D. Gryaznov, M. W. Finnis, R. A. Evarestov, and J. Maier. Oxygen vacancy formation energies in Sr-doped complex perovskites: ab initio thermodynamic study. *Solid State Ionics* **2014**, *254*, 11-16.
- (187) L. Er-Rakho, C. Michel, and B. Raveau.  $\text{La}_{8-x}\text{Sr}_x\text{Cu}_8\text{O}_{20}$ : An oxygen-deficient perovskite built of  $\text{CuO}_6$ ,  $\text{CuO}_5$ , and  $\text{CuO}_4$  polyhedra. *Journal of Solid State Chemistry* **1988**, *73*, 514-519.
- (188) T. Sugimoto, A. Yanagawa, and T. Hashimoto. Evaluation of thermodynamic and kinetic stability of P-type transparent conducting oxide,  $\text{SrCu}_2\text{O}_2$  under various oxygen partial pressures. *Thermochimica Acta* **2012**, *532*, 45-48.
- (189) R. Genouel, C. Michel, and B. Raveau. Powder Neutron Diffraction Study of the Ordered Oxygen-Deficient Perovskites  $(\text{La},\text{Sr})_8\text{Cu}_{8-x}\text{Fe}_x\text{O}_{20}$ . *Chemistry of Materials* **1995**, *7*, 2181-2184.
- (190) J. A. Brown Bourzutschkya, N. Homsa, and A. T. Bell. Conversion of synthesis gas over  $\text{LaMn}_{1-x}\text{Cu}_x\text{O}_{3+\lambda}$  perovskites and related copper catalysts. *Journal of Catalysis* **1990**, *124*, 52-72.
- (191) L. Ge, R. Ran, K. Zhang, S. Liu, and Z. Shao. Oxygen selective membranes based on B-site cation-deficient  $(\text{Ba}_{0.5}\text{Sr}_{0.5})(\text{Co}_{0.8}\text{Fe}_{0.2})_y\text{O}_{3-\delta}$  perovskite with improved operational stability. *Journal of Membrane Science* **2008**, *318*, 182-190.
- (192) S. Bernal, F. J. Botana, R. García, and J. M. Rodríguez-Izquierdo. Behaviour of rare earth sesquioxides exposed to atmospheric carbon dioxide and water. *Reactivity of Solids* **1987**, *4*, 23-40.
- (193) M. P. Rosynek and D. T. Magnuson. Infrared study of carbon dioxide adsorption on lanthanum sesquioxide and trihydroxide. *Journal of Catalysis* **1977**, *48*, 417-421.
- (194) C. Liu, T. R. Cundari, and A. K. Wilson.  $\text{CO}_2$  Reduction on Transition Metal (Fe, Co, Ni, and Cu) Surfaces: In Comparison with Homogeneous Catalysis. *The Journal of Physical Chemistry C* **2012**, *116*, 5681-5688.
- (195) J. Nakamura, J. A. Rodriguez, and C. T. Campbell. Does  $\text{CO}_2$  dissociatively adsorb on Cu surfaces? *Journal of Physics: Condensed Matter* **1989**, *1*, SB149-SB160.
- (196) J. A. Rodriguez, J. Evans, L. Feria, A. B. Vidal, P. Liu, K. Nakamura, and F. Illas.  $\text{CO}_2$  hydrogenation on Au/TiC, Cu/TiC, and Ni/TiC catalysts: Production of CO, methanol, and methane. *Journal of Catalysis* **2013**, *307*, 162-169.
- (197) U. S. E.P.A. *State  $\text{CO}_2$  Emissions from Fossil Fuel Combustion 1990-2013*. Available: [https://www3.epa.gov/statelocalclimate/resources/state\\_energyco2inv.html](https://www3.epa.gov/statelocalclimate/resources/state_energyco2inv.html)
- (198) U. S. E.I.A. (2013, March 19<sup>th</sup>). *Rankings: Total Carbon Dioxide Emissions*. Available: <http://www.eia.gov/state/rankings/?sid=FL-series/226>
- (199) F. D. o. E. Protection. (Last updated: September 25, 2015). *Emissions sources: Central Power & Lime Biomass Project*. Available: [http://www.dep.state.fl.us/air/emission/bioenergy/central\\_power.htm](http://www.dep.state.fl.us/air/emission/bioenergy/central_power.htm)
- (200) F. G. Acien Fernández, C. V. González-López, J. M. Fernández Sevilla, and E. Molina Grima. Conversion of  $\text{CO}_2$  into biomass by microalgae: how realistic a contribution may it be to significant  $\text{CO}_2$  removal? *Applied Microbiology and Biotechnology* **2012**, *96*, 577-586.

- (201) L. Gustavsson, P. Börjesson, B. Johansson, and P. Svanberg. Reducing CO<sub>2</sub> emissions by substituting biomass for fossil fuels. *Energy* **1995**, *20*, 1097-1113.
- (202) J. David and H. Herzog, "The cost of carbon capture, in *Fifth international conference on greenhouse gas control technologies*, 2000, pp. 13-16.
- (203) *Renewable Energy Cost Analysis*; International Renewable Energy Agency, United Arab Emirates, 2012
- (204) J. I. Levene, M. K. Mann, R. M. Margolis, and A. Milbrandt. An analysis of hydrogen production from renewable electricity sources. *Solar Energy* **2007**, *81*, 773-780.
- (205) Y. A. Daza, "Experimentally determined density of La<sub>0.75</sub>Sr<sub>0.25</sub>CoO<sub>3</sub>," ed, 2012.
- (206) A. H. Bork, M. Kubicek, M. Struzik, and J. L. M. Rupp. Perovskite La<sub>0.6</sub>Sr<sub>0.4</sub>Cr<sub>1-x</sub>Co<sub>x</sub>O<sub>3-δ</sub> solid solutions for solar-thermochemical fuel production: strategies to lower the operation temperature. *Journal of Materials Chemistry A* **2015**, *3*, 15546-15557.

## APPENDICES

## Appendix A Copyright Permissions

### A.1 Permission for Use of Material in Chapter 3

1/21/2016

Rightslink® by Copyright Clearance Center



RightsLink®

Home

Create Account

Help



ACS Publications  
Most Trusted. Most Cited. Most Read.

**Title:** Carbon Dioxide Conversion by Reverse Water–Gas Shift Chemical Looping on Perovskite-Type Oxides

**Author:** Yolanda A. Daza, Ryan A. Kent, Matthew M. Yung, et al

**Publication:** Industrial & Engineering Chemistry Research

**Publisher:** American Chemical Society

**Date:** Apr 1, 2014

Copyright © 2014, American Chemical Society

LOGIN

If you're a **copyright.com user**, you can login to RightsLink using your copyright.com credentials. Already a **RightsLink user** or want to [learn more?](#)

#### PERMISSION/LICENSE IS GRANTED FOR YOUR ORDER AT NO CHARGE

This type of permission/license, instead of the standard Terms & Conditions, is sent to you because no fee is being charged for your order. Please note the following:

- Permission is granted for your request in both print and electronic formats, and translations.
- If figures and/or tables were requested, they may be adapted or used in part.
- Please print this page for your records and send a copy of it to your publisher/graduate school.
- Appropriate credit for the requested material should be given as follows: "Reprinted (adapted) with permission from (COMPLETE REFERENCE CITATION). Copyright (YEAR) American Chemical Society." Insert appropriate information in place of the capitalized words.
- One-time permission is granted only for the use specified in your request. No additional uses are granted (such as derivative works or other editions). For any other uses, please submit a new request.

BACK

CLOSE WINDOW

Copyright © 2016 [Copyright Clearance Center, Inc.](#) All Rights Reserved. [Privacy statement.](#) [Terms and Conditions.](#) Comments? We would like to hear from you. E-mail us at [customercare@copyright.com](mailto:customercare@copyright.com)



## A.2 Permission for Use of Material in Chapter 4

1/21/2016

Rightslink® by Copyright Clearance Center



RightsLink®

Home

Account Info

Help



**Title:** Isothermal reverse water gas shift chemical looping on La<sub>0.75</sub>Sr<sub>0.25</sub>Co(1-Y)FeYO<sub>3</sub> perovskite-type oxides

**Author:** Yolanda A. Daza,Debtanu Maiti,Ryan A. Kent,Venkat R. Bhethanabotla,John N. Kuhn

**Publication:** Catalysis Today

**Publisher:** Elsevier

**Date:** 1 December 2015

Copyright © 2015 Elsevier B.V. All rights reserved.

Logged in as:  
Yolanda Daza  
Account #:  
3000992586

LOGOUT

### Order Completed

Thank you very much for your order.

This is a License Agreement between Yolanda A Daza ("You") and Elsevier ("Elsevier"). The license consists of your order details, the terms and conditions provided by Elsevier, and the [payment terms and conditions](#).

[Get the printable license.](#)

License Number	3793860034168
License date	Jan 21, 2016
Licensed content publisher	Elsevier
Licensed content publication	Catalysis Today
Licensed content title	Isothermal reverse water gas shift chemical looping on La <sub>0.75</sub> Sr <sub>0.25</sub> Co(1-Y)FeYO <sub>3</sub> perovskite-type oxides
Licensed content author	Yolanda A. Daza,Debtanu Maiti,Ryan A. Kent,Venkat R. Bhethanabotla,John N. Kuhn
Licensed content date	1 December 2015
Licensed content volume number	258
Licensed content issue number	n/a
Number of pages	8
Type of Use	reuse in a thesis/dissertation
Portion	full article
Format	both print and electronic
Are you the author of this Elsevier article?	Yes
Will you be translating?	No
Title of your thesis/dissertation	Renewable concentrated CO <sub>2</sub> conversion to CO for liquid fuels synthesis
Expected completion date	May 2016
Estimated size (number of pages)	150
Elsevier VAT number	GB 494 6272 12
Permissions price	0.00 USD
VAT/Local Sales Tax	0.00 USD / 0.00 GBP
Total	0.00 USD

ORDER MORE...

CLOSE WINDOW

Copyright © 2016 Copyright Clearance Center, Inc. All Rights Reserved. [Privacy statement](#). [Terms and Conditions](#). Comments? We would like to hear from you. E-mail us at [customercare@copyright.com](mailto:customercare@copyright.com)

<https://s100.copyright.com/AppDispatchServlet>

1/2

## A.3 Permission for Use of Material in Chapter 5

1/21/2016

Rightslink® by Copyright Clearance Center

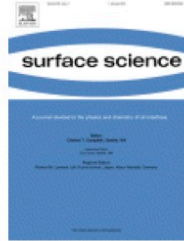


RightsLink®

Home

Account Info

Help



**Title:** More Cu, more problems: Decreased CO<sub>2</sub> conversion ability by Cu-doped La<sub>0.75</sub>Sr<sub>0.25</sub>FeO<sub>3</sub> perovskite oxides

**Author:** Yolanda A. Daza, Debtanu Maiti, Bryan J. Hare, Venkat R. Bhethanabotla, John N. Kuhn

**Publication:** Surface Science

**Publisher:** Elsevier

**Date:** Available online 28 November 2015

Logged in as:  
Yolanda Daza  
Account #:  
3000992586

LOGOUT

Copyright © 2015 Elsevier B.V. All rights reserved.

### Permission Request Submitted

**Your request is now under review.  
You will be notified of the decision via email.  
Please print this request for your records.**

[Get the printable order details.](#)

Order Number	501100782
Order Date	Jan 21, 2016
Licensed content publisher	Elsevier
Licensed content publication	Surface Science
Licensed content title	More Cu, more problems: Decreased CO <sub>2</sub> conversion ability by Cu-doped La <sub>0.75</sub> Sr <sub>0.25</sub> FeO <sub>3</sub> perovskite oxides
Licensed content author	Yolanda A. Daza, Debtanu Maiti, Bryan J. Hare, Venkat R. Bhethanabotla, John N. Kuhn
Licensed content date	Available online 28 November 2015
Licensed content volume number	n/a
Licensed content issue number	n/a
Number of pages	1
Type of Use	reuse in a thesis/dissertation
Portion	full article
Format	both print and electronic
Are you the author of this Elsevier article?	Yes
Will you be translating?	No
Title of your thesis/dissertation	Renewable concentrated CO <sub>2</sub> conversion to CO for liquid fuels synthesis
Expected completion date	May 2016
Elsevier VAT number	GB 494 6272 12
Permissions price	Not Available
VAT/Local Sales Tax	Not Available
Total	Not Available

ORDER MORE...

CLOSE WINDOW

Copyright © 2016 Copyright Clearance Center, Inc. All Rights Reserved. [Privacy statement](#). [Terms and Conditions](#).  
Comments? We would like to hear from you. E-mail us at [customercare@copyright.com](mailto:customercare@copyright.com)

<https://s100.copyright.com/AppDispatchServlet>

1/1

## Appendix B Calculations

### B.1 X-Ray Diffraction Qualitative Analysis for Different Geometries

Table B-1. Summary of equations. Modified from [103]

System	Axial lengths and angles	Plane spacing equations
Cubic	$a = b = c, \alpha = \beta = \gamma = 90^\circ$	$\frac{1}{d^2} = \frac{h^2 + k^2 + l^2}{a^2}$
Tetragonal	$a = b \neq c, \alpha = \beta = \gamma = 90^\circ$	$\frac{1}{d^2} = \frac{h^2 + k^2}{a^2} + \frac{l^2}{c^2}$
Hexagonal	$a = b \neq c, \alpha = \beta = 90^\circ, \gamma = 120^\circ$	$\frac{1}{d^2} = \frac{4}{3} \left( \frac{h^2 + hk + k^2}{a^2} \right) + \frac{l^2}{c^2}$
Orthorhombic	$a \neq b \neq c, \alpha = \beta = \gamma = 90^\circ$	$\frac{1}{d^2} = \frac{h^2}{a^2} + \frac{k^2}{b^2} + \frac{l^2}{c^2}$
Monoclinic	$a \neq b \neq c, \alpha = \gamma = 90^\circ \neq \beta$	$\frac{1}{d^2} = \frac{1}{\sin^2 \beta} \left( \frac{h^2}{a^2} + \frac{k^2 \sin^2 \beta}{b^2} + \frac{l^2}{c^2} - \frac{2hl \cos \alpha}{ac} \right)$
Rhombohedral (trigonal)	$a = b = c, \alpha = \beta = \gamma \neq 90^\circ$	$\frac{1}{d^2} = \frac{(h^2 + k^2 + l^2) \sin^2 \alpha + 2(hk + kl + hl)(\cos^2 \alpha - \cos \alpha)}{a^2(1 - 3 \cos^2 \alpha + 2 \cos^3 \alpha)}$
Triclinic	$a \neq b \neq c, \alpha \neq \beta \neq \gamma \neq 90^\circ$	$\frac{1}{d^2} = \frac{1}{V^2} (S_{11} h^2 + S_{22} k^2 + S_{33} l^2 + 2 S_{12} h k + 2 S_{23} k l + 2 S_{13} h l)$ $S_{11} = b^2 c^2 \sin^2 \alpha$ $S_{22} = a^2 c^2 \sin^2 \beta$ $S_{33} = a^2 b^2 \sin^2 \gamma$ $S_{12} = abc^2 (\cos \alpha \cos \beta - \cos \gamma)$ $S_{23} = a^2 bc (\cos \beta \cos \gamma - \cos \alpha)$ $S_{13} = ab^2 c (\cos \gamma \cos \alpha - \cos \beta)$

## B.2 Sample Ionization Factor Calculations

To calculate the ionization factor of a gas on the MS with a certain carrier gas, the desired gas should be flowed at different flow rates with respect to the carrier until the signal is stable at each step. Only the desired gas and the carrier should be flowed. In this example, the desired gas will be CO and the carrier He.

Ideally, the following statement is true (for each combination of flow rates):

$$F_{CO\_set} = F_{tot} * \frac{S_{r\_CO}}{S_{r\_CO} + S_{r\_He}}$$

where  $S_{r\_CO}$  is the raw signal of  $m/z=28$  (representative of CO),  $F_{tot}$  is the total volumetric flow rate (scm) set on the Alicat mass flow controllers (sum of He and CO flow rates in scm), and  $F_{CO\_set}$  is the flow rate (in scm) set for CO on the Alicat mass flow controllers.

But, because of differences in ionization of difference gases in the MS, Ionization Factors (IF) should be introduced into the equation to normalize the data and allow for quantitative analysis:

$$F_{CO\_set} = F_{tot} * \frac{\frac{S_{r\_CO}}{IF_{CO}}}{\frac{S_{r\_CO}}{IF_{CO}} + S_{r\_He}}$$

rearranging the equation, we get:

$$\frac{F_{tot}}{F_{CO\_set}} = \frac{S_{r\_He}}{S_{r\_CO}} * IF_{CO} + 1$$

which is of the form:  $y = b + m * x$ . After plotting  $\frac{F_{tot}}{F_{CO\_set}}$  (in the vertical axis) vs.  $\frac{S_{r\_He}}{S_{r\_CO}}$  (in the horizontal axis), and setting the intercept to 1, the pendent is the IF. It is important to note that at least 3 points (not counting 0 scm for the desired gas) should be taken, and the total flow rate should remain constant.

When using a water bubbler, the Antoine equation is used:

$$\text{Log}_{10}(P) = A - \frac{B}{(T + C)}$$

using the A, B and C values corresponding to the temperature of the bubbler, we rearrange the equation to calculate P. Next, the partial pressure of water is calculated by dividing P by 760 mm Hg as follows:

$$P_{H_2O} = \frac{P \text{ (from Antoine eq)}}{760 \text{ mmHg}}$$

Then, the partial pressure of water is multiplied by the He flow (in sccm) that was passed through the bubbler, resulting on the equivalent to the Flow set of water vapor, as following:

$$F_{set_{H_2O}} = P_{H_2O} * F_{set_{He\_to\_bubbler}}$$

Next, the calculations described on the previous section can be performed by substituting  $F_{set_{CO}}$  by  $F_{set_{H_2O}}$ .

### B.3 Procedure for Mass Spectrometry Qualitative Analysis

1) Determine the offset of desired masses. During the period of the experiment where only He is flowing, an average value of mass 28 (and other masses of interest) can be quantified and subtracted from all the values of mass 28, that way, we are minimizing the contribution of N<sub>2</sub> (from air) to mass 28.

2) Determine contribution of certain gases to other masses of interest. For example, determine CO<sub>2</sub> contribution to mass 28. After the experiment is over, but before turning off the filaments in the MS, CO<sub>2</sub> and He were flowed, and the data obtained from this period was used to quantify the contribution of CO<sub>2</sub> to mass 28 (mass 28 is the m/z used for CO calculations).

3) Divide by IF: Divide the signals of the masses of interest (in the case of this dissertation: CO<sub>2</sub> (m/z=44), CO (m/z=28), H<sub>2</sub>O (m/z=18) and H<sub>2</sub> (m/z=2) by their respective ionization factors).

4) Divide by sum of all masses: Add all the signals (divided by IFs), including He, and divide each mass of interest by the sum of all the signals.

5) Calculate trapezoidal area: Use a numerical integration method to integrate the area under the curve of the masses of interest.

6) Use ideal gas equation of state to calculate moles of products and reactants: Multiply the area obtained by the total volumetric flow rate (usually 50 sccm) and use the ideal gas equation to calculate the moles/min out of the reactor for each gas. When this value is multiplied by the amount of time in which the reaction took place, the total moles produced (or moles out) of each gas are obtained.

## B.4 Data Used in Calculations on Chapter 6

Table B-4 Constants used in the calculations. Properties of the materials, conversion factors and energy specificities.

Densities and molar masses		
CO <sub>2</sub>	44.01	g/mol
CO <sub>2</sub>	1.98	kg/m <sup>3</sup>
La <sub>0.75</sub> S <sub>0.25</sub> FeO <sub>3</sub>	229.93	g/mol
La <sub>0.75</sub> S <sub>0.25</sub> CoO <sub>3</sub>	660.00	kg/m <sup>3</sup>
H <sub>2</sub>	2.00	g/mol
CO	28.00	g/mol
H <sub>2</sub> O	18.00	g/mol
C <sub>8</sub> H <sub>18</sub>	114.22	g/mol
C <sub>8</sub> H <sub>18</sub>	703.00	kg/m <sup>3</sup>
CH <sub>3</sub> OH	32.04	g/mol
CH <sub>3</sub> OH	791.80	kg/m <sup>3</sup>
Conversion factors		
1 car	7.00	m <sup>3</sup>
football field	5363.60	m <sup>2</sup>
1 ton	0.91	tonne
H <sub>2</sub> cost (solar)	11.00	\$/kg
1 Mega tonne	1,000,000	tonne
1 Giga tonne	1,000	Mega tonne
1 m <sup>3</sup>	264.17	gal
C <sub>8</sub> H <sub>18</sub>	1 gal is 0.88 GGE (gallon gas equivalent)	
CH <sub>3</sub> OH	1 gal is 2 GGE (gallon gas equivalent)	
Energy specificity (energy density per mass)		
H <sub>2</sub>	142	MJ/kg
C <sub>8</sub> H <sub>18</sub>	48	MJ/kg
CH <sub>3</sub> OH	19.7	MJ/kg